University of California
Santa Barbara

# Vibrational Spectroscopy of Single Polyatomic Molecular Ions

A dissertation submitted in partial satisfaction
of the requirements for the degree

Doctor of Philosophy
in
Physics

by

Scott Eierman

Committee in charge:

Professor David Patterson, Chair
Professor Andrew Jayich
Professor Mark Bowick

June 2023

The Dissertation of Scott Eierman is approved.

---

Professor Andrew Jayich

---

Professor Mark Bowick

---

Professor David Patterson, Committee Chair

April 2023

Vibrational Spectroscopy of Single Polyatomic Molecular Ions



by

Scott Eierman

To my parents, my family, and everyone who has made this long journey possible.

# Acknowledgements

Everyone acknowledged here knows that their contributions are much more expansive than is written out.

This experiment never would have left the ground without Aaron Calvin's ion trapping knowledge and intuition (and his magic "ion eyes"), in addition to the many other invaluable experimental skills he shared with myself and everyone else. Beyond his laboratory skills, most of my garden would be dead by now if it wasn't for him.

Zeyun Peng's natural aptitude and intuition for the fundamental physics behind everything we did always far surpassed my own and always motivated me to try to learn more. He devised some of the most useful and important aspects of this experiment, in spite of the fact that I argued against many of them. Thankfully for all of us I lost those arguments.

Merrell Brzeczek made some of the hardware central to this experiment, and gave us all a reason to move forward with this work knowing that it would one day pass into the hands of a capable new generation of grad students in our lab.

While it's not entirely his fault, Lincoln Satterthwaite shoulders a lot of the blame for why I fell so deep down the machining rabbit hole. Of course once I was down there I needed someone equally as obsessed to talk shop and compare parts with, and he played that role like a natural.

Through humor, levity, espresso, and cookies, Greta Koumarianou kept our lab sane throughout our grad school experience, and we (mostly) kept each other sane throughout our job search experiences too. All of it would have been much lonelier and more stressful without her around.

Dave Patterson invited me into a young and growing lab, fueled by clever ideas and some of the most unconventional thinking (in the best possible sense) that I've yet been

party to. With Lincoln he bears the rest of the responsibility for my unhealthy machining habits. He also helped me to learn more valuable lessons than I could have anticipated and made ours the best lab I could have hoped to be a part of throughout this experience.

Thanks to everyone for the past five years.

# Curriculum Vitæ

Scott Eierman

## Education

| | |
|---|---|
| 2023 | Ph.D. in Physics, University of California, Santa Barbara. |
| 2021 | M.A. in Physics, University of California, Santa Barbara. |
| 2018 | B.S. in Physics, University of Nevada, Las Vegas. |

## Publications

A. Calvin*, **S. Eierman***, Z. Peng*, M. Brzeczek, L. Satterthwaite, D. Patterson. *Single Molecule Infrared Spectroscopy in the Gas Phase.* Nature (*Accepted, preprint*, 2023)

**S. Eierman**, Z. Peng, A. Calvin, M. Brzeczek, D. Patterson. *A Cryogenic Ion Trap for Single Molecule Vibrational Spectroscopy.* (*Accepted, preprint*, 2023)

Z. Peng, A. Calvin, **S. Eierman**, S. Kresch, D. Patterson. *Vibrational Spectroscopy of a Single Tropylium Molecule with Partial Rotational Resolution.* (*In preparation*, 2023)

A. Calvin, **S. Eierman**, Z. Peng, L. Satterthwaite, S. Kresch, D. Patterson. *Characterizing the Photofragmentation of a Single Indole Radical Cation in the Gas Phase.* (*In preparation*, 2023)

* Joint first author

## Abstract

Vibrational Spectroscopy of Single Polyatomic Molecular Ions

by

Scott Eierman

Vibrational spectroscopy in the gas phase is a powerful analytical tool for probing the structure of polyatomic molecules in an isolated, non-perturbative environment. This dissertation describes the development of a novel experimental technique for non-destructively measuring the vibrational spectrum of single gas phase polyatomic molecules. This is believed to be the first report of such a result. The underlying theory relevant to this method, as well as the experimental infrastructure which was constructed to facilitate it, is discussed in detail. Spectra of single molecular ions of multiple species are presented and analyzed, illustrating the general capabilities of this technique. This powerful new analytical tool has important implications for chemical analysis and fundamental physical chemistry experiments, along with other applications which are highlighted.

# Contents

# Chapter 1

# Introduction

Since its inception at the onset of the quantum revolution over a century ago, the field of atomic, molecular, and optical physics (AMO) has undergone a dramatic transformation in both its scope and capabilities. The advent of laser cooling four decades ago began this journey from the largely passive interrogation of atoms to precise quantum control of these systems, providing decades-worth of invaluable scientific results along the way. The "M" in AMO has been almost entirely absent from this evolution, however. The additional vibrational and rotational degrees of freedom in molecular systems make even the simplest molecules dramatically more challenging to tame than their atomic counterparts. Nevertheless, this added complexity raises tantalizing prospects for powerful experimental applications of cold, controlled molecules. Significant effort has therefore been devoted in recent decades to adapting and applying powerful atomic physics tools, such as laser cooling and ion trapping, to molecular systems.

The current cutting edge of experimental AMO physics largely focuses on the direct laser cooling and quantum state manipulation of small molecules. These efforts have led to a significant expansion of the list of molecules which can be directly laser cooled, with well over a dozen to date and many more candidates on the horizon. Many fundamen-

tal molecular processes can be studied through these highly controlled model systems, providing valuable insight into basic molecular physics. Ultracold small molecules are promising for a number of intriguing applications ranging from tests of fundamental physics through precision measurement, to the study of untracold many-body interactions, to the development of molecular quantum bits. The precision required by these more traditional physics applications demands a molecular temperature ($\mu$K-scale) which can only be accessed through direct laser cooling, thus motivating these efforts.

A host of important scientific questions can be interrogated at somewhat higher energy scales, however. Cryogenic buffer gas cooling was largely developed to assist in the laser cooling and trapping process, since it is generalizable to a much broader range of atomic and molecular systems than any laser cooling scheme. While it is limited in its ultimate achievable temperature, the temperature scale relevant to cold chemistry (1-10 K) is readily accessible through this method of cooling. The translational temperature of buffer gas cooled molecules may be reduced even further through the sympathetic laser cooling process, in which a laser cooled atomic ion indirectly reduces the temperature of a molecular ion when confined together in an ion trap. This cooling method relies on straightforward atomic laser cooling, and is therefore significantly simpler to implement than direct laser cooling of molecules. The realization of quantum state-level control of ultracold molecules remains an active, valuable, and formidable research task. The work horse tools which have long been used in this effort, however, are already capable of producing cold, localized molecules which are primed for cold chemistry experiments, all with little adaptation required. The rich structural information provided by spectroscopy then offers an ideal tool for probing the characteristics of these simply produced cold molecules.

Such capabilities raise a truly tantalizing prospect: cold chemistry at the single molecule level. Physical chemists have utilized techniques such as buffer gas cooling

in ion traps to study the spectra and dynamics of cold molecular ensembles for many years. By their very nature, however, such ensembles are messy environments in which many different molecular structures are often present, thus complicating the information which can be extracted from these measurements. The trapping, observation, and manipulation of individual atoms and molecules is all but routine in traditional ion trapping experiments which employ atomic laser cooling, however. Compared to an ensemble measurement, such a system containing an individual molecule is necessarily "pure," as only one molecular structure can be interrogated. Furthermore, as mentioned above, ion traps are the requisite platform for the sympathetic laser cooling process which can produce translationally cold molecules. By integrating all of these tools together, one could therefore produce and spectroscopically probe a single cold molecule. Such capabilities would enable fundamental chemical processes to be studied in a simple and highly controlled environment, free of the congestion and complications intrinsic to conventional ensemble measurements, all with the aid of tried and true experimental methods. What's more, these methods could be readily generalized to a wide range of interesting molecular systems. Thus, in addition the precise study of small molecules for fundamental and applied physics, modern AMO physics is well poised to study a broad suite of molecules and processes important to numerous facets of physical chemistry.

The application of well established tools of cold atom physics to open questions in chemistry, and doing so in the simplest possible fashion, served as the catalyzing idea for the work detailed here. This dissertation presents a novel form of infrared spectroscopy capable of recording vibrational spectra of individual polyatomic molecular ions. The technique combines the standard AMO physics tools of laser cooling and ion trapping, discussed in chapter 2, with established action spectroscopy methods commonly utilized in experimental physical chemistry, discussed in chapter 3. The outcome of this marriage is a novel spectrometer, described in detail in chapter 4, which can identify the chemical

species and isomeric structure of a single polyatomic molecular ion. This apparatus has been used to study three different molecular species: the tropylium cation ($C_7H_7^+$), the dehydrogenated 1,3-benzodioxole cation ($C_6H_4O_2CH^+$), and the yet unidentified photofragments of the indole cation ($C_8H_7N^+$). The results of these experiments are detailed in chapter 5, highlighting the valuable new structural information which this novel single molecule technique has provided. A brief discussion of promising potential applications of this method follows in chapter 6. Finally, appendices A and B provide technical details of the data analysis methods employed in chapter 5.

## 1.1 Permissions and Attributions

1. Much of the theoretical treatment of quadrupole ion traps in ch. 2 is derived from the comprehensive text by March and Todd [1], as well as the excellent dissertations of B. King [2] and P. Richerme [3]. These resources, and references therein, provide a much more detailed theoretical treatment than is presented here.

2. Much of the theoretical treatment of molecular vibrations in ch. 3 is derived from the texts of Woodward [4] and Wilson, Decius, and Cross [5]. A much more comprehensive view of molecular vibrations is provided in both resources.

3. Fig. 3.3.1 is reproduced from J. Chem. Phys. **140**, 221101 (2014) with the permission of AIP Publishing: `http://https://publishing.aip.org/`

4. The spectroscopic data in sec. 5.1 is the result of a collaboration with A. Calvin, Z. Peng, M. Brzeczek, L. Satterthwaite, and D. Patterson, and has been accepted for publication by the journal Nature. It is reproduced here with the permission of Springer Nature: `http://springernature.com`.

5. The reference data in fig. 5.2 has been published in ref. [6]. This data was provided by corresponding author Michael Duncan, and is reproduced here with his permission.

6. The spectroscopic data in sec. 5.2 and sec. 5.3 is the result of a collaboration with A. Calvin, Z. Peng, M. Brzeczek, L. Satterthwaite, and D. Patterson, and has been accepted for publication by the journal Review of Scientific Instruments. It is reproduced here with the permission of AIP Publishing: `http://publishing.aip.org`.

# Chapter 2

# Trapping and Cooling Ions

Ion traps have proven to be invaluable experimental tools in the modern study of AMO physics and physical chemistry. Their inherently long trapping times make them natural platforms for more traditional physics experiments such as precision measurement [7] and action spectroscopy [8, 9, 10]. This long storage time coupled with intrinsic mass sensitivity has also made ion traps a standard tool of mass spectrometry [11, 12], thus significantly advancing research in physical and analytical chemistry as well. This chapter highlights the geometry and trapping characteristics of the linear Paul trap, which is used in the experimental work described in later chapters. This is followed by a discussion of experimental techniques for trapping and cooling atomic and molecular ions, principally through laser cooling and buffer gas cooling.

## 2.1 The Linear Quadrupole Trap

As was first demonstrated by Earnshaw [13], charged particles cannot be confined in space solely by static electric *or* magnetic fields alone.[1] To circumvent Earnshaw's theorem, the Paul trap [14] employs both radio frequency (RF) and DC electric fields: the RF field produces a time varying quadrupole field which confines ions radially, and DC fields applied to the ends of the trap confine ions axially. The geometry and electrical configuration of the linear quadrupole trap (a variant of the Paul trap) are shown in fig. 2.1.

The equipotential lines of a purely quadrupolar field are hyperbolic in shape. In principle, then, the quadrupole electrodes (four long electrodes in fig. 2.1) must also be hyperbolic in order to satisfy the quadrupole boundary conditions. Electrodynamic simulations have shown, however, that the fields produced by cylindrical electrodes[2] deviate from the quadrupolar ideal on the few percent level near the trap center [1], making cylindrical electrode geometries sufficient for most applications. Cylindrical electrodes are much easier to produce than hyperbolic ones, thus simplifying the trap fabrication process while minimally impacting trap performance.

The static quadrupole potential can be written in the most general form

$$\Phi(x, y) = A_0 + A_1\big(B_x x^2 + B_y y^2\big) \tag{2.1}$$

Substitution of this potential into Laplace's equation yields

$$\nabla^2\big\{A_0 + A_1\big(B_x x^2 + B_y y^2\big)\big\} = 0 \tag{2.2}$$

[1] A combination of static electric *and* magnetic fields can provide confinement, and is the basis of the Penning trap.

[2] As well as blade electrodes and a host of other electrode geometries that are widely used

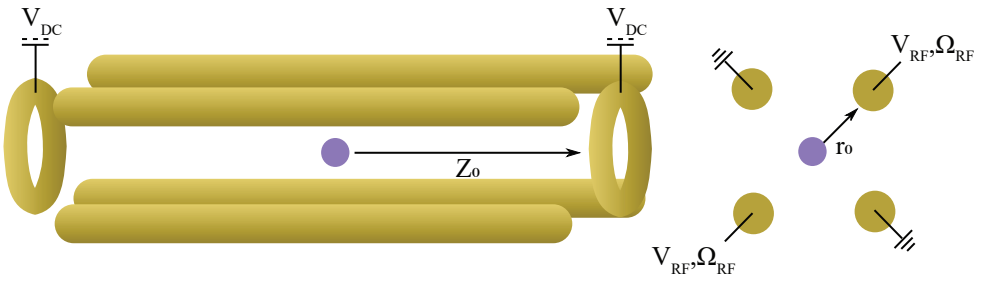


Figure 2.1: The linear quadrupole trap. *Left*: 3D view of the trap electrodes. The ring electrodes on either end of the trap (termed "endcaps") are held at a positive DC voltage, $V_{DC}$, to confine the ions along the trap axis, $Z_0$. *Right*: Perpendicular view of the trap electrodes. Two opposing electrodes are held at ground, while a RF voltage is applied to the other pair, with peak amplitude $V_{RF}$ and frequency $\Omega_{RF}/2\pi$.

$$B_x + B_y = 0 \tag{2.3}$$

As eq. 2.3 shows, the $x$ and $y$ terms of the static quadrupole potential are of opposite sign, forming a classic saddle potential containing only one unstable equilibrium point. This instability is ultimately circumvented in the Paul geometry by effectively rotating this saddle in time at frequency $\Omega_{RF}$, such that the ions are held in a region about the local minimum of the saddle. This corresponds to a time varying voltage applied to the electrodes of

$$\phi(t) = V_0 \cos(\Omega_{RF} t) + U_0 \tag{2.4}$$

where $V_0$ is the peak amplitude of the drive voltage and $U_0$ is a DC offset. A suitable potential which satisfies the quadrupole solution in eq. 2.3, as well as the boundary conditions posed by eq. 2.4, can be written as

$$\phi(x, y, t) = (V_0 \cos(\Omega_{RF} t) + U_0)\left(\frac{x^2 - y^2}{2r_0^2}\right) \tag{2.5}$$

where $r_0$ is the distance between the central axis of the trap and the surface of a quadrupole electrode, also referred to as the inscribed radius of the trap. From this

potential one can then determine the equation of motion of trapped ions in the $x-y$ plane.

### 2.1.1 Equation of Motion

As a result of the symmetry of eq. 2.5, the ion's motion can be solved independently in $x$ and $y$, yielding two solutions of the same form and opposite sign. Inserting eq. 2.5 into the equation for the force in the $x-$direction, $m\ddot{x} = -q\partial_x\phi(x,y,t)$, leads to the differential equation

$$\ddot{x} + \left(\frac{qV_0}{mr_0^2}\cos(\Omega_{RF}t) + \frac{qU_0}{mr_0^2}\right)x = 0 \tag{2.6}$$

for an ion of mass $m$ and charge $q$. Differential equations of this form have been well studied, and one may take advantage of this prior knowledge to apply the following suitable change of variables

$$\zeta = \frac{1}{2}\Omega_{RF}t \qquad q_x = -\frac{2qV_0}{\Omega_{RF}^2 mr_0^2} \qquad a_x = \frac{4qU_0}{\Omega_{RF}^2 mr_0^2} \tag{2.7}$$

With these substitutions, eq. 2.6 can be recast as

$$\frac{\mathrm{d}^2x}{\mathrm{d}\zeta^2} + (a_x - 2q_x\cos(2\zeta))x = 0 \tag{2.8}$$

This is precisely the Mathieu equation, which is known to have general solutions of the form (see ref. [15] for a detailed derivation)

$$x(\zeta) = A\sum_{n=-\infty}^{+\infty} C_{2n}\cos[\zeta(2n+\beta)] + B\sum_{n=-\infty}^{+\infty} C_{2n}\sin[\zeta(2n+\beta)] \tag{2.9}$$

The parameter $\beta$, which itself is a function of the Mathieu parameters $q_x$ and $a_x$, determines the stability of the solution: $x(\zeta)$ is stable (does not diverge as $\zeta \to \infty$) only

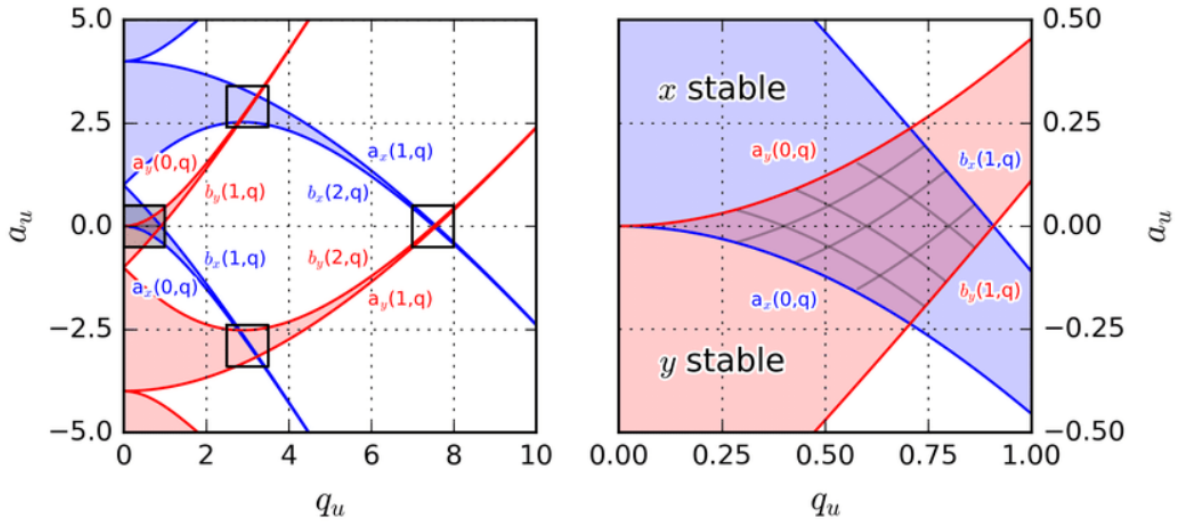


Figure 2.2: The $a$-$q$ stability diagram, reproduced from ref. [16]. Regions shaded blue represent combinations of $a$ and $q$ for which trajectories in the $x$-direction are stable, and regions shaded red represent stable $y$ trajectories. The regions of overlap represent those $a$-$q$ values for which the trap is stable in both directions, and the unshaded regions are unstable trajectories.

for non-integer values of $\beta$. One can then substitute eq. 2.9 into the Mathieu equation and determine the range of values of $q_x$ and $a_x$ which produce stable ion trajectories in the $x-$direction. The process is the same for determining stable trajectories in the $y-$direction, simply with a change of sign between $x$ and $y$. Since $q$ and $a$ are themselves functions of the drive voltage and geometry of the trap, this process equivalently determines the range of experimental parameters for which trapping will occur. A diagram depicting those combinations of $a$ and $q$ for which stable trajectories occur is shown in fig. 2.2. From this calculation it can be seen that the maximum stable $q_u$ in the first region of overlap, where $U_0 = 0$, is $q_u = 0.908$.

### 2.1.2 The Pseudopotential Approximation

The $x-z$ and $y-z$ cross sections of the saddle potential produced by the Paul trap's quadrupole field are themselves quadratic. The effect of rotating this saddle is therefore

to produce an approximately harmonic potential (imagine viewing a rotating saddle from the side; averaged over time, the saddle effectively "looks" like a harmonic potential). As a result, the ions confined within the quadrupole trap will oscillate approximately as simple harmonic oscillators, with some characteristic secular frequency $\omega_{sec}$. However, since the ions are confined within a potential driven at a frequency $\Omega_{RF}$, rather than a truly harmonic static potential, they will also experience motion at the drive frequency $\Omega_{RF}$ (referred to as "micromotion"), where typically $\Omega_{RF} \gg \omega_{sec}$. The full trajectory of the trapped ions is therefore a convolution of these two oscillations.

In all of the experiments reported here, the quadrupole trap was operated with zero DC bias on the RF electrodes, that is, $U_0 = 0$. Additionally, since the motion of the trapped ions is a mixture of secular and micromotion, the coordinates $x$ and $y$ can be decomposed into $x = x_s + x_\mu$ and $y = y_s + y_\mu$. Applying this to eq. 2.6 in the $U_0 = 0$ case yields

$$(\ddot{\alpha}_s + \ddot{\alpha}_\mu) \pm \frac{qV_0}{mr_0^2} \cos(\Omega_{RF} t) (\alpha_s + \alpha_\mu) = 0 \tag{2.10}$$

where $\alpha = x, y$. From here on, in expressions involving $\pm$ or $\mp$, the upper term applies to the $x-$component, while the lower term applies to the $y-$component. It is at this point that the so-called pseudopotential approximation can be made.[3] It will be assumed that the amplitude of the micromotion is much smaller than that of the secular motion, that is, $\alpha_\mu \ll \alpha_s$. Additionally, since it is assumed that $\Omega_{RF} \gg \omega_{sec}$, this also implies that $\ddot{\alpha}_\mu \gg \ddot{\alpha}_s$. These two assumptions together are the basis of the pseudopotential approximation, and applying them to eq. 2.10 yields

[3]Kapitza introduced the approximation to address the case of an inverted pendulum with a vibrating pivot point, a system whose equation of motion is also given by the Mathieu equation [17].

$$\ddot{\alpha}_\mu \pm \frac{qV_0}{mr_0^2}\cos(\Omega_{RF}t)\alpha_s = 0 \tag{2.11}$$

On the assumption that $\alpha_s(t)$ varies much more slowly than $\alpha_\mu(t)$, $\alpha_s$ in eq. 2.11 can be regarded as approximately constant, so that solving for $\alpha_\mu$ leads to

$$\alpha_\mu \pm \frac{qV_0}{mr_0^2\Omega_{RF}^2}\cos(\Omega_{RF}t)\alpha_s = 0 \tag{2.12}$$

Applying the results in eq. 2.11 and eq. 2.12 to the full ($U_0 = 0$) Mathieu equation (eq. 2.10) and solving for $\alpha_s$,

$$\ddot{\alpha}_s + \frac{q^2V_0^2}{m^2r_0^4\Omega_{RF}^2}\cos^2(\Omega_{RF}t)\alpha_s = 0 \tag{2.13}$$

Since $\Omega_{RF} \gg \omega_{sec}$, eq. 2.13 can be averaged over one period of the drive frequency $\Omega_{RF}$, for which $\langle\cos^2(\Omega_{RF}t)\rangle \to \frac{1}{2}$ and the equation of motion for $\alpha_s$ becomes

$$\ddot{\alpha}_s + \frac{q^2V_0^2}{2m^2r_0^4\Omega_{RF}^2}\alpha_s = 0 \tag{2.14}$$

From this, the solution for the secular coordinates as a function of time is given by

$$\alpha_s = C_\alpha\cos(\omega_\alpha t + \phi_\alpha) \tag{2.15}$$

where $C_\alpha$ is an amplitude constant, and the secular frequency $\omega_\alpha$ is identical in both the $x-$ and $y-$directions

$$\omega_\alpha = \frac{qV_0}{\sqrt{2}mr_0^2\Omega_{RF}} \tag{2.16}$$

For the ion trap geometry described in ch. 4, $r_0 = 2.2$ mm, $V_0 \approx 50$ V, and $\Omega_{RF} = 2\pi \times 1.63$ MHz. This leads to typical radial secular frequencies for $^{88}Sr^+$ of $\omega_\alpha \approx 2\pi \times 196$

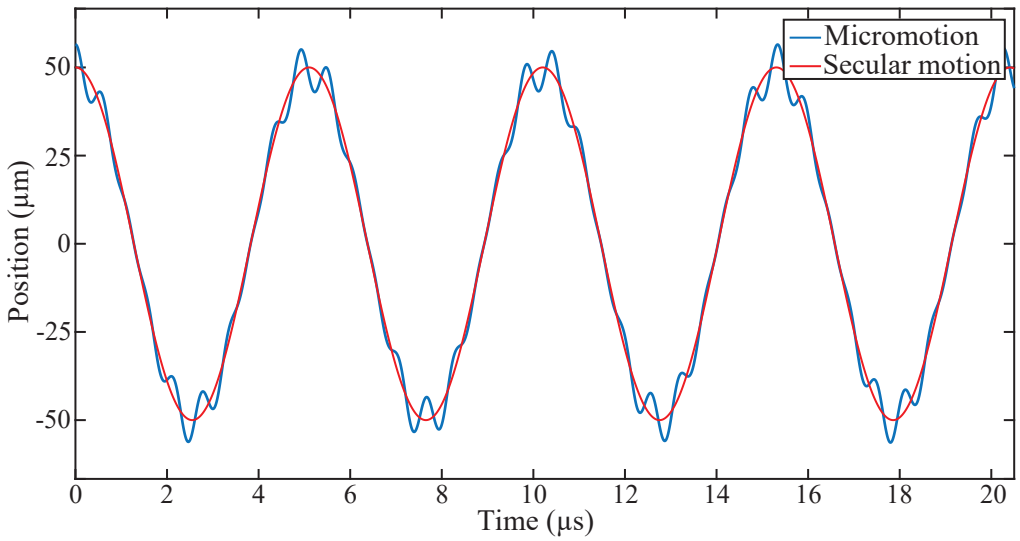


Figure 2.3: Eq. 2.18 for $\alpha = x$ plotted over four secular oscillation periods with the trap parameters and frequencies cited in sec. 4.4. The secular motion for these parameters is plotted against the combined secular and micromotion to illustrate the relationship between the two, especially the displacement-dependence of the micromotion amplitude.

kHz.

With the secular motion coordinate solved for, eq. 2.15 may be inserted back into eq. 2.12 to solve for the micromotion coordinate

$$\alpha_\mu = \mp \frac{qV_0}{mr_0^2\Omega_{RF}^2} \cos(\Omega_{RF}t) C_\alpha \cos(\omega_\alpha t + \phi_\alpha) \tag{2.17}$$

Finally, combining this result with eq. 2.15 yields the full solution for the ion position

$$\alpha = \alpha_s + \alpha_\mu = \left(1 \pm \frac{qV_0}{mr_0^2\Omega_{RF}^2} \cos(\Omega_{RF}t)\right) C_\alpha \cos(\omega_\alpha t + \phi_\alpha) \tag{2.18}$$

The functional form of this equation of motion is that of fast micromotion at frequency $\Omega_{RF}$ overlayed on top of a slower harmonic oscillation at frequency $\omega_\alpha$, an example of which is shown in fig. 2.3. As is clear from eq. 2.12, the amplitude of this micromotion is proportional to the ion displacement from the trap center during slower secular oscillation.

Thus the micromotion amplitude is larger near the turning points of secular motion, and near zero at the trap center. This has important practical ramifications which are discussed in more detail in sec. 4.4.

### 2.1.3 Trap Depth

The development of the pseudopotential model allows for a straightforward approximation of the depth of this confining potential. An ion in a quadrupole trap must not come into contact with any surface in order to remain trapped, otherwise it will be quickly removed from the trap through adsorption at the contact point with that surface. An ion is therefore considered trapped if it has insufficient kinetic energy to reach the nearest surfaces, which are the surfaces of the quadrupole electrodes themselves.

The trap depths along the $x-$ and $y-$axes, $D_x$ and $D_y$, are approximated by equating the conservative restoring force of the pseudopotential which pulls the ion back to the trap center with the 1D simple harmonic oscillator kinetic energy along each of the two axes

$$qD_\alpha = \frac{1}{2}m\omega_\alpha^2 r_0^2 \tag{2.19}$$

where $\alpha = x, y$. As noted in eq. 2.16, $\omega_x$ and $\omega_y$ are degenerate, resulting in a degeneracy of the trap depths along the $x-$ and $y-$ directions, $D_x$ and $D_y$. Inserting eq. 2.16 into eq. 2.19 and solving for $D_\alpha$ yields the approximate trap depth

$$D_\alpha = \frac{qV_0^2}{4mr_0^2\Omega_{RF}^2} \tag{2.20}$$

Again for the trap parameters described in ch. 4 ($r_0 = 2.2$ mm, $V_0 \approx 50$ V, and $\Omega_{RF} = 2\pi \times 1.63$ MHz), eq. 2.20 leads to a trap depth of $\sim$1.4 V. This confining potential depth

far exceeds the average energy of collisions between trapped ions and background gas particles even at room temperature,[4] indicating that ions should remain well trapped even in a warm, collisional environment.

### 2.1.4 Axial Motion

The equations of motion derived to this point assume an infinitely long quadrupole ion trap with no $z-$ component of the electric field. Such a system traps ions in the $x-y$ plane, but provides no confinement along the cylindrical symmetry axis. In practice, a DC potential, $V_{DC}$, is applied to endcap electrodes on the ends of the quadrupole configuration to provide axial confinement (see fig. 2.1). The potential produced near the axis of the quadrupole trap as a result of these DC fields is approximately given by [18]

$$U(x,y,z) \approx \frac{\kappa V_{DC}\left[z^2 - (x^2+y^2)/2\right]}{Z_0^2} \tag{2.21}$$

where $\kappa$ is a geometric constant and $Z_0$ is the distance between the trap center and each endcap electrode. From the perspective of an ion near the axis of a quadrupole trap, the radio frequency fields from the radial confinement electrodes act to partially screen the DC axial potential. This screening effect is encoded in the geometric constant $\kappa$.

The full potential near the trap axis is therefore the sum of eq.s 2.5 and 2.21. The resultant equations of motion for a trapped ion are still separable, however, yielding a Mathieu equation as a function of $z$ with the Mathieu stability parameters

$$a_z = \frac{8\kappa q V_{DC}}{m Z_0^2 \Omega_{RF}^2} \qquad q_z = 0 \tag{2.22}$$

The axial secular frequency $\omega_z$ can be approximated by

[4] 1.4 eV $\approx$ 16,200 K.

$$\omega_z \approx \frac{1}{2}\Omega\sqrt{a_z} = \frac{1}{Z_0}\sqrt{\frac{2\kappa q V_{DC}}{m}} \tag{2.23}$$

which is valid in the case that $a_z \ll 1$ [18]. The geometric screening constant, $\kappa$, can readily be estimated through a measurement of the axial secular frequency $\omega_z$. In the experiments described in later chapters, typical observations yield $\omega_z \approx 2\pi \times 28$ kHz for $^{88}Sr^{+}$, which corresponds to $\kappa \approx 0.025$.

A single ion of mass $m_a$ has an axial secular frequency $\omega_{z,a}$ given by eq. 2.23. If a second ion of mass $m_b$ is co-trapped with a single ion $m_a$ then the frequency, $\omega_{z,ab}$, of the center-of-mass motion of this ion pair along the trap axis can be simply expressed by [19, 20]

$$\omega_{z,ab}^2 = \left[1 + \mu - \sqrt{1 - \mu + \mu^2}\right]\omega_{z,a}^2 \tag{2.24}$$

where $\mu$ is the ratio of the masses of the two ions, $\mu = m_a/m_b$. This relation is utilized extensively in the experiments reported in later chapters. Eq. 2.24 implies that a form of mass spectrometry can be performed with only two ions. The axial secular frequency $\omega_{z,a}$ of a single ion of known mass $m_a$ can first be measured. A further measurement of $\omega_{z,ab}$ for this same ion plus a single ion of unknown mass $m_b$ then allows $m_b$ to be directly determined via eq. 2.24. This is the basis for mass measurements described in greater detail in ch. 4.

### Axial Trap Depth

In analogous fashion to the trap depth approximation in 2.1.3, the effective depth of the confining potential seen by one ion along the axis of the trap can be estimated. The distance to the nearest contact point is $Z_0$ in this case, rather than $r_0$, and the criterion for confinement becomes

$$qD_z = \frac{1}{2}m\omega_z^2 Z_0^2 \tag{2.25}$$

Inserting eq. 2.23 into eq. 2.25 yields the simplified axial trap depth expression

$$D_z = \kappa V_{DC} \tag{2.26}$$

Intuitively, the geometric screening parameter, $\kappa$, therefore acts to reduce the static potential $V_{DC}$ experienced by a single ion near the trap center. The experiments reported in this work typically confined ions axially with a potential of $V_{DC} = 40$ V, which, in combination with the previously estimated value of $\kappa$, yields an approximate axial trap depth of $D_z \approx 1$ V. Again, this potential corresponds to a substantial equivalent temperature,[5] indicating that ions should remain well confined in the quadrupole trap even in a warm, collisional environment.

## 2.2 Laser Cooling

The advent of laser cooling nearly fifty years ago [21] transformed the field of experimental AMO physics and continues to unlock new avenues for significant research. At the core of this phenomenon is the simple fact that photons carry momentum along their propagation axis, $\vec{p} = \hbar\vec{k}$, where $|\vec{k}| = \lambda^{-1}$. If $\lambda$ is near-resonant with a transition in a given atomic system, then an atom in the presence of such a light field can absorb these photons. The conservation of momentum then dictates that the momentum of this atom must change; that is, the photon imparts a momentum "kick" of magnitude $\hbar k$. Thus the process of absorbing these photons exerts a force on the atom along the direction of propagation of the photons.

[5] 1 V $\approx$ 11,600 K.

This process alone is insufficient for a qualitative description of laser cooling, as the atom cannot simply absorb a photon but instead scatters this photon. Stated differently, any photon that is absorbed will be spontaneously re-emitted some time later (characterized by the natural lifetime $\tau$ of the excited state involved). In principle, then, the net force on the atom should be zero, as the scattered photon also imparts a momentum kick to the atom. The direction of spontaneously emitted photons, however, is entirely random. Consequently, averaged over many cycles, the net momentum kick imparted on the atom due to this fluorescence process is zero, and there is a net force on the atom in the direction of propagation of the incident photons.

Quantitatively, this force is dependent on the rate at which incoming photons are scattered, $R_s$, which can be expressed for an ideal two-level atom as [22]

$$R_s = \frac{\Gamma}{2} \frac{I/I_{sat}}{1 + I/I_{sat} + 4\Delta^2/\Gamma^2} \tag{2.27}$$

Here $\Gamma$ is the natural linewidth of the transition excited by the photons, where $\Gamma = \tau^{-1}$. $I_{sat} \equiv \pi hc/3\lambda^3\tau$ is the saturation intensity of the transition, and is defined as the intensity needed to maintain half of all atomic absorbers in the excited state. The detuning $\Delta \equiv \omega_L - \omega_0$ is the difference between the incident light frequency $\omega_L$ and the natural transition frequency $\omega_0$ of the atom. The scattering force is then the product of the photon scattering rate and the photon momentum $\hbar k$.

It is important to note, however, that eq. 2.27 assumes that the atom which is scattering photons is at rest. If instead the atom itself is in motion relative to the incident laser beam then a Doppler shift of the laser frequency in the atomic reference frame occurs. Accounting for this shift, the scattering force becomes

$$F_s = \frac{\hbar k \Gamma}{2} \frac{I/I_{sat}}{1 + I/I_{sat} + 4(\Delta - \vec{k} \cdot \vec{v})^2/\Gamma^2} \tag{2.28}$$

It can readily be seen from eq. 2.28 that this force depends on the velocity of the atom relative to the incident laser field. It is largest when $\Delta = \omega_L - \omega_0 = \vec{k} \cdot \vec{v}$, in which case the laser frequency is Doppler shifted on resonance with the atomic transition.

The two non-zero laser detuning regimes $\Delta > 0$ and $\Delta < 0$ are referred to as blue and red detuning, respectively. In the blue detuned case, $F_s$ is smallest if the atom and laser counter-propagate, as $\vec{k} \cdot \vec{v} = kv \cos \pi = -kv$ and consequently $\Delta - \vec{k} \cdot \vec{v} = \Delta + kv$ is large. $F_s$ is therefore largest in the blue detuned case when the atom and laser are co-propagating. This means that a maximal force is applied to the atom when it is moving away from the laser, in effect increasing its velocity relative to the laser and heating the atom. Thus a blue detuned laser, in general, leads to heating rather than cooling of the atom. Conversely, in the red detuned case, $F_s$ is smallest when the atom and laser co-propagate, as $\vec{k} \cdot \vec{v} = kv \cos 0 = kv$, and consequently $|\Delta - \vec{k} \cdot \vec{v} = \Delta - kv|$ is large (since $\Delta < 0$). $F_s$ is therefore largest when the atom and laser counter-propagate. This means that the scattering force is maximized when it opposes the motion of the atom, and therefore acts to reduce the velocity of the atom, effectively cooling it. This cooling mechanism is often termed Doppler cooling.

As mentioned previously, Doppler cooling exploits the fact that the direction of spontaneously emitted photons is random, so that, averaged over many such events, a net scattering force on an atom in a resonant laser field arises. In practice, however, this does not mean that one needs only to scatter many photons off of an atom to reduce its temperature ever further. Instead there is an intrinsic lower limit on the temperature which can be achieved via Doppler cooling, known as the Doppler temperature, $T_D$. This limit arises from the fact that the random spontaneous emission process causes the atom to undergo Brownian-like motion as it recoils after each emission, effectively heating the atom. The Doppler temperature is therefore the effective temperature of the atom when the heating effect of this random walk is equal to the cooling rate of the scattering force,

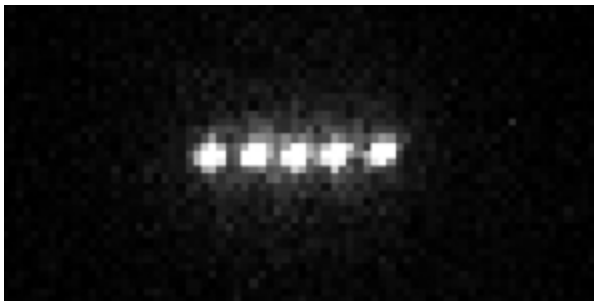

Figure 2.4: An example of a Coulomb Crystal of trapped $^{88}Sr^{+}$ ions. Laser cooling reduces the temperature of these ions below the threshold to form an ordered crystal.

and is found to be [22]

$$T_D = \frac{\hbar\Gamma}{2k_B} \tag{2.29}$$

where $k_B$ is the Boltzmann constant. This is the lowest temperature expected in a Doppler cooled system. In the case of $^{88}Sr^{+}$ ions which are laser cooled in this work, $\Gamma = 2\pi \times 20.05$ MHz (see sec. 2.2.2). Inserting this into eq. 2.29 yields $T_D \approx 0.5$ mK. A host of techniques have been developed since the advent of Doppler cooling which allow temperatures far below the Doppler limit to be achieved. Such techniques are not employed in the experiments described here, however, and so the simple Doppler cooling picture is sufficient to understand this work.

In the case of laser cooled ions in an ion trap, two broad spatial regimes exist. As discussed in sec. 2.1.3, RF ion traps have very deep confining potentials, corresponding to ion temperatures of $\gtrsim 10^4$ K. When trapped ions are at such high temperatures, they remain confined within the trap but will move in large orbits within the trapping region, owing to their large kinetic energy. A group of such warm ions can essentially be viewed as a confined, non-neutral plasma. As the ions are cooled, the amplitude of their orbit continuously decreases. Below a certain temperature, however, these ions will undergo a sort of "phase transition" from a diffuse, disordered plasma, to a spatially periodic

array of ions. This latter phase is referred to as a "Coulomb crystal" [8, 9] (see fig. 2.4). Treating the trapped ions as a simple one component plasma, the critical temperature for this transition can be estimated via the plasma coupling parameter (see ref. [8]). For the inter-ion separation observed here ($\sim$50 $\mu$m, see sec. 2.2.1), this yields and estimated critical temperature of $T_c \simeq 2mK$. This temperature is both within the reach of Doppler cooling and outside the limits of other cooling schemes such as buffer gas cooling, meaning that Coulomb crystals can be readily formed via Doppler cooling. It also serves as an approximate upper bound for the temperature of Coulomb crystallized ions in the system described in ch. 4.

### 2.2.1 Sympathetic Cooling

The Doppler cooling process described in sec. 2.2 allows for atomic ions with closed optical cycles to be cooled to temperatures $\ll$1 K. This closed cycle requirement makes laser cooling experimentally intractable for all but a select few molecules, however, since typical molecular energy manifolds are dramatically more complex than for atoms. Molecular ions can be trapped and cooled to temperatures on the order of 10 K utilizing cryogenic buffer gas, a process which is described in greater detail in sec. 2.3, but additional methods are necessary to cool trapped molecular ions to lower temperatures. This can be achieved through the sympathetic cooling process which, since its first demonstration decades ago [23], has been widely used to cool trapped atomic [24, 25, 26] and molecular [27, 28] ions to translational temperatures $\ll$1 k without directly laser cooling them. This powerful technique has even been used to cool fundamental particles and antiparticles to temperatures of order 1 K [29, 30].

Consider the simple case of two co-trapped ions, only one of which has an appropriate optical cycle for laser cooling. Here the laser cooled species is referred to as the "host",

while the non-laser cooled ion is the "guest."[6] The strong Coulomb interaction between the host and guest leads to a large effective collision cross section, so that kinetic energy is readily exchanged between the two via elastic collisions. Additionally, if laser cooling is applied to the host then its kinetic energy is continuously dissipated. Consequently, the host acts as a heat sink for the guest, as it transfers kinetic energy to its cold partner which is then carried away by fluorescence photons. The net result is that the kinetic energy, and therefore translational temperature, of both ions is reduced, even though only one of the two is directly laser cooled.

While the direct measurement of the temperature of a sympathetically cooled guest ion is often non-trivial to measure, an upper bound on the temperature can be inferred. This is because mixed species Coulomb crystals can readily be created, and are observed routinely in the experiments detailed in later chapters. As discussed in sec. 2.2, the translational temperature threshold for Coulomb crystallization is $\lesssim$2 mK. Both components of a mixed species Coulomb crystal must therefore have translational temperatures on the order of this threshold [28]. An image of a mixed species Coulomb crystal containing a laser cooled $^{88}Sr^{+}$ atomic and a sympathetically cooled $C_7H_7^{+}$ molecular ion is shown in fig. 2.5.

Additionally, the separation between ions in a Coulomb crystal may be estimated straightforwardly. Consider a pair of trapped, laser cooled $^{88}Sr^{+}$ ions. Both ions are attracted to the RF null point at the center of the trap by the harmonic restoring force, $\frac{1}{2}m\omega_z^2 z$. Neither can occupy this point, however, due to their mutual Coulomb repulsion. The equilibrium inter-ion separation therefore arises from the balancing of this mutual repulsion with the harmonic restoring force

[6]The "host" species is always present in the trap during real experiments, since the host is necessary to cool the "guest," hence the terminology: the host is always present in the trap; the guest is not always present, but it is never present alone.

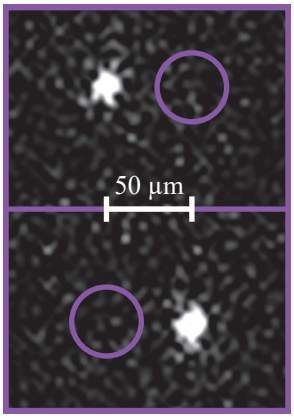


Figure 2.5: A two ion, mixed species Coulomb crystal containing $^{88}Sr^{+}$ and $C_7H_7^{+}$. The ions are separated by approximately 50 $\mu$m at equilibrium. This image was recorded in the experiment described in sec. 5.1.

$$\begin{aligned} \frac{1}{4\pi\epsilon_0}\frac{q^2}{r_s^2} &= \frac{1}{2}m\omega_z^2 r_s \\ r_s &= \left(\frac{q^2}{2\pi\epsilon_0 m\omega_z^2}\right)^{1/3} \end{aligned} \tag{2.30}$$

Applying eq. 2.30 two the case of a two ion Coulomb crystal of $^{88}Sr^{+}$, with an experimentally observed COM axial secular frequency of $\omega_z/2\pi = 28$ kHz, yields an ion separation of $r_s \approx 50$ $\mu$m. Given that the mass of molecular ions investigated here is necessarily similar to that of $^{88}Sr^{+}$, the inter-ion spacing for mixed species Coulomb crystals should be similar to this value.

### Mass Considerations

Among the significant features of the sympathetic cooling scheme is that it is entirely agnostic to the internal structure of the guest ion. Atomic and molecular ions alike can, and have been, efficiently sympathetically cooled via laser cooled host ions. There is, however, a relationship between the choice of the host-guest pair and sympathetic

cooling efficiency. Namely, sympathetic cooling is most efficient when the mass-charge ratio of the host and guest species are as similar as possible [31].

Recalling the discussion in sec. 2.1.2, the pseudopotential seen by an ion in a Paul trap is dependent on the ion's mass-charge ratio, meaning that ions of different species held within the same trap will experience different confining potentials. Equivalently, the Mathieu stability parameters of a trapped ion depend on the mass-charge ratio, and so different species in the same trap have different Mathieu $q$ parameters. At the coarsest level, this means that the ions must have a sufficiently similar mass-charge ratio such that the Mathieu $q$ for all species lies within the stable trapping region. Beyond this, however, the difference in pseudopotential for different species also means that each species will oscillate in the trap with a different secular frequency. The Coulomb interaction between the ions can be viewed simply as a spring coupling the motion of harmonic oscillators. The greatest degree of coupling occurs between two such oscillators when their respective oscillation frequencies are equal, $\omega_1 = \omega_2$, and the coupling becomes weaker as the difference between their frequencies, $\Delta\omega$, increases. Consequently, the coupling between two co-trapped ions will be greatest when they are of equal mass-charge ratio, and will become weaker as their mass-charge ratios become more dissimilar. If the motions of the two ions are largely decoupled, kinetic energy isn't efficiently transferred between the ions, and therefore the sympathetic cooling effect is minimal. When designing such experiments it is therefore prudent to choose ions of similar mass-charge ratio in order to maximize the sympathetic cooling efficiency between them. It should be noted, however, that this efficiency can remain quite high even for species of relatively disparate size; systems with mass-charge ratio disparities of nearly an order of magnitude (laser cooled ions and highly charged proteins) have been successfully sympathetically cooled to translational temperatures $<1$ K [32].

**Sympathetic Cooling of Molecules**

The application of sympathetic cooling most important to the experiments in this dissertation is the ability to produce well localized, translationally cold molecular ions. But while this technique can efficiently cool the motional degrees of freedom of molecular ions, it cannot also efficiently cool the internal degrees of freedom (that is, vibrational and rotational). There is an intrinsically poor coupling between the motion of a trapped molecular ion and its internal vibrational/rotational state, owing to the large disparity in the relevant time scales for these motions (kHz-scale frequencies for translational motion in a typical RF trap, compared to GHz- and THz-scale frequencies for rotations and vibrations, respectively). This has been confirmed experimentally by directly recording the rotational temperature of sympathetically cooled molecular ions in Coulomb crystals [33], where internal temperature remains high in spite of sympathetic translational cooling. Thus while the kinetic energy of molecular ions can be very effectively reduced through sympathetic cooling, additional cooling schemes are needed to cool their internal degrees of freedom. The method used in this work to address this issue is discussed in detail in sec. 2.3.

### 2.2.2 The Strontium Ion

A greatly simplified depiction of the lowest lying energy levels of $^{88}Sr^{+}$ is shown in fig. 2.6. The $Sr^{+}$ ion is iso-electronic to neutral rubidium (Rb), making it a natural species for laser cooling. The transition wavelengths and excited state lifetimes for this ion have been compiled in ref. [34]. Laser cooling is achieved by driving the $5^2S_{1/2} \rightarrow 5^2P_{1/2}$ transition at 421.55 nm, which has a natural linewidth of $\Gamma/2\pi = 20.05$ MHz. It is found in $^{88}Sr^{+}$ that the branching ratio between the $^2P_{1/2}$ and $^2D_{3/2}$ states is 1:13 [35]. This means that $\sim$8% of 422 nm photon scattering events, on average, will result in the ion

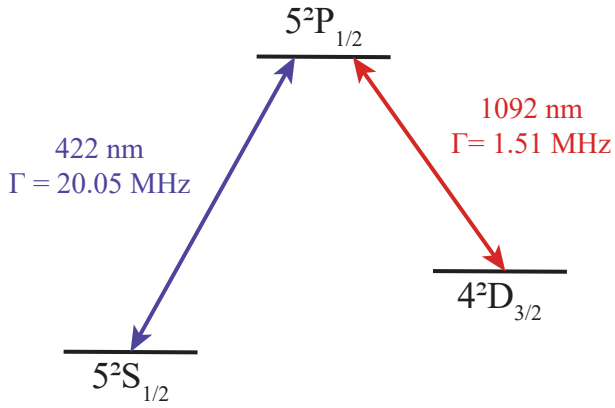


Figure 2.6: The simplified level structure of $^{88}Sr^{+}$, depicting the states and transitions relevant to laser cooling, along with the wavelengths and natural linewidths of these transitions.

decaying to the $^2D_{3/2}$ state. The radiative lifetime for decay from this metastable state back to the $5^2S_{1/2}$ ground state is long (435 ms [36]), so that ions will rapidly accumulate in this state and remain their for a long period of time. Ions in this state are no longer resonant with the 422 nm laser, and therefore will cease to be cooled. To combat this effect, a second "repump" laser drives the $4^2D_{3/2} \rightarrow 5^2P_{1/2}$ transition at 1091.49 nm, which has a natural linewidth of $\Gamma/2\pi = 1.51$ MHz. The effect of this laser is therefore to pump ions out of the dark $4^2D_{3/2}$ state back into the $5^2P_{1/2}$ state, maintaining an effectively closed cycle through which the ion can be efficiently cooled.

$^{88}Sr^{+}$ serves as an ideal choice for the ion trapping experiments reported in later chapters for a number of reasons. As previously discussed in sec. 2.2.1, if a laser cooled atomic ion is to be co-trapped with a molecular ion, the masses of the two must be similar in order to maximize both the stability of the trap and the sympathetic cooling rate of the molecule [31]. The species of the atomic ion used in such an experiment should therefore be chosen to be as close as possible to the masses of molecular ions of interest. The isotope $^{88}Sr$ falls roughly within a range of $\pm 30$ Da of a number of molecules which are interesting for vibrational spectroscopy experiments, making those molecular

species eligible for spectroscopic investigation. In practice, stable Coulomb crystals can be formed with a single laser cooled $^{88}Sr^{+}$ ion and a single molecular ion for molecule masses in the approximate range of 50-150 Da.

## 2.3 Buffer Gas Cooling

Laser cooling allows physicists to routinely achieve phenomenally low temperatures [37]. It is, however, severely restricted in the range of species to which it can be applied. To some extent this is due to experimental restrictions on the frequencies of laser radiation which can be readily generated in the lab (coherent light generation is simplest in the visible to near-infrared). To a much larger extent, however, this is due to the simple level structure necessary for laser cooling. The further a system strays from the ideal two-state model presented in the previous section, the greater the chance for the system to decay to a state that lies outside of the cooling cycle. These conditions together make the vast majority of the periodic table ineligible for laser cooling. They also exclude all but a special few diatomic and triatomic molecules. An alternative cooling scheme is therefore necessary for cold molecule experiments.

Buffer gas cooling has long been used as a partial substitute for laser cooling in both atomic and molecular systems [38, 39, 40]. The technique relies quite simply on elastic collisions between the species of interest and particles of a cryogenically cooled buffer gas. After a sufficient number of such collisions the species of interest thermalizes approximately to the temperature of the buffer gas itself. The ultimate temperature achievable by these means is therefore the ultimate attainable temperature of the buffer gas. While this temperature is quite high compared to what can be achieved via laser cooling, modern closed cycle helium refrigerators can routinely reach liquid helium temperatures at price points comparable to or (often) cheaper than those of laser systems necessary for

laser cooling; such systems are often much simpler to operate and maintain as well.

### 2.3.1 Buffer Gas Species

Several properties affect the experimental choice of a buffer gas species. Chief among these are the reactivity, mass, and vapor pressure of the gas being considered. This first property is straightforward to address: a buffer gas species which tends to react with the analyte species is clearly detrimental, as it effectively depletes the amount of analyte which is present in the experimental region. Inert gases are therefore a natural choice for buffer gas cooling experiments. It is also necessary for the mass of the buffer gas species to be less than that of the analyte, so that it is the buffer gas rather than the analyte which gains momentum and carries it away from the system after a collision. Finally, the vapor pressure curve of a given gas strongly affects its utility for buffer gas cooling applications. The lowest temperature to which an atom or molecule can be effectively cooled is the lowest temperature for which the vapor pressure of the buffer gas is still appreciable.

It is because of these three requirements that helium is perhaps the most common choice of buffer gas: it is an inert noble gas, its mass is low (3-4 Da), it does not freeze at any temperature,[7] and it maintains a high vapor pressure down to $\lesssim$4 K. While $^3$He is particularly advantageous in these respects, as it has a lower mass, lower boiling point, and higher vapor pressure at low temperature than $^4$He, its scarcity compared to $^4$He makes it a much less commonly used species and so only $^4$He is referred to here.

Compared to all other gases, either choice of He isotope represents the lowest possible buffer gas temperature which can be achieved. This makes He the natural choice in experiments for which ultimate temperature is a critical factor, for example in neutral atom/molecule traps which have very low trap depths [38]. This becomes a much less

[7] At atmospheric pressure or below.

significant factor in ion trapping experiments, however, as the depth of an ion trap, as seen in sec. 2.1.2, is on the order of 1 eV, or some 10,000 K. In the particular case of the vibrational spectroscopy experiments detailed in ch. 5, the ability to quickly and efficiently remove buffer gas from the experimental region proves more important than achieving the lowest possible ultimate temperature, the reasons for which will be articulated in more detail in ch. 4. This efficient pumping requirement consequently favors buffer gases which possess higher melting and freezing points than He. This is because such gases will quickly and faithfully freeze to any surface in the experimental region held below the gas's freezing point. For example, a relatively high boiling point gas like $O_2$ injected into a chamber held at 4 K will very quickly freeze to the walls of the chamber,[8] and will maintain an extremely low vapor pressure within that chamber as well. This so-called cryo-pumping or cryo-soprtion process will be discussed in more detail in ch. 4, but the ability that it provides to quickly and efficiently remove gas from an experimental region means that alternative buffer gas species such as Ne and Ar become useful for various applications where high pumping speed is necessary. He and Ne were the primary buffer gas species used in the experiments detailed in later chapters, and so will be given the greatest emphasis in proceeding sections.

### 2.3.2 Collision Cross Section

The conditions necessary for efficient buffer gas cooling (e.g. buffer gas temperature, density, etc.) depend primarily on the collision cross section between the buffer gas species and the species of interest. For neutral-neutral collisions the cross section can be crudely estimated by treating the participating particles as hard spheres of radii equal to their approximate physical size ($\sim$1 Å). In the case of ion-neutral collisions, however, the electric field of the ion tends to partially polarize the neutral collision partner, which

[8] Boiling point $T \simeq 90$ K

then interacts with the ion's field. This polarization interaction tends to dominate the long range ion-neutral interaction potential, which is given by

$$V(r) = -\frac{\alpha q^2}{(4\pi\epsilon_0)^2}\frac{1}{2r^4} \tag{2.31}$$

where $\alpha$ is the polarizability of the neutral collision partner, $q$ is the charge of the ion, $\epsilon_0$ is the permittivity of free space, and $r$ is the internuclear separation.

For a collision between an ion and a neutral particle interacting via such a potential, the impact parameter $b$ has a critical value which can be written as [41]

$$b_c = \left[\frac{2\alpha q^2}{(4\pi\epsilon_0)^2}\frac{1}{E}\right]^{1/4} \tag{2.32}$$

where E is the collision energy in the center-of-mass frame of the particles. In the case of $b > b_c$, if $b$ is sufficiently large, the neutral particle will simply undergo a glancing collision with the ion. For values of $b$ closer to $b_c$, the neutral particle may experience greater deflection or even spiral toward the ion, but will never come closer than $b_c/\sqrt{2}$ [42]. This is due to the so-called centrifugal barrier to the collision, where the fictitious centrifugal force repelling the particles due to their mutual angular momentum exceeds the relative kinetic energy, preventing a head-on collision. In the alternate case, where $b < b_c$, the neutral particle will spiral in toward the center of the ion and undergo a head-on collision. This short-range collision process was first described by Langevin [43], and the so-called Langevin collision cross section can be simply defined in terms of the critical impact parameter as $\sigma_L = \pi b_c^2$ [41, 44], effectively treating the ion as a hard sphere of radius $b_c$. With the center-of-mass frame collision energy $E = \frac{1}{2}\mu v_{rel}^2$, this can be expressed as

$$\sigma_L = \frac{|q|}{2\epsilon_0}\sqrt{\frac{\alpha}{\mu v_{rel}^2}} \tag{2.33}$$

where $v_{rel}$ is the relative velocity between the collision partners. In a thermal ensemble of ions and buffer gas particles, the collision rate coefficient $k$ is given by the average $k = \langle \sigma v \rangle$ [44], yielding

$$k = \frac{|q|}{2\epsilon_0}\sqrt{\frac{\alpha}{\mu}} \tag{2.34}$$

The primary ion of interest in this work is $^{88}Sr^+$, and He is one of the two primary buffer gas species used here. Consider, then, the case of a $^{88}Sr^+$ ion colliding with a He atom. With $\alpha_{He} \simeq 2.30\text{x}10^{-41}$ $C^2s^2/kg$ [45], eq. 2.34 gives $k \simeq 5.44\text{x}10^{-10}$ $cm^3/s$. The relevant buffer gas temperature for the experiments reported in later chapters (see sec. 4.2) is T $\approx$ 13.5 K. For a Boltzmann distribution of He at this temperature, the most probable velocity is ∼237 m/s. Treating the $^{88}Sr^+$ ion as approximately stationary relative to the colliding He atom and using this velocity with eq.s 2.33 and 2.34 yields an approximate collision cross section of $\sigma \simeq 2.29\text{x}10^{-14}$ $cm^2$ for this most probably velocity class. While He is a more common buffer gas species and was used to cool molecules at various stages of this experiment (see sec. 3.3), Ne buffer gas was also employed here, primarily when loading ions into the ion trap.[9] Performing this same exercise with $^{88}Sr^+$ and Ne at T = 13.5 K,[10] with the larger Ne polarizability of $\alpha \simeq 3.91\text{x}10^{-41}$ [46], yields $\sigma \simeq 3.24 \times 10^{-14}$ $cm^2$.

While these exact values are only approximate and are computed only for the most probable velocity class of each buffer gas species, the relative values for the two cases should be reasonably accurate (i.e. $\sigma_{Sr-Ne} \approx \sigma_{Sr-He}$). Additionally they do provide

[9] The dominant Ne isotope is $^{20}Ne$, and this mass was used for these calculations.
[10] For which the most probable velocity is ∼106 m/s

an accurate order of magnitude estimate, a result which is approximately two orders of magnitude higher than the result of a hard sphere estimation with sphere radii ∼1 Å. With this corrected collision cross section in hand the collision can then be viewed in a simple hard sphere picture, where the effective sphere radii are larger due to the effects of the ion's field.

### Elastic vs. Inelastic Collisions

As indicated at the end of sec. 2.2.1, the coupling between a trapped molecular ion's motion and its internal states is poor, meaning that sympathetic laser cooling can efficiently reduce the translational temperature of the ion but not its ro-vibrational temperature. Such internal state cooling can be realized via collisions with cryogenic buffer gas.

The long-range, glancing collisions described previously in this section (i.e. those for which $b > b_c$) are primarily elastic in nature. Such collisions are only capable of transferring linear momentum between the particles, and thus can only cool the motional temperature of one of the collision partners. If this collision partner is a molecular ion, the effective temperature of the molecule's internal states is unchanged by the collision. This internal temperature can only be reduced via inelastic collisions with the buffer gas, in which energy from an internal state of the molecule is transferred to the buffer gas particle and carried away as linear momentum. Such collisions occur with high probability for impact parameters below the critical parameter of eq. 2.32.

A number of studies of the vibrational dynamics of atom-polyatomic molecule collisions have broadly shown that the cross section for vibrational energy transfer between the collision partners is of an order comparable to the geometric collision cross section between the two [47]. This is generally true for polyatomic molecules in the mass range studied in this work (∼100 Da), but this energy transfer cross section is generally much

lower for very small molecules ($\lesssim$5 atoms). Vibrational quenching via buffer gas is therefore relatively efficient for the mid-size polyatomics studied here, typically requiring $\lesssim$10 collisions, but is inefficient for smaller molecules (>100 collisions [48]). Efficient buffer gas cooling has been observed in some simple diatomics [49], however, illustrating that this correlation between molecule size and vibrational quenching efficiency is a general trend rather than a rule. In the case of an atom-molecular ion collision, the Langevin cross section of eq. 2.33 is a good approximation for this geometric cross section. Energy should therefore be transferred from a vibrationally excited molecular ion to a buffer gas atom at a rate equal to some fraction of the total collision rate, i.e. the inelastic collision cross section between the two species is comparable to the elastic collision cross section.

This rate is largely influenced by the density of states of the molecular ion, owing to the so-called energy gap law, which states that the most probable pathways for inelastically transferring a molecule's internal energy are those with the smallest energy difference between the molecule's initial and final states [50]. Accordingly, the greater the molecule's density of states is, the greater the number of nearby, accessible energy transfer pathways. Thus, a larger density of states corresponds to a greater probability of energy transfer, which is equivalent to increasing the inelastic collision cross section. It is for this reason that the cooling efficiency of rotational modes is particularly efficient, as the density of rotational states in a polyatomic molecule is exceedingly high.[11] It is also for this reason that the efficiency of cooling vibrational degrees of freedom via buffer gas is relatively high for mid-size polyatomic molecules, but rather low for small molecules. The cooling of vibrational degrees of freedom via cryogenic buffer gas should therefore be very efficient at buffer gas densities similar (within roughly one order of magnitude) to those required for efficient translational cooling.

[11] Of order $10^6$ states accessible at room temperature

### 2.3.3 Trapping with Buffer Gas

As described in sec. 2.1.2, the confining potential of an ion trap is approximately harmonic, and therefore conservative. Consequently, in order to load an ion into the trap there must be some means to dissipate energy from the ion once it has moved into the trapping region. This is achieved experimentally through collisions with cold buffer gas. To understand the effect of such collisions, consider a thermal ensemble of hard sphere particles of masses $m$ and $M$, where $m < M$. The average temperature change of the heavier $M$ species after undergoing one collision with a buffer gas particle can be written as [51]

$$\begin{aligned} \Delta T &= \frac{T_0 - T_b}{k} \\ k &\equiv \frac{(m+M)^2}{2mM} \end{aligned} \tag{2.35}$$

where $T_0$ is the initial temperature of the $M$ particle and $T_b$ is the buffer gas temperature.

Consider again $^{88}Sr^+$ ions immersed in He buffer gas. $Sr^+$ ions are produced in this work via laser ablation of a solid metal target with a frequency doubled, nanosecond pulsed Nd:YAG laser. While the dynamics of a laser ablation plume are complex and chaotic, ion temperatures within this plume are estimated to be on the order of 1000 K [52]. If $^{88}Sr^+$ ions were ablated directly into the ion trap, then evaluating eq. 2.35 for $T_0 = 1000$ K and $T_b = 13.5$ K shows that the average temperature of the $^{88}Sr^+$ ions decreases by $\Delta T \simeq 82$ K after a single collision event. In the case of a $^{20}Ne$ buffer gas at $T_b = 13.5$ K, this change becomes $\Delta T \simeq 298$ K. Thus, while eq. 2.33 showed the collision cross section between $^{88}Sr^+$ and Ne to be nearly the same as for He, eq. 2.35 shows that Ne cools the ions approximately 3.5× more efficiently. This result is among the reasons why Ne is a suitable choice of buffer gas species for ion loading.

Although the preceding example is illustrative, it is important to note that ions are not ablated directly into the ion trap in this work. Here ions are produced at a distance from the ion trap and transferred to the trap via ion optics (see sec. 4.3). In this loading scheme, ions typically enter the boundaries of the trap with a kinetic energy of approximately 3 eV ($\sim 3.5 \times 10^4$ K), and accelerate to 18 eV ($\sim 2.1 \times 10^5$ K) by the time they reach the trap center. The average collision energy between ions and buffer gas atoms is therefore significantly higher in this system. If an ion undergoes a collision immediately after entering the trap ($T_0 = 3.5 \times 10^4$ K), then the previous calculations yield $\Delta T_{He} \simeq 2.9 \times 10^3$ K and $\Delta T_{Ne} \simeq 1.05 \times 10^4$ K. Note that the relative cooling efficiency between the two species is the same, as the ratio $\Delta T_{He}/\Delta T_{Ne}$ depends only on the temperature-independent ratio $k_{He}/k_{Ne}$ when both gases are at the same initial temperature.

Eq. 2.35 can be recast in differential form as a function of the number of collision events, $\ell$, for which the following solution can be written [12] [51]

$$T_\ell = (T_0 - T_b)e^{-\ell/k} + T_b \tag{2.36}$$

Reorganizing eq. 2.36 to solve for $\ell$ given a desired final ion temperature $T_\ell$

$$\ell = -k \ln \frac{T_\ell/T_b - 1}{T_0/T_b - 1} \tag{2.37}$$

It is worth noting from the logarithmic form of this result that the experimental species will never completely equilibrate with the temperature of the buffer gas, and so the ultimate ion temperature achievable in practice will be some degrees warmer than the buffer gas temperature.

With the aid of eq. 2.37, the number of collisions necessary to cool an ion to a

[12] $dT_\ell/d\ell = -(T_\ell - T_b)/k$, where $T_\ell$ is the temperature of the ion after undergoing $\ell$ collisions

desired temperature can be estimated. It is instructive to first determine the number of collisions needed to confine an incoming ion, as this will require far fewer collisions than cooling will. Consider a $^{88}Sr^+$ ion entering the ion trap with translational temperature $T_0 = 3.5 \times 10^4$ K, which immediately begins colliding with Ne buffer gas at $T_b = 13.5$ K. As was shown in sec. 2.1.3 and sec. 2.1.4, the lowest effective trap depth for the trap used in this work is approximately 1 V. In order for an incoming $^{88}Sr^+$ ion to be confined, therefore, its kinetic energy must be reduced below 1 eV, corresponding to a translational temperature of $T_\ell = 1.16 \times 10^4$ K. Inserting these values into eq. 2.37 yields $\ell \approx 4$. With He buffer gas, this becomes $\ell \approx 13$. Additionally, these collisions must occur well before the ion entering the trap can reach the opposite side, otherwise its kinetic energy will be high enough to escape from the far side of the trap. The distance between the endcaps and the trap center in this work is approximately 1.7 cm, so that the mean free path of an ion entering the trap should be $\lesssim$1.5 cm. Given that the mean free path $\lambda \propto (\sigma\eta)^{-1}$, where $\eta$ is the density of gas particles, and using the previously estimated cross section for Ne collisions, the density imposed by this requirement is $\eta \approx 2 \times 10^{13}$ cm$^{-3}$.

This represents the minimum Ne buffer gas density required to trap an incoming $^{88}Sr^+$ ion. Recall, however, that trapping only requires a translational temperature below $\sim 10^4$ K. Many more collisions will be necessary to cool the ion to cryogenic temperatures. For $^{88}Sr^+$ at $T_0 = 3.5 \times 10^4$ K and Ne at $T_b = 13.5$ K, eq. 2.37 indicates that $\sim$34 collisions are necessary to cool the ion to 15 K, nearly an order of magnitude more than the loading requirement. This cooling is most efficient if the mean free path is again comparable to the trap length, indicating that a Ne buffer gas density of $\sim 2 \times 10^{14}$ cm$^{-3}$ is needed. This density is also more than sufficient for ion loading. Thus while the values calculated above are mere estimates, the order of magnitude result is instructive and indicates that both loading and cooling can be efficiently achieved at Ne buffer gas densities of order $10^{14}$ cm$^{-3}$. A simple ideal gas law analysis for this density at 13.5

K yields an approximate peak buffer gas pressure of ∼0.3 mtorr. As a result of the mass requirements for sympathetic cooling (see sec. 2.2.1), the molecules studied in this work are of a similar mass to $^{88}Sr^{+}$, meaning that these estimates should be reasonably accurate for the molecular ions studied in ch. 5 as well.

# Chapter 3

# Vibrational Spectroscopy

Prior to introducing the novel procedure implemented in this project, a brief overview of the relevant theory and techniques of vibrational spectroscopy is in order. This review is meant only to establish the minimum foundation needed to appreciate the experiments described in later chapters. Far more exhaustive theoretical and literature reviews of the subject are cited throughout this chapter.

## 3.1 Molecular Vibrations

In contrast to the simple atomic system whose state is described entirely by the quantum numbers of its valence electrons, the internal state of even the simplest molecule is made more complex by the presence of rotational and vibrational degrees of freedom. Molecular systems are therefore characterized by electronic, vibrational, and rotational states, with transition energies on the order of 100 THz, 1 THz, and 0.01 THz, respectively. A detailed understanding of the vibrational motion of polyatomic molecules is the focus of the research presented in later chapters. As will be discussed later in this chapter (sec. 3.3), the molecular energy scale which can be probed via the single molecule method developed here is approximately >1 THz. Low energy rotational motions are therefore difficult to observe with this technique, and only pure vibrational motions will be considered here.[1]

Each atom in a polyatomic molecule of $N$ atoms can be described by 3 laboratory frame Cartesian coordinates, thus giving the system $3N$ degrees of freedom. The description of these atoms' motion can be greatly simplified by choosing the center of mass (COM) of the molecule as the origin of the coordinate system, which decouples the rotational and vibrational motion of the atoms from the molecule's laboratory frame translational motion. Furthermore, if this coordinate system is constrained to rotate together with the molecule, then any small amplitude vibrational motion of the component atoms will contribute no angular moment to the system to zeroth order, thus decoupling vibrational motion from molecular rotation as well as translation [5]. As a result of this careful choice of coordinate system, vibrational motion can be treated independently of other molecular degrees of freedom. A total of 6 degrees of freedom are required to define

[1] In the context of conventional ro-vibrational spectroscopy, this restriction is equivalent to considering only $Q$-branch transitions, in which the initial and final rotational states of a molecule undergoing a vibrational transition are the same.

this rotating COM-frame coordinate system (3 Cartesian coordinates to define the origin at the COM, 3 Euler angles to define the rotation of the coordinates with the molecule), leaving a total of $3N-6$ degrees of freedom to describe the molecular vibrations.[2]

The classical Hamiltonian for the vibration of this system can be conveniently expressed in terms of the normal vibrational coordinates, $Q_k$. A normal mode of vibration is one for which the frequency and phase of each atom's motion is equal, thus causing all vibrating atoms to pass through their extrema and equilibrium positions in unison. Each normal mode of motion is characterized by a single normal coordinate $Q_k$, which itself can be written as a linear combination of the Cartesian coordinates of the vibrating atoms. The classical kinetic and potential energies are given by

$$K_v = \frac{1}{2}\sum_{k=1}^{3N-6} \dot{Q_k}^2 \qquad V = V(Q) \tag{3.1}$$

For a sufficiently small amplitude vibration, $V(Q)$ can be Taylor expanded about the equilibrium position of $Q$. One may choose $Q_{eq} = 0$ and $V(Q_{eq})$ can be arbitrarily chosen to be zero as well. The first order term of the expansion is zero at equilibrium ($\partial_Q V = 0$ at the potential minimum), leaving the harmonic term as the lowest order term of this expansion. In general this term is given by $\frac{1}{2}\sum_{ij}^{3N} F_{ij}Q_iQ_j$, where $F_{ij}$ is a force constant matrix linking the various normal modes. This matrix can be diagonalized, however, thus removing terms which contain more than one normal coordinate. Neglecting higher order terms in $V(Q)$ gives harmonic approximation of the classical Hamiltonian

$$H_v = \frac{1}{2}\sum_{k=1}^{3N-6} \left(\dot{Q_k}^2 + \omega_k^2 Q_k^2\right) \tag{3.2}$$

where the values $\omega_k$ are the terms of the diagonalized force constant matrix ($F_k = \omega_k^2$),

[2]One less Euler angle is needed to define the rotation of a simple linear molecule, therefore $3N-5$ degrees of freedom describe vibrations in this case.

which correspond to the frequency of the $k$th normal vibrational mode. Derivation of the quantum mechanical Hamiltonian for this system yields the same result, where the normal coordinates are replaced by the corresponding operators

$$\hat{\mathcal{H}}_v = \frac{1}{2}\sum_{k=1}^{3N-6}\left(\hat{P_k}^2 + \omega_k^2\hat{Q_k}^2\right) \tag{3.3}$$

As a result of the harmonic approximation for the potential, there are no coupling terms between the $k$ normal modes of oscillation, so that the Hamiltonian in eq. 3.3 is merely a sum of independent one-dimensional simple harmonic oscillator (SHO) Hamiltonians [4]. The eigenfunction $\Phi_v$ of $\mathcal{H}_v$ is therefore a product of $3N-6$ SHO eigenfunctions

$$\Phi_v(Q) = \prod_{k=1}^{3N-6}\phi_{v_k}(Q_k) \tag{3.4}$$

where $\phi_k(Q_k)$ is the wavefunction for the $k$th normal vibrational mode, with eigenvalue

$$\mathcal{E}_{v_k} = \left(v_k + \frac{1}{2}\right)\hbar\omega_k \tag{3.5}$$

and $v$ is the vibrational quantum number. This result, that the vibrating polyatomic molecule may be viewed as $3N-6$ independent harmonic oscillators, together with the harmonic potential of eq. 3.3, indicates that the transition frequency $\omega_k$ is related to a force constant opposing the motion of the oscillator analogous to the force constant in Hooke's spring potential. The restoring force for such an oscillator is dependent on the stiffness of the spring, corresponding to the vibrating atom's molecular bonds. All of this is to say that the vibrational frequency of a single oscillator in a polyatomic molecule is influenced by its bond environment, though the exact relationship is well beyond the scope of this chapter (see ref. [4, 5] for thorough discussions of this relationship). Information about these bonds can therefore be derived by measuring this vibrational

frequency, providing a significant motivation for the field of vibrational spectroscopy.

### 3.1.1 Selection Rules

The transition probability between the vibrational eigenstates $\phi_{v_k} \rightarrow \phi_{v'_k}$ is dependent on the transition dipole moment matrix element

$$\boldsymbol{\mu}_{v_k v'_k} = \left\langle \phi_{v'_k} \right| \boldsymbol{\mu} \left| \phi_{v_k} \right\rangle \tag{3.6}$$

where $\boldsymbol{\mu}$ is the dipole moment vector for the molecule, which is itself a function of the normal coordinates. As such $\boldsymbol{\mu}$ can be approximated by Taylor expanding about the equilibrium atomic coordinates and ignoring terms beyond first order

$$\boldsymbol{\mu} = \boldsymbol{\mu}_0 + \sum_{k=1}^{3N-6} \left( \frac{\partial \boldsymbol{\mu}}{\partial Q_k} \right)_0 Q_k \tag{3.7}$$

Here $\boldsymbol{\mu}_0$ is a constant, so that this zeroth-order term of $\boldsymbol{\mu}$ does not contribute to the transition matrix element. Eq. 3.6 therefore becomes

$$\boldsymbol{\mu}_{v_k v'_k} = \left\langle \phi_{v'_k} \right| \sum_{k=1}^{3N-6} \left( \frac{\partial \boldsymbol{\mu}}{\partial Q_k} \right)_0 \hat{Q}_k \left| \phi_{v_k} \right\rangle = \sum_{k=1}^{3N-6} \left( \frac{\partial \boldsymbol{\mu}}{\partial Q_k} \right)_0 \left\langle \phi_{v'_k} \right| \hat{Q}_k \left| \phi_{v_k} \right\rangle \tag{3.8}$$

Since the vibrational wavefunctions $\phi_{v_k}$ are eigenfunctions of the harmonic oscillator Hamiltonian, the normal coordinate position operator $\hat{Q}_k$ can be recast in terms of the harmonic oscillator ladder operators, yielding

$$\boldsymbol{\mu}_{v_k v'_k} = \sqrt{\frac{\hbar}{2\omega_k}} \left( \delta_{v'_k v_k + 1} \sqrt{v_k + 1} + \delta_{v'_k v_k - 1} \sqrt{v_k} \right) \tag{3.9}$$

where $\delta$ here is the Kronecker delta function. The immediate consequence of this result is the vibrational quantum number selection rule $\Delta v_k = \pm 1$, that is, only transitions which add or remove one quantum of vibrational energy to the $k$th oscillator in the molecule

are allowed. Such a transition is known as the *fundamental transition* for the $k$th mode.

### Vibrational Symmetry

The above selection rule restricts the change in the vibrational quantum number which is allowed given the approximations which have been made for $V(Q)$ and $\boldsymbol{\mu}$. Additional factors beyond the vibrational quantum number influence whether or not a transition is allowed in this approximation, however. Specifically, the symmetries of the vibrational eigenstates $\phi_{v_k}$ and the molecular dipole moment $\boldsymbol{\mu}$ affect whether or not the transition matrix element in eq. 3.6 is non-zero. Though written in bra-ket notation, this matrix element constitutes and integral over all normal coordinate space of the product $\phi_{v'_k}\boldsymbol{\mu}\phi_{v_k}$, where $\boldsymbol{\mu}$ is an implicit function of $Q$ as well. Such an integral from $-\infty$ to $+\infty$ is non-zero only if the integrand is symmetric. This restriction is true in general for any vibrational transition between any two vibrational states $\phi_{v_k} \rightarrow \phi_{v'_k}$.

In the harmonic approximation, the vibrational eigenstates are SHO eigenstates, thus the vibrational ground state $\phi_0$ is known to be totally symmetric. Whether or not a transition from the ground state to a vibrationally excited state is allowed therefore depends on the symmetry of both the excited state $\phi_{v'_k}$ and the components of the dipole moment vector $\boldsymbol{\mu}$. Furthermore, the symmetry of the excited vibrational state is simply that of the corresponding normal mode [4]. The transition matrix element from the ground state is therefore non-zero only in the case that the symmetry species of at least one of the components of the dipole moment vector is the same as the symmetry species of the excited vibrational mode. That is to say, $\Gamma(\mu_\alpha) = \Gamma\left(\phi_{v'_k}\right)$ for at least one component $\alpha = x, y, z$. Unlike the quantum number selection rule, this symmetry selection rule does not rely on any approximation, and thus takes priority over the quantum number selection rule previously derived. Only those transitions which satisfy this symmetry requirement are not forbidden, and of those transitions only those with $\Delta v = \pm 1$ are

allowed, thus yielding the full vibrational selection rule.[3]

### 3.1.2 Anharmonicity and Mode Coupling

Higher order terms in the approximations of the vibrational potential and molecular dipole moment were ignored in deriving eq.s 3.5 and 3.9, thus these equations are only valid if these higher order terms are negligibly small. This is a good first approximation, as anharmonic contributions to $V(Q)$ and $\boldsymbol{\mu}$ are generally much smaller than than the principal harmonic terms [4]. The effects of anharmonicity are frequently observable in real vibrational spectra, however, including in the spectra reported in ch. 5. A brief review of the effects of these higher order terms is therefore in order. Since two approximations were made in the derivations of the preceding results, two forms of anharmonicity may arise: electrical and mechanical.

#### Electrical Anharmonicity

Electrical anharmonicity refers to higher order terms in the Taylor expansion of the molecular dipole moment $\boldsymbol{\mu}$ used to approximate its value. The $\Delta v = \pm 1$ selection rule was derived on the assumption that terms beyond first order in this expansion are negligible. If the second order term is instead included in the approximation, additional terms appear in the approximation for the transition matrix element $\mu_{v_k v'_k}$ of eq. 3.8, of the form

$$\sum_{k=1}^{3N-6} \left( \frac{\partial^2 \boldsymbol{\mu}}{\partial Q_k^2} \right)_0 \left\langle \phi_{v'_k} \right| \hat{Q}_k^2 \left| \phi_{v_k} \right\rangle \tag{3.10}$$

As previously noted, the normal coordinate position operator $\hat{Q}_k$ is proportional to the

[3]The rotational state of a molecule does affect the symmetry of the molecular wavefunction, so that symmetry disallowed vibrational transitions can become allowed in a ro-vibrational transition of appropriate symmetry. Again, such transitions are neglected here.

SHO ladder operators, $\hat{Q}_k \propto \left(\hat{a} + \hat{a^\dagger}\right)$. As a result, $\hat{Q}_k$ acting twice on the eigenstate $\phi_{v_k}$ produces states with vibrational quantum number $v'_k = v \pm 2$. The matrix element in eq. 3.10 therefore leads to an additional selection rule $\Delta v = \pm 2$, and such a transition is known as the *first overtone*. The effect of electrical anharmonicity, i.e. higher order terms of $\boldsymbol{\mu}$, is to make harmonically forbidden overtone transitions allowed. In analogous fashion to the argument made for the first overtone, the *second overtone* with $\Delta v = \pm 3$ arises from the third order term in $\boldsymbol{\mu}$ which contains terms proportional to $\hat{Q}_k^3$, and so on. The transition matrix element for these overtone transitions is much smaller than for the fundamental transition, however, as the derivatives of $\boldsymbol{\mu}$ decrease in magnitude with order. Overtone transitions in real vibrational spectra are therefore of much lower amplitude, in general, than fundamental transitions (typically $\gtrsim$100$\times$ smaller).

### Mechanical Anharmonicity

While electrical anharmonicity refers to the higher order terms in the series approximation of $\boldsymbol{\mu}$, mechanical anharmonicity refers to the higher order terms in the series approximation of the vibrational potential energy $V(Q)$. Two primary effects arise from the inclusion of such terms in this potential energy. The most easily observed of these effects is a distortion of the energy level spacing of the molecular vibrational modes. The energy level spacing of the SHO is uniform, given by eq. 3.5. The asymmetry introduced into the molecular potential energy by higher order terms, however, leads to higher order terms in this energy relation as well. A first order perturbation treatment of the cubic term in the expansion of $V(Q)$ has no effect on the vibrational energy, but quartic and higher terms affect the vibrational energy to second order. The quadratic SHO potential is an accurate approximation of the true vibrational potential energy for small amplitude vibrations in which the displacement of nuclear positions from equilibrium is small. For larger nuclear displacements, the vibrational potential energy function deviates appreciа-

bly from a $(r-r_e)^2$ functional form. In practice, $V(Q)$ is often approximated by the well known Morse potential, which replicates the true vibrational potential more accurately than the harmonic treatment for larger nuclear displacements

$$V(r) = D_e\left(1 - e^{-a(r-r_e)}\right)^2 \tag{3.11}$$

This potential describes the relative vibration of two atomic nuclei bonded together, and is a function of the internuclear separation $r$. $D_e$ is the bond dissociation energy, $a$ is a parameter related to the vibrational force constant, and $r_e$ is the equilibrium internuclear separation. The Schrödinger equation can be solved analytically for this potential, and the resulting energy eigenvalues are no longer linear in the vibrational quantum number $v$, as in eq. 3.5, but are instead given by

$$E_v = \hbar\omega_k\left(v + \frac{1}{2}\right) + \frac{\hbar^2\omega_k^2\left(v+\frac{1}{2}\right)^2}{4D_e} \tag{3.12}$$

As a result, the energy levels of a given vibrational mode are no longer evenly spaced but instead decrease with increasing quantum number $v$ (see fig. 3.1). While the true vibrational potential differs from the Morse potential, the disagreement is smaller than for a harmonic potential. The Morse function is therefore a useful model to illustrate the effects of mechanical anharmonicity. This anharmonic effect impacts the previously discussed overtone transitions as well, so that overtone transition energies are not perfect integer multiples of the fundamental transition energy.

In the harmonic approximation, eq. 3.3 contains only terms which are proportional to $Q_k$, but no cross terms linking different normal coordinates. The second primary effect of mechanical anharmonicity is the introduction of such cross terms which are proportional to products between different normal coordinates. Although the cubic term in $V(Q)$ does not perturb the molecular energy levels to first order, it does introduce off-diagonal

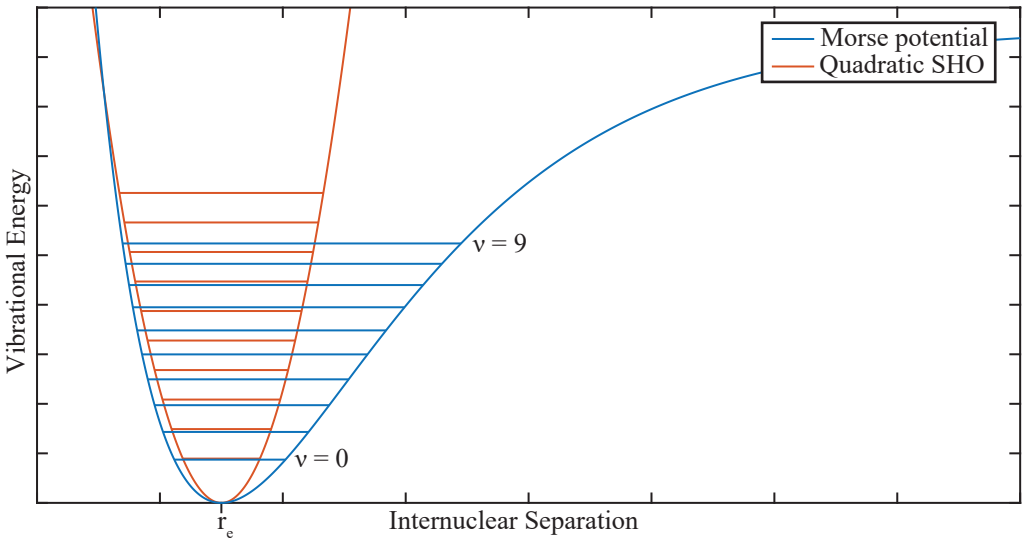


Figure 3.1: An example of a Morse potential function, plotted for arbitrary molecular constants, compared to a quadratic SHO potential given the same molecular constants. The energy level spacing in the harmonic approximation is uniform, but decreases with increasing vibrational quantum number $v$ in the more accurate Morse curve.

matrix elements into the molecular Hamiltonian of the general form $\frac{1}{6}\sum_{ijk} F_{ijk}\hat{Q}_i\hat{Q}_j\hat{Q}_k$. The three-dimensional force constant matrix cannot be diagonalized in the general case, leaving non-zero cross terms in the Hamiltonian which couple formerly independent normal modes to one another. While the non-zero elements of this matrix are generally small, the inclusion of these cross terms in the vibrational Hamiltonian prevents the molecular system from being viewed as a series of entirely independent harmonic oscillators. The possibility then exists that vibrational motion in one normal mode may affect the state of a separate normal mode within the molecule. The significant implications of this coupling are discussed in sec. 3.1.3.

Weak coupling of normal modes through mechanical anharmonicity may also lead to the appearance of *combination bands*, in which more than one normal mode is excited at the same time. Such a combination can be excited spectroscopically if the sum of the energies of the participating modes is equal to the incident photon energy, and if there is a sufficiently large 3rd or 4th order coupling term between those modes in the molecular

Hamiltonian. Since this coupling is generally weak, the transition dipole moment for combination bands is generally much smaller than for fundamental single mode transitions and thus combination bands tend to be spectroscopically weak. As a consequence of this, the effect of electrical anharmonicity on such combinations is smaller still; that is to say, the transition dipole moment for an overtone of a combination band, or for a combination band containing an overtone, is even smaller than for a simple, weak combination band. Thus combination transitions tend to consist of sums and/or differences of fundamental modes, each generally following the $\Delta v = 1$ selection rule.

Additionally, the same symmetry selection rule still applies for combination transitions. Recall that for single fundamental modes, the symmetry of the mode must equal the symmetry of at least one of the three Cartesian components of the molecular dipole moment in order to be allowed. In order for a combination transition to be symmetry allowed, therefore, the direct product of the symmetry species of each mode must contain the symmetry species of at least one dipole moment component. As an example, take a molecule with $D_{7h}$ symmetry, whose dipole moment has the symmetry species $\Gamma(\mu_{x,y}) = E_1'$ and $\Gamma(\mu_z) = A_2''$. Suppose also that this molecule has two normal modes $v_1$ and $v_2$ with species $E_1'$ and $E_2'$, respectively. Here, $v_1$ is symmetry allowed, since $\Gamma(v_1) = \Gamma(\mu_{x,y})$, but $v_2$ is not allowed since its symmetry species differs from all three dipole moment components. The combination $v_1 + v_2$, however, has symmetry $\Gamma(v_1) \otimes \Gamma(v_2) = E_1' \oplus E_3'$, which contains the $\Gamma(\mu_{x,y})$ species and is therefore symmetry allowed. A much more detailed explanation of the group theoretical analysis of molecular symmetry can be found in ref. [53]. In addition to illustrating the role of a combination's direct product symmetry, this example illustrates a further important aspect of combination transitions: the symmetry selection rule is only affected by the symmetry of the combination, not the component modes. As noted, $v_2$ is not allowed by symmetry in this example, but the $v_1 + v_2$ symmetry does satisfy the selection rule, thus the $v_2$ mode can

be excited as part of the combination in spite of being forbidden on its own.

### 3.1.3 Intramolecular Vibrational Redistribution

Perhaps the most important consequence of mechanical anharmonicity concerning the tagging spectroscopy technique outlined in sec. 3.3 is the process of intramolecular vibrational redistribution, or IVR. As indicated in sec. 3.1.2, the presence of cubic and higher order terms in the vibrational potential energy $V(Q)$ does not perturb the molecular energy levels to first order, but does introduce weak coupling terms between normal coordinates which would otherwise be independent in the harmonic approximation. As a result of this coupling, the SHO eigenfunctions are no longer the true eigenfunctions of the molecular Hamiltonian. The true basis states of this anharmonic Hamiltonian can, however, be expressed as a linear combination of SHO eigenstates, $\phi^a = \sum_j c_j \phi_j$. Solutions of the time-dependent Schrödinger equation for such basis states yield coefficients $c_j$ which vary in time, indicating that if a pure normal mode vibration is excited at time $t = 0$, the vibrational wavefunction can evolve in time to include other normal mode vibrations. Anharmonic coupling leads to "mixing" of independent SHO eigenstates in this sense. Thus, the vibrational energy deposited in a single normal mode can redistribute to other normal modes over time.

This redistribution process is of fundamental importance throughout chemistry, as chemical reaction rates and pathways are influenced by the vibrational states of participating molecules. A fundamental understanding of the distribution and time evolution of vibrational quanta in polyatomic molecules is therefore necessary to understand chemical dynamics. Both the manner and time scale by which this redistribution occurs have been the subject of extensive research [54, 55] in the decades since it was first observed experimentally [56].

Developing an understanding of the energy redistribution pathways in a polyatomic molecule is a non-trivial task which depends on many molecule-specific factors, and is therefore beyond the scope of this discussion. The redistribution time scale, though also dependent on species-specific factors, is a somewhat more tractable problem. Among the primary factors influencing this time scale is the density of molecular states. If a molecule exhibits a large density of ro-vibrational states $\rho$, then the decay rate out of an initially excited normal vibrational mode may be roughly approximated by Fermi's golden rule, which is linearly dependent on $\rho$ [57]. A larger state density therefore corresponds to a faster redistribution rate. The reverse is true for species with a low density of vibrational states, as there are fewer avenues for energy redistribution into a smaller manifold of states. The IVR time scale should therefore be shorter for larger, floppier molecules and longer for smaller, stiffer molecules, in general. Indeed this trend has been directly observed experimentally [58]. Ref. [57] summarizes several experiments which further illustrate this result, showing that the relationship between $\tau_{IVR}$ and $\rho$ is not universal across all similar systems, but does feature a general inverse trend. Many theoretical and experimental studies have concluded IVR time scales which span a broad range from 0.1-100 ps, and even up to 1000 ps for some species [54, 59], all of which is generally slower than the period of typical molecular vibrations. While this time-dependent energy flow has important implications for many important chemical processes, it is particularly critical for the action spectroscopy scheme described in sec. 3.3.

### 3.1.4 Real Vibrational Spectra

#### Frequency Range

With the preceding simplified description of molecular vibrations established, a few salient features of experimentally observed vibrational spectra are worth noting. Funda-

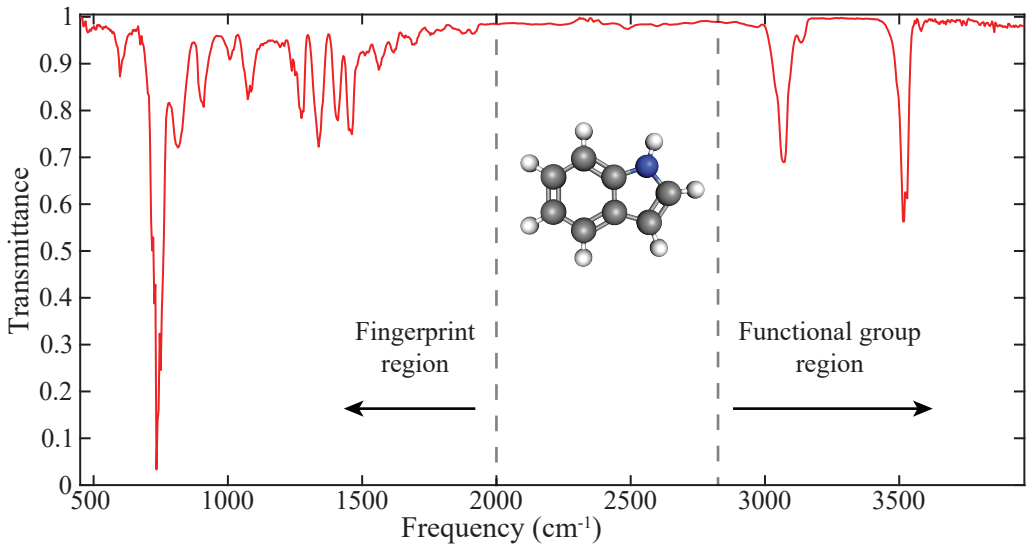


Figure 3.2: An illustrative example of a mid-size polyatomic molecule vibrational spectrum. The two primary bands in the functional group region are C–H (∼3070 $cm^{-1}$) and N–H (∼3500 $cm^{-1}$) stretching motions. The bands in the fingerprint region arise from C–H bending motions, skeletal deformations of the benzene and pyrrole rings, and many other difficult to assign motions. This data for indole ($C_7H_8N$) is taken from the NIST/EPA gas phase infrared spectrum database [60].

mental vibrational transition frequencies for polyatomic molecules typically lay between ∼12–120 THz, corresponding to the mid-infrared region of the spectrum. Traditionally, vibrational spectra are reported in units of wavenumbers, $cm^{-1}$, where 1 $cm^{-1} \approx 30$ GHz.[4] In units of wavenumbers, therefore, the frequency range for typical fundamental vibrations is ∼400–4000 $cm^{-1}$. An example of a proto-typical vibrational spectrum (indole, $C_8H_7N$) is shown in fig. 3.2.

In practice, this frequency range can be subdivided into two loosely defined regions: the fingerprint region, spanning approximately 400–2000 $cm^{-1}$; and the functional group region, spanning approximately 2800–4000 $cm^{-1}$.[5] The stretching vibrational motions which tend to occur in molecular functional groups (e.g. N–H stretching in amine groups, C–H stretching in methyl groups, etc.) are higher in energy and therefore frequency. Such

[4] E.g. a light field with frequency 3000 $cm^{-1}$ oscillates 3000 cycles over a physical distance of 1 cm.

[5] The region from ∼2000–2800 $cm^{-1}$ is relatively devoid of vibrational modes for mid-size (∼100 Da) polyatomic molecules, though this is only generally true.

stretching motions are therefore the namesake of this frequency region. The stretching motions of heavier atoms (e.g. C–C, C–N, C=O, etc.), by contrast, are typically much lower in frequency and lay in the fingerprint region. Bending vibrations, in which atoms move relative to one another without an appreciable change in their bond distance, also occur at lower frequencies in the fingerprint region (e.g. C–H bending motions, skeletal structure deformations, etc.). For molecules in the mass range considered here, the density of low energy fingerprint region vibrations is typically much higher than for functional group stretches. Additionally, since bending motions involve many more atoms than functional group stretches, these vibrations tend to couple more readily. All of these factors contribute to the fingerprint region of the spectrum typically being much more congested, making this spectral data challenging to interpret. As the name suggests, however, the pattern of vibrational modes observed in this range is unique to each molecular species. Thus, while it is challenging to assign all observed modes in this range, the combination of features here can be useful for distinguishing molecular species [61].

**Transition Linewidths**

The vibrational bands observed in fig. 3.2 are generally ∼30-50 $cm^{-1}$ full width at half maximum (FWHM), corresponding to ∼1 THz. The radiative lifetime of a two level system scales as the inverse cube of the transition frequency, $\nu^{-3}$, however. The natural linewidth for these transitions should therefore lay in the kHz range rather than THz. The Doppler width for a room temperature molecule (of order 500 MHz) is much larger than the expected natural linewidth, but still significantly smaller than what is observed. While this width will inevitably vary between molecular species, widths of this order are commonly observed in mid-IR spectra. This is due, in part, to the assumption made at the beginning of this chapter that vibrational and rotational motion can be treated

completely independently. In reality, the rotational state of a molecule often changes along with its vibrational state, meaning that the vibrational bands observed above have underlying rotational structure. The energy separation between rotational states is on the order of 1-10 GHz, and a large number of rotational states can be occupied in a thermal ensemble of molecules at room temperature. As a result, if the primary vibrational transition is addressed by a light source with spectral width broader than the rotational separation, then these "ro-vibrational" transitions will not be resolved. Underlying rotational features instead appear to run together, producing a single broad band with a width dependent on the rotational level spacing and molecular temperature. A more thorough discussion of ro-vibrational transitions is beyond the scope of this work, but can be found elsewhere [62].

## 3.2 Dissociative Action Spectroscopy

As illustrated in the preceding sections, the vibrational potential energy $V(Q)$ experienced by atoms in a polyatomic molecule determines the frequency at which different molecular vibrations occur. This potential energy is highly sensitive to the physical geometry of the molecule, as well as its local environment [63]. IR spectroscopy in the functional group region is a valuable analytical tool for identifying the presence of various chemical groups in larger molecules. IR spectroscopy in the fingerprint region, often in concert with theoretical calculations, provides a valuable probe of the skeletal structure and geometry of polyatomic molecules and, as the name implies, can serve as a useful bar code by which molecules can be identified [61].

The application of this sensitive probe to molecular ions has been a burgeoning field of research in the last few decades for multiple reasons. While the detailed structural information encoded in molecular spectra is invaluable for understanding their properties,

many molecules are difficult to analyze by conventional absorption spectroscopy methods. This is particularly true of solid and liquid phase molecules, which are challenging to analyze in the gas phase owing to their intrinsically low vapor pressures. Vibrational spectroscopy can instead be performed in the condensed phase, but such spectra are typically highly distorted due to interactions with neighboring molecules [64]. Interaction-induced effects therefore limit the amount of useful structural information which can be extracted from condensed phase spectra.

This challenge for low vapor pressure species can be circumvented by ionizing such analytes instead. Multiple techniques, such as electrospray ionization (ESI) and matrix assisted laser desorption ioinization (MALDI), have become standard tools for ionizing low vapor pressure condensed phase samples [65]. Once ionized, these analytes can be easily manipulated and isolated in the gas phase with standard mass spectrometry and ion optical tools. Simple IR absorption spectroscopy is still infeasible at this stage, as the mutual Coulomb repulsion of ions prevents one from creating a sufficiently high analyte density to detect absorption. A wealth of action spectroscopy methods have been developed and refined in recent years, however, to circumvent this limitation. Such methods marry the incredible sensitivity of modern mass spectrometry with IR spectroscopy, typically driving state specific photodissociation of analyte molecules followed by sensitive detection of molecular fragments via mass spectrometry [66]. The detection of these photofragments therefore serves as a secondary indicator of a photon absorption event, rather than observing absorption directly.

In addition to this ability to render low vapor pressure molecules spectroscopically accessible, ion action spectroscopy has enabled invaluable research into molecular ions themselves, which play important roles in a wide range of chemical environments. The constant presence of ionizing cosmic radiation in the earth's atmosphere continually produces ions which are important drivers of atmospheric chemistry and aerosol nucleation

[67, 68]. Biological systems rely on ions for electrical transport and signalling, and biologically relevant molecules often readily ionize in solution, thus making ions important components of most all biological processes [69, 70]. Although experimental evidence indicates that the conformational landscape of ions in the gas phase is different than for the solution phase, such experiments also suggest that solution phase conformations can be realized in the gas phase under certain ionization conditions [71]. If this can be realized experimentally, infrared ion spectroscopy would be able to provide highly accurate characterizations of the biomolecular structures actually present in biological environments. Infrared and radio astronomy studies have unambiguously observed numerous neutral and ionized molecules to be abundant in the interstellar medium, where ever present ionizing radiation produces molecular ions which drive astrochemical reactions [72, 73, 74]. Molecular ions play important roles in many more systems than these, but this truncated list helps to highlight their importance and thus motivate the significant work which has been done to characterize them spectroscopically.

### 3.2.1 Infrared Multiple Photon Dissociation

Infrared multiple photon dissociation (IRMPD) is arguably the most common technique of ion vibrational spectroscopy. The energies of vibrations in polyatomic molecules are typically much less than the lowest bond energy in the molecule, so that resonant IR absorption events are insufficient to dissociate the molecule. As a result of the IVR process described in sec. 3.1.3, however, the energy absorbed in such a vibrational excitation can rapidly propagate throughout the molecule and excite other vibrational modes provided that energy conservation is obeyed. Once this enery transfer has occurred, the vibrational mode which was originally excited is free to absorb another IR photon.

This process occurs on the picosecond time scale, much faster than the radiative

lifetime of typical vibrationally excited states. As a result, many IR photons can be absorbed by the resonant vibrational mode and redistributed to other modes in the molecule before any energy is radiatively released, effectively pumping several photons worth of energy into the various vibrations of the molecule. With the aid of a sufficiently intense IR light source, enough photons can be absorbed into the manifold of vibrational modes to surpass the lowest bond energy of the molecule before any radiative decay can occur, thus fragmenting the molecule. These photofragments can be readily detected with high sensitivity in a mass spectrometer. The rate of photofragmentation here is dependent on the detuning of the IR light source from a molecular resonance, so that a vibrational spectrum can be mapped by monitoring the fragmentation rate as a function of laser frequency.

As illustrated, this technique is conceptually very simple, whereby an experimenter needs only to focus a relatively intense IR laser into a mass spectrometer. This simplicity has contributed to the rapid adoption of IRMPD as a means of measuring ion vibrational spectra [75]. In spite of this widespread adoption, however, important challenges inherent to this technique have limited its utility. From a technical perspective, IRMPD can be difficult to implement for the fact that high IR laser intensities are needed to cause photofragmentation. There are very few commercially available tabletop light sources which can produce this level of power and are also broadly tunable. As a result, IRMPD has largely been limited to experiments involving free electron lasers (FEL). FELs readily satisfy the requirements for IRMPD experiments, but such light sources are highly complex and only exist at large user facilities, thus greatly inhibiting experimental operating time.

In addition to this practical consideration, IRMPD suffers from an important fundamental scientific challenge. The process described above is intrinsically non-linear. Each data point observed in a spectrum corresponds to a photodissociation event, but each

photodissociation event requires several photon absorptions to occur. This deposition of many vibrational quanta of energy into the network of molecular vibrational modes effectively heats the molecule, leading to red-shifting and broadening of observed vibrational bands [75, 76], in addition to altering their relative amplitudes [77]. Indeed it has been shown previously that molecular dynamics simulations can derive broadened, distorted IRMPD spectra from the high resolution spectra of cold molecules by simply increasing the effective molecular temperature to hundreds of kelvin [78]. These distortions therefore limit the resolution achievable with IRMPD and often severely complicate the comparison of observed spectra with *ab initio* calculations.

### 3.2.2 UV-IR Depletion

The detrimental effects of vibrational heating on the spectra observed via IRMPD arise from the fundamental complication that the energy of a typical IR photon is small compared to molecular bond energies. Since no single photon can dissociate an average analyte molecule, multiple mid-IR photons must be absorbed to induce fragmentation. A conceptually simple solution to this problem, therefore, is to increase the photon energy used for dissociative spectroscopy. This approach can be implemented in a two-photon scheme to record high resolution vibrational spectra using both mid-IR and ultra-violet (UV) light. In this method, known as UV-IR depletion spectroscopy, an energetic, pulsed UV light source at a fixed frequency drives a known transition between the ground vibronic state and an excited vibronic state, $S_0 v_0 \rightarrow S_1 v'$, of a molecular ion [79]. This transition energy typically exceeds the lowest bond energies of the molecule, leading to rapid dissociation. If the molecular ions are exposed to pulses of tunable mid-IR light prior to UV irradiation, then any pure vibrational transition driven by this light source will deplete the population of molecules resonant with the subsequent UV light pulse,

thus reducing the number of ions generated by driving the dissociative vibronic transition. These vibrational resonances therefore appear as dips in the observed photo-fragment flux produced from the analyte molecules.

Although this method relies on the absorption of two photons, it is a linear process compared to IRMPD. Each count observed in a spectrum corresponds to a photodissociation event, as with IRMPD, which is driven by a single UV photon. The dips in this dissociation signal, from which the vibrational spectrum is inferred, are the result of a single IR photon absorption which causes vibrational excitation out of the dissociative vibronic resonance. The resulting vibrational spectrum is therefore generated through single IR photon absorption events, significantly decreasing the issues of red-shifting and band broadening observed in IRMPD [79]. As a result, the achievable resolution with the UV-IR depletion method is significantly higher than for IRMPD [66]. In spite of these improvements, however, there are two primary practical considerations which limit the utility of the UV-IR method as a general analytical tool. The first is one of experimental complexity. A double resonance method such as this necessarily requires two independent light sources, a tunable mid-IR source as well as a tunable UV source, which increases both operational costs and complexity. Additionally, in order to implement this two-photon scheme, the UV dissociation spectrum of a given analyte species must first be measured to locate the relevant vibronic resonances before the vibrational spectrum can be measured through depletion. The second, more fundamental limitation, however, arises from the fact that not all molecules contain chromophores which absorb UV light. Thus, while many important systems are accessible by this method, the full reach of this technique is limited. Finally, it should be noted that, for all of their advantages and trade-offs, neigher IRMPD nor UV-IR depletion are adaptable to the single molecule case, as they intrinsically involve the destruction of the analyte molecule. The search for a suitable action spectroscopy scheme for extension to the single molecule regime must

therefore be expanded to methods which do not rely on direct analyte dissociation.

## 3.3 Tagging Spectroscopy

Although IRMPD and UV-IR dip spectroscopy are commonly used techniques in the study of molecular ions, the previously discussed disadvantages associated with these techniques makes them unsuitable for the pursuit of single molecule spectroscopy. The cryogenic messenger, or "tagging," method has many important advantages over both alternative techniques, and is much more amenable to implementation at the single molecule level. The single molecule method developed in this work therefore adapts the established cryogenic messenger method.

Since its first demonstration nearly four decades ago [80], tagging spectroscopy has proven to be among the most useful forms of action spectroscopy [81]. Here, trapped molecular ions are exposed to an inert, high density buffer gas which is typically cooled to cryogenic temperatures. After a ternary molecule-gas collision, one of two incident gas particles, $G$, carries energy and momentum away from the system. The second gas particle remains in close proximity to the molecular ion by conservation of energy and momentum. The electric field of the ion acts to polarize the tag particle, resulting in a weak, attractive van der Waals interaction between the induce dipole and ion field which binds the particle $G$ to the molecular ion $X^+$

$$X^+ + 2G \rightarrow X^+ \cdot G + G \tag{3.13}$$

$G$ is commonly referred to as a "tag," and will be referred to as such from here on. The strength of the van der Waals potential binding the tag to the molecule depends on both the polarizability of the tag and the geometry of the molecule, where more

polarizable tags will tend to attach with larger binding energies. The van der Waals interaction between the two is greatest when the tag is near the ion's charge center, thus molecules tend to gain tags near this point [82]. As noted, however, additional factors such as molecular geometry influence the tagging position and multiple tagging sites can be energetically competitive for certain tag-molecule combinations [83].

Tagging spectroscopy is made possible by the fact that the potential well for the molecule-tag complex is extremely shallow in general, with binding energies typically of order 100 $\text{cm}^{-1}$ for most combinations of tags and molecules [84, 85]. As a result, nearly all vibrationally excited states of the molecular ion are degenerate with a continuum state of the complex. If the molecule is driven to an excited vibrational state via a single photon, vibrational relaxation quickly redistributes energy throughout the molecule and causes kinetic energy to be transferred to the tag. The complex therefore quickly converts to a degenerate continuum state and dissociates

$$\text{X}^+ \cdot G + h\nu \rightarrow [\text{X}^+ \cdot G]^* \rightarrow \text{X}^+ + G \tag{3.14}$$

This is the well known phenomenon of predissocation, illustrated schematically in fig. 3.3. All vibrationally excited states of the tagged molecule complex are strongly predissociative, so that driving the molecule to any higher vibrational state results in dissociation of the complex. By combining the above process with mass spectrometry, the vibrational spectrum of $\text{X}^+$ can be readily observed by tagging the ion and monitoring the complex dissociation rate as a function of incident photon frequency $\nu$. Recall that the fundamental challenge to applying mass spectrometry to ion spectroscopy is the fact that IR photons are not energetic enough to dissociate a molecule. IRMPD addresses this issue by absorbing more IR photons, while UV-IR depletion increases the photon energy used to drive dissociation. The tagging method therefore adopts the inverse approach: decreas-

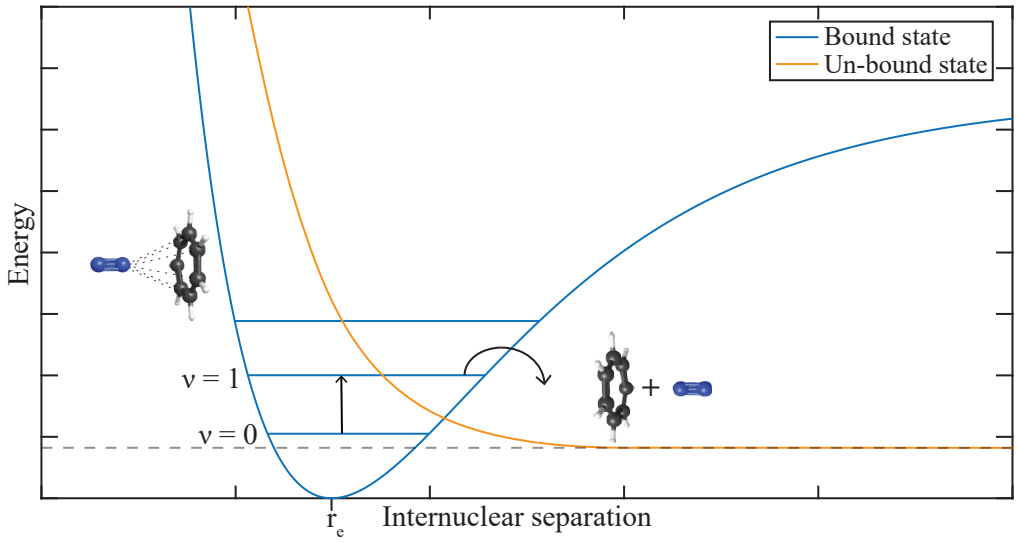


Figure 3.3: A very simplified schematic representation of the predissociation process. The first vibrationally excited level of the bound/tagged molecular ion is degenerate with an unbound/de-tagged state which is lower in overall energy. As a result, once the bound system is vibrationally excited it can rapidly transfer to the unbound potential leading to the radiationless dissociation of the tagged complex. This is illustrated with simple 1D potential functions, though in reality this process is described by a 2D potential energy surface.

ing the relevant "bond" energy (that of the tag) to enable dissociation ("de-tagging") by a single IR photon.

Such experiments are typically performed in a time-of-flight mass spectrometer (TOF-MS). Molecular ions are first mass filtered by a quadrupole mass filter and subsequently transferred to an ion trap. During this brief storage period, the ions are exposed to an intense pulse of cold buffer gas, which tags some fraction of the molecules. The contents of the trap are then passed through a long drift tube, where ions of different masses separate into groups of different mass, owing to their different mass-dependent drift velocities. It is in this stage that tagged and un-tagged molecules separate from one another. The tagged group is then exposed to mid-IR radiation after exiting the drift tube, where some fraction will resonantly de-tag. Tagged and de-tagged ions in a given mass group are then further separated by reflection from an array of reflectron

electrodes, before entering an electron multiplier detector. Integrating the resulting mass spectrum reveals the total number of molecular ions present. The ratio of the areas under the tagged and de-tagged mass peaks indicates the strength of the transition, as mid-IR light tuned closer to resonance will produce more de-tagged ions. This ratio therefore corresponds to the amplitude of the vibrational spectrum at the corresponding mid-IR frequency used in the measurement.

This leads to one of the most important advantage of the tagging technique compared to alternative photodissociation methods. As indicated in eq. 3.13 and fig. 3.3, only a single photon is needed to dissociate the van der Waals complex. A spectrum measured in this fashion is therefore linear, as opposed to IRMPD, and only requires light of a single frequency, as opposed to UV-IR depletion. This linearity simplifies important experimental constraints, particularly that of laser power, so that the tagging method can be implemented with lower power, turn-key, tabletop light sources. It also greatly simplifies observed spectra and enables straightforward comparison to theoretically calculated vibrational spectra [76].

It is also important to note that in addition to this benefit of linearity, tagging spectra are further simplified by the cryogenic nature of this measurement scheme. As a general trend, the number of energetically competitive conformational structures of a molecule increases with the size of the molecule. At the two extremes, for example, a simple diatomic molecule has only one isomer whereas large biomolecules can adopt one of many possible conformations [86]. Additionally, the number of energetically accessible conformations scales with the effective temperature of the molecule. As a result, an ensemble of room temperature molecules will exhibit more conformational structures than a cold ensemble will, each of which contributes unique features to an observed vibrational spectrum. Room temperature vibrational spectra of large molecules are therefore frequently very challenging to interpret [84, 87, 88] (see sec. 6.1). This also contributes to the

broadening issues which were discussed for IRMPD. Such complications are necessarily absent in tagging spectroscopy, however, as the buffer gas used to tag analyte molecules is typically cooled to temperatures on the order of 10 K. As was discussed in the preceding chapter, this cryogenic buffer gas efficiently reduces the internal temperature of analyte molecules, thus reducing the number of possible conformations which might be observed in an analyte ensemble. Higher energy conformations are therefore said to be "frozen out" for cryogenically cooled molecules, leaving the molecules in only the most energetically favorable conformational state(s) and significantly reducing the complexity of the resulting spectrum. Cryogenic buffer gas cooling has been combined with UV-IR depletion spectroscopy previously to achieve simpler and higher resolution spectra [89], but this benefit is a built in feature intrinsic to the tagging method.

### 3.3.1 Perturbative Effects

The vibrational spectrum of a tagged molecular ion extracted via the process described above is very nearly equal to that of a naked molecular ion. Nevertheless, the presence of a tag does slightly perturb the vibrational spectrum of the molecule. The positions and intensities of observed spectral lines usually differ from those of a tag-free molecule, but these shifts are typically quite small.

#### Frequency Shifts

As noted previously, tagging arises from the interaction between the induced dipole moment of a tag with the electric field of a molecular ion. This interaction asserts an attractive force on the tag, adhering it to the molecular ion, but it also asserts and equal attractive force on the molecule, thus slightly distorting the equilibrium positions of the nuclei. As a result, the vibrational potential energy surface seen by the various normal

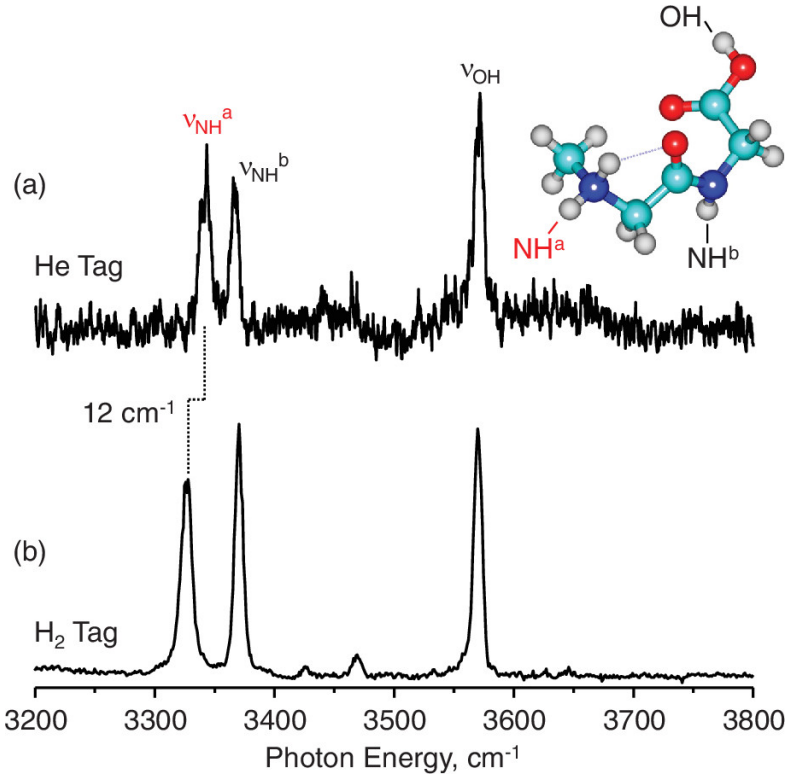


Figure 3.4: Tagging spectra of the SarGlyH$^+$ dipeptide [90]. Theoretical calculations in this study indicated a preferred tag binding site near the NH$^a$ group. *a)* He-tagged and *b)* $H_2$-tagged spectra illustrate the relative difference in tag-induced perturbations. The higher binding energy, more perturbative $H_2$ tag led to a red shift of 12 cm$^{-1}$ and 3 cm$^{-1}$ of the NH$^a$ and NH$^b$ modes, respectively, when compared to the less perturbative He-tagged spectrum. No relative shift is observed for the OH mode.

oscillator modes is slightly altered. More specifically, this perturbation tends to increase the internuclear separation of atoms in the molecule, thus slightly broadening the molecular potential well and red-shifting the vibrational energy levels. Tagging spectroscopy therefore tends to report transition frequencies which are slightly lower than the true frequencies of the bare molecular ion.

It is important to emphasize, however, the role that molecular geometry plays in such shifts and the relatively high degree of localization that this tag perturbation often exhibits. Consider, for example, the vibrational spectrum of the protonated dipeptide

$SarGlyH^+$ in fig. 3.3.1,[6] reported in ref. [90]. DFT geometry optimization calculations indicated that the most energetically favorable tagging site for this molecule lay near the N–H bond labelled *a* and highlighted in red in the figure. Vibrational spectra in the N–H stretching region were then recorded using two different species, He and $H_2$. Given that the polarizability of $H_2$ is nearly 4× greater than that of He [45, 91], the binding energy of the $H_2$ tag is generally larger, and thus more perturbative to the molecular frequencies. Indeed ref. [90] measured the binding energy of $H_2$ tags to this dipeptide to be ∼500 $cm^{-1}$, but cited calculated He binding energies closer to ∼100 $cm^{-1}$. This can be seen in the comparison between the two spectra, where $N–H^a$ transition in the $H_2$-tagged spectrum is red-shifted by approximately 12 $cm^{-1}$ compared to the same transition in the He-tagged spectrum.

Interestingly, however, the stretching frequency of the $N–H^b$ bond, which is physically further away from the tagging site, is only red-shifted 3 $cm^{-1}$ in the $H_2$–tagged spectrum compared to the He-tagged spectrum. Furthermore, the stretching frequency of the O–H bond on the opposite end of the molecule is not visibly shifted between the two spectra. This result illustrates several important aspects of tag perturbations on the true molecular vibrational frequencies. Firstly, the tag-induced frequency shift tends to be small, as illustrated by the magnitude of the relative shift between the two spectra. This shift also illustrates the dependence of the perturbation on the tag species, in particular on the polarizability/binding energy of the tag. Additionally, this result illustrates the relative localization of the tag perturbation. The tagging method is therefore capable of observing reasonably accurate vibrational frequencies for those modes laying closest to the tagging site, while observing very accurate absolute frequencies for modes which are shielded by distance from the effects of the tag.

[6]Reproduced from J. Chem. Phys. **140**, 221101 (2014), with the permission of AIP publishing.

**Amplitude Shifts and Symmetry**

The presence of a tag near a molecule slightly distorts both the potential energy surface $V(Q)$ as well as its derivative, $\partial_Q V$. This is simply the force constant for the normal mode SHO oscillator, however, corresponding to the transition matrix element. The strength of a given vibrational transition is dependent on the square modulus of this term, thus the presence of a tag near a molecule can alter the $y-$axis of the molecule's vibrational spectrum by changing the strengths of certain vibrational transitions. This effect is particularly pronounced in systems where more than one tagging site is energetically competitive. The same vibrational mode can be seen to be shifted to different frequencies for the different tagging positions, while also shifting in relative amplitude due to the effects on the curvature of the potential energy surface nearest each mode [6, 92].

Additionally, the change in the overall symmetry of the system can affect which vibrational modes are allowed by symmetry. This effect is typically smaller, as the change in symmetry due to a single tag is usually small. In the case of weak transitions, however, this perturbation to the symmetry selection rule can be strong enough to effectively suppress or allow such transitions between different tagging configurations [92] (see appendix B). A real example of this effect is observed experimentally in sec. 5.1.

### 3.3.2 Predissociation and Broadening

While the previously discussed perturbations introduced by the tag can act to limit the ultimate accuracy of the tagging method, the predissociation process itself further imposes fundamental resolution limits. As alluded to in the previous section, the vibrational spectrum of a tagged molecule can be measured in its entirety, even for transitions where the tag sits at some distance away from the relevant oscillator in the molecule. In

principle, only the normal mode closest to the tagging position should be observable in tagging spectroscopy, as only this mode can deliver energy to the weakly bound tag to drive dissociation. The fact that distant molecular vibrations are observable at all is a direct result of the IVR process discussed in sec. 3.1.3: if a normal mode distant from the tag site is excited, that vibrational energy can be redistributed over time into other molecular modes which lay closer to the tag site, until eventually a mode neighboring the tag begins to oscillate and causes predissociation. Additionally, this redistribution process is made even more efficient in the case of tagged molecular ions, as the tag itself can undergo low frequency oscillations in the shallow potential well binding it to the molecule. These slow vibrational degrees of freedom introduce additional modes into the density of states of the complex which can then facilitate more efficient coupling between modes of the molecular ion [93].

It is for this reason, for example that the vibrational modes in fig. 3.3.1 are observable, even though two of the three strong modes in that system are physically distant from the tagging site. This also leads to the relative insensitivity of more distant modes to the perturbative effects of the tag. Since the O–H oscillator in that system lays at the opposite end of the molecule from the tagging site, the potential energy surface for that mode is minimally perturbed by the tag and therefore the observed mode frequency is largely tag-independent. The mode can still be observed, however, because IVR allows O–H oscillator energy to propagate to the relevant N–H oscillator leading to de-tagging.

While this process enables all molecular vibrations to be observed, not just those closest to the tagging site, it also imposes fundamental limits on the achievable resolution of a tagging spectrum. As was noted in sec. 3.1.4, natural lifetimes for vibrationally excited states should be on the ms-scale given their 10 THz-scale transition frequencies. The IVR process, however, takes place on a time scale much shorter than this natural lifetime. As discussed in sec. 3.1.3, redistribution can occur anywhere from 0.1-1000

ps for different molecules. This therefore limits the observable linewidth for a given molecule to be of order 10-100 GHz (1-10 $cm^{-1}$). This is many orders of magnitude larger than the natural linewidth of typical vibrations, thus precluding the observation of natural vibrational linewidths in tagging experiments. This broadening mechanism is also two to three orders of magnitude larger than the effect of Doppler broadening of a room temperature molecular vibration, typically of order 100 MHz. While user-facility FEL systems, as well as a small number of high-end tabletop laser systems, can produce mid-IR light with a spectral width smaller than the 1-10 $cm^{-1}$ induced by predissociation broadening, the spectral width of many commercially available tabletop sources is comparable to the predissociation broadening limit. As a result, most reported tagging spectra are limited to linewidths of several $cm^{-1}$.

It is also worth noting that this $cm^{-1}$-scale broadening is comparable to, if not larger than, typical rotational constants for intermediate size polyatomic molecules. Ro-vibrational transitions are therefore difficult to resolve via tagging spectroscopy, though they have been partially resolved in smaller molecules with relatively large rotational constants [94]. Bands observed via tagging are therefore typically broadened, unresolved ro-vibrational contours, as discussed in sec. 3.1.4.

### 3.3.3 Destructive Detection

Although the point has already been made in the preceding discussion of the three principal forms of vibrational action spectroscopy, it is worth reiterating that each of these three methods is destructive to the analyte molecule. IRMPD and UV-IR dip spectroscopy both fundamentally rely on the dissociation of the analyte molecule. Tagging spectroscopy is not intrinsically destructive to the analyte, as it relies on dissociation of the tagged van der Waals complex rather than the analyte molecule itself. The TOF-MS

method of mass detection employed in conventional tagging spectroscopy *is* destructive, however, as it relies on high energy collisions of analyte molecules with an electron multiplying dynode in order to produce an electrical signal correlated to ion drift times. On this basis, therefore, none of these three techniques is suitable for single molecule spectroscopy. Since conventional spectroscopy methods interrogate an ensemble of molecules at once, information is obtained from each molecule in parallel, thus providing a large degree of statistical averaging across many molecules in one measurement. In contrast, spectroscopy of a single molecule requires many measurements to be performed sequentially on only one analyte. Sequential measurement is impossible, however, if the analyte is destroyed after every measurement, as is the case with the three methods highlighted above.

It is noteworthy, however, that tagging spectroscopy stands alone among these three as the only method which is not intrinsically destructive to the analyte. If an alternative mass measurement method could be employed instead of the destructive TOF-MS technique, then tagging measurements could potentially be performed sequentially on a single analyte molecule, thus enabling single molecule spectroscopy. It is for this reason, as noted earlier in this section, that the tagging mechanism was adapted in this work to achieve single molecule spectroscopy. This novel technique, referred to from here on as single molecule tagging spectroscopy (SMTS), exploits the features of trapped ions discussed in sec. 2.1.2 to achieve a robust, non-destructive mass measurement scheme, thus enabling sequential tagging measurements of a single analyte. The experimental details of this technique are discussed in the following chapters.

# Chapter 4

# Experimental Setup and Methods

This chapter introduces the various experimental systems developed in this work, their design and operating principles, and the relevant phenomena affecting their operation. The experimental methods using these systems to perform SMTS are also described. This information is summarized by a general outline of the SMTS experimental procedure at the end of the chapter.

## 4.1 Cryogenic Vacuum System

The ion trap in this system is operated at ultra-high vacuum (UHV), on the order of $10^{-11}$ Torr, in order to minimize the collision rate between trapped ions and background gas. This reduces the probability that collisions will occur that may increase the translational temperature or change the vibrational state of a trapped molecular ion. It also enables lower ion temperatures to be achieved through laser cooling and sympathetic cooling, increasing the spatial localization of the ions by reducing the number of collisions which move the ions away from the trap center. This pressure is achieved inside a custom built aluminum vacuum chamber, designed in-house and fabricated by Precision Cryogenics Inc©. The chamber, which is depicted in fig.s 4.1 and 4.2, is mounted atop a pair of large aluminum I-beams, which are themselves securely bolted to the underside of a large optical table. This geometry rigidly indexes the chamber to the optical table, in order to prevent any movement of the chamber relative to the table which would act to misalign the lasers described in sec. 4.5. The chamber has six removable panels which form vacuum seals via Viton™ fluoroelastomer o-rings against face seal glands. The o-ring seals are rated to $10^{-8}$ torr, which is therefore chamber. Lower pressures are achieved in the trapping region, however, due to cryo-sorption, as is discussed below.

A Sumitomo Cryogenics™ RDK-415D closed cycle, Gifford-McMahon style refrigerator is mounted to the top of the vacuum chamber, which acts as a dewar. High pressure helium flexlines are connected to the cryocooler on the atmosphere side of the chamber, providing refrigerant from a helium compressor, and the two-stage cold finger is suspended inside of the vacuum chamber. An ISO-K 160 face seal o-ring forms the vacuum seal at the cryocooler feedthrough on the top plate of the vacuum chamber. The cooler consists of two stages: a "warm" first stage which can cool a 45 W heat load to 50 K, and a colder second stage which can cool a 1.5 W heat load to 4.2 K. Minimum temperatures

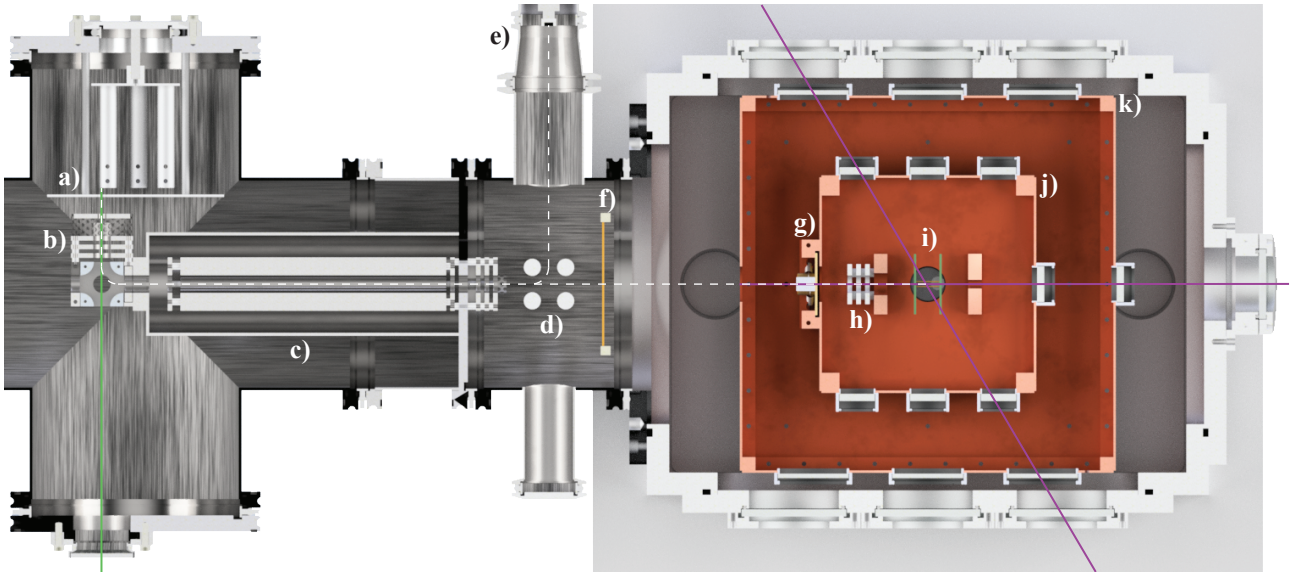


Figure 4.1: The experimental apparatus viewed in cross section, looking down from above the system. *a)* rotating holder for solid ablation (green beam) targets. *b)* EI ionizer. *c)* quadrupole filter. *d)* quadrupole bender. *e)* channel electron multiplier. *f)* up-down steering electrodes. *g)* cold mechanical shutter. *h)* einzel lens stack. *i)* quadrupole ion trap. *j)* inner radiation shield (5.7 K). *k)* outter radiation shield (60 K). The solid green line (left) represents the beam path of the 532 nm ablation laser (sec. 4.3.3). Dashed lines indicate the paths of ions through the system. Purple lines represent the combined $^{88}Sr^{+}$ cooling lasers (sec. 4.5).

below 3.5 K are attainable at the colder second stage, but with diminished heat load capacity. The vacuum chamber is evacuated prior to starting the refrigerator in order to minimize the amount of background gas which freezes onto the cold surfaces of the system. A dry scroll pump (Agilent IDP-07, 2.5 l/s) first pumps the vacuum chamber to a pressure of ∼50 mtorr, and a pair of turbomolecular pumps (Pfeiffer HiCube Eco 80, 67 l/s) reduces the pressure further to ∼0.2 mtorr. Finally, a high pumping speed (Agilent TV551, 500 l/s) turbomolecular pump attached directly to the main vacuum chamber is used to achieve a base pressure of $10^{-6}$ torr. This entire pumping procedure requires approximately two hours. The cryocooler is then powered on and reaches its base operating temperature after approximately two to three hours.

The blackbody spectrum emitted by 300 K bodies lies dominantly in the infrared, with

a peak emittance on the order of 10s of $W/m^2$ and peak wavelength on the order of 10 $\mu$m. Metals are typically highly reflective in the infrared; copper, for example, has a peak IR reflectance ∼90%. This means that of the blackbody radiation continually emitted by the room temperature vacuum chamber walls, on the order of several $W/m^2$ can potentially be absorbed by the two stages of the cryostat. Additionally, this radiation can negatively impact vibrational spectroscopy experiments by influencing the internal states of trapped analyte molecules [95], effectively increasing their rotational temperatures [96], which can lead to vibrational band broadening as discussed in sec. 3.1.4.

In order to prevent this radiation from burdening the heat load of the low capacity second stage and interacting with trapped molecules, a radiation shield is anchored to the 50 K stage and encloses (without contact) the second stage ($k$ in fig. 4.1). The shield is made of oxygen free high thermal conductivity (OFHC) copper panels bolted to a framework of OFHC copper bars. A small amount of Apiezon® N-grease is applied to the contact points between the panels and bars, increasing the thermal conductivity across these joints by nearly two orders of magnitude, while also decreasing the conductance of gas across these joints. Additionally, the steel bolts anchoring the panels in place are affixed with spring-loaded Belleville-type washers which ensure a large clamping force while cold. This shield ensures that 300 K blackbody radiation is absorbed by the high heat load first stage, while also reducing the peak emittance and wavelength of the blackbody spectrum to which the second stage housed inside this shield is exposed. In practice, the thermal burden of room temperature blackbody radiation absorbed by the outer shield is sufficient to raise the temperature of the outer shield from 50 K to 60 K. Importantly for the vacuum performance of the chamber, this radiation shield also acts as a cryo-pump, as background gas particles with freezing points above 60 K will freeze to the surface of the shield on contact. The pressure between the vacuum chamber and outer radiation shield is therefore limited by the pressure of gases with freezing points

below 60 K (e.g. He, $H_2$, etc.). During an average experimental run, the pressure in the volume between the vacuum chamber and first radiation shield (as measured via an ion gauge) is approximately $2 \times 10^{-8}$ torr. Additionally, as a result of its higher thermal mass, this radiation shield takes approximately eight hours to reach base temperature once the cryocooler is powered on.

In order to achieve lower pressures, a second, smaller OFHC copper radiation shield is anchored to the coldhead second stage ($j$ in fig. 4.1, the "inner radiation shield" as opposed to the "outer radiation shield"). Though the operating temperature of the cryostat stage to which the shield is mounted is 4.2 K, in practice this shield is held at a temperature of 5.7 K (see sec. 4.1.1). It is inside this second shield that the ion trap is housed, where the pressure is significantly lower due to the lower temperature of the cryo-pumping surfaces.[1] The pressure in this region is estimated by observing a pair of trapped ions. If a single $^{88}Sr^+$ ion and a single molecular ion are co-trapped, they will be well localized into two distinct equilibrium positions in the trap center. If these ions are imaged onto a camera, however, they will be observed to periodically exchange position (see fig. 2.5). Simulations have suggested that the energy needed for ions in a laser cooled Coulomb crystal to hop between equilibrium sites is <1 K [97], implying that this observed hopping in a two ion crystal can be attributed to background gas collisions. A measurement of this site hopping rate therefore serves as an estimate of the mean free time between collisions, thus constraining the background pressure.

### Pressure Estimate

In between experimental cycles, when many hours have elapsed since the last pulses of buffer gas were injected into the chamber, the ion hopping rate is observed to be ∼200 mHz, i.e. $\tau \simeq 5$ s. During typical experimental cycles, when buffer gas including He is

[1] E.g. The vapor pressure of $O_2$ at 4.2 K is $<10^{-56}$ torr, extrapolating down from 50 K.

frequently injected into the system, ion hopping rates are observed to be ∼10 Hz, i.e. $\tau \simeq 100$ ms. $H_2$ and He are the only two gas species with an appreciable vapor pressure at 5.7 K. In the periods between experimental cycles, it may therefore be assumed that the background gas is primarily $H_2$, while during experimental cycles it may be assumed to be primarily He, since the He vapor pressure is much higher than $H_2$. Applying the Langevin collision model of eq. 2.34 along with these assumptions, the observed hopping times correspond to average background gas pressures of approximately $8 \times 10^{-11}$ torr between experiments ($H_2$ limited), and $10^{-8}$ torr during experiments (He limited). These estimates, however, assume that each background gas collision imparts sufficient energy to the ions to induce hopping, which is unlikely to be the case. The two ion hopping energy can be estimated by comparing the potential energy for two ions laying along the trap axis to the potential energy for two ions rotated 90°, with a separation vector orthogonal to the trap axis. This energy difference is the energy required to rearrange the ions from the former position to the latter, at which point they may fall back to their axial orientation with exchanged positions.

The energy of a Coulomb crystal of two identical ions is the sum of the harmonic oscillator potential energy of each ion due to its displacement from the trap center with the mutual Coulomb repulsion between the ions [98]

$$U = 2\left[\frac{1}{2}m\omega^2\left(\frac{r}{2}\right)^2\right] + \frac{q^2}{8\pi\epsilon_0}\frac{1}{r} \tag{4.1}$$

Here $r$ is the distance between the ions along the Coulomb crystal symmetry axis, and the harmonic oscillator term is multiplied by a factor of two since the ions are symmetrically displaced from the trap center.

The energy required to cause the ions in such a crystal to hop is the difference in energy between a two ion crystal oriented along the trap axis ($z$-axis) and a two ion

crystal rotated by 90°, orthogonal to the trap axis; this represents the energy barrier which must be overcome to rotate the crystal by 180°. As previously noted in sec. 2.2.1, the observed axial secular frequency of $\omega_z/2\pi = 28$ kHz corresponds to an ion separation along the $z$-axis of approximately 50 $\mu$m. Inserting the observed $^{88}Sr^+$ radial secular frequency of $\omega_\alpha = 196$ kHz, eq. 2.30 yields an ion separation of approximately $r_\alpha \approx 13$ $\mu$m along the $x-$ and $y-$axes ($\alpha = x, y$). The energy difference between the axial and orthogonal configuration for this Coulomb crystal is therefore

$$\Delta U = m\left[\omega_\alpha^2\left(\frac{r_\alpha}{2}\right)^2 - \omega_z^2\left(\frac{r_z}{2}\right)^2\right] + \frac{q^2}{8\pi\epsilon_0}\left(\frac{1}{r_\alpha} - \frac{1}{r_z}\right) \tag{4.2}$$

Inserting the above values into eq. 4.2 results in an ion hopping energy barrier $\Delta U \approx 0.08$ meV. For the nominal background gas temperature in this system ($T = 5.7$ K), this indicates that $\Delta U \approx \frac{1}{6}kT$.

While this hopping energy is greater than the typical background gas kinetic energy for a 5.7 K Boltzmann distribution, it must be noted that a collision between a trapped ion and a background gas particle will not typically transfer the full kinetic energy of that gas particle to the ion. On average, some fraction of the gas particle's energy will be transmitted to the ion as kinetic energy, where this fraction is determined by the masses of the two particles [51, 98]

$$E_{transferred} = \frac{2m_{Sr}m_{gas}}{(m_{Sr} + m_{gas})^2}E_{gas} \tag{4.3}$$

For $^{88}Sr^+$ colliding with $H_2$ and He background gas, this expression indicates that only approximately 4% and 8%, respectively, of the background gas particle's kinetic energy will be transferred to the $Sr^+$ ion as kinetic energy, on average. An incoming background gas particle must therefore have a kinetic energy well in excess of the hopping energy ($\gtrsim 4\times kT$ and $\sim 2\times kT$ for $H_2$ and He, respectively) in order for the small fraction of that

energy which is transferred to the ion to exceed the hopping energy. If background gas of these two species is described by a 5.7 K Boltzmann distribution, then approximately 5% of $H_2$ molecules and 26% of He atoms will have kinetic energies which satisfy this criterion. As noted, the previous pressure estimates for these two species assumed that 100% of background gas particles were sufficiently energetic to induce ion hopping, but this result indicates that these estimated pressures must be scaled by approximately 20× and 4× for $H_2$ and He, respectively.

While these pressures are relatively high compared to typical room temperature ion trapping systems, they are more than sufficient to produce cold, localized Coulomb crystals. This is primarily due to the cryogenic temperature of the system, which results in the average energies of background gas collisions being significantly lower, and therefore less perturbative, than would be the case for room temperature gas.

### Cryogenic Aperture

Additionally, as will be seen in later portions of this chapter, ions are produced outside of the cryogenic radiation shields (far right of fig. 4.2, see sec. 4.3) and must be transported across the vacuum chamber to the trap center. A direct line of sight between the ionization region and the trap center is disadvantageous, however, as the background gas pressure in the region outside of the radiation shields is one to three orders of magnitude higher than that inside. A direct line between the outer vacuum region and the trap center would thus leave trapped ions exposed to a higher gas pressure and prone to suffer more collisions. This is remedied with the use of a cold shutter ($g$ in fig. 4.1). The shutter itself is a thin sheet of flat brass which is constrained to be nearly flush with the outside of the inner radiation shield by a pair of cold copper guide rails (see fig. 4.2). A braided stainless steel cable is mechanically anchored to the shutter at one end and to a linear motion feedthrough at the top of the vacuum chamber on the

other. This cable is pulled vertically (toward the top of fig. 4.2) to lift the shutter and expose a one inch aperture in the radiation shield wall behind it. A pair of stainless steel springs is anchored to the bottom of the copper guide rails and to the shutter, pulling it normally shut, and the motion feedthrough pulls the shutter against these springs to expose the radiation shield aperture, requiring approximately 5 s to open or close. Whenever the shutter is pulled open, ions generated outside of the cryogenic manifold can then pass through a permanently open aperture in the outer radiation shield, followed by the exposed inner shield aperture. When the shutter is closed, there is no path which molecules from the external vacuum chamber can follow to reach the ion trapping region without first undergoing several collisions with cryogenically cold surfaces. As a result, while the shutter fits only loosely against the radiation shield aperture, it effectively seals off the inner volume from the external chamber, as any undesirable contaminant gases will be cryo-pumped onto the cold stage of the cryostat before reaching the ion trap. Finally, a 12.5 mm hole is bored through the brass shutter and a sapphire window is mounted to it to allow optical access through the shutter when it is closed.

### 4.1.1 Vibration Isolation

Helium is pulsed into and out of the cryostat at a rate of about 1 Hz, which causes tangible vibrations in the system at this frequency. This vibration translates through the radiation shields, which are bolted to the cold finger of the cryostat, and into the ion trap itself, which is bolted to the cold radiation shields. This is therefore a constant perturbation to the trapped ions themselves, as it causes a regular, macroscopic shift in the spatial position of the trapping fields confining the ions. In order to remove this perturbation, the Sumitomo refrigerator used in this work was modified by ColdEdge Technologies™ to mechanically isolate the cold fingers from the refrigerator itself. A

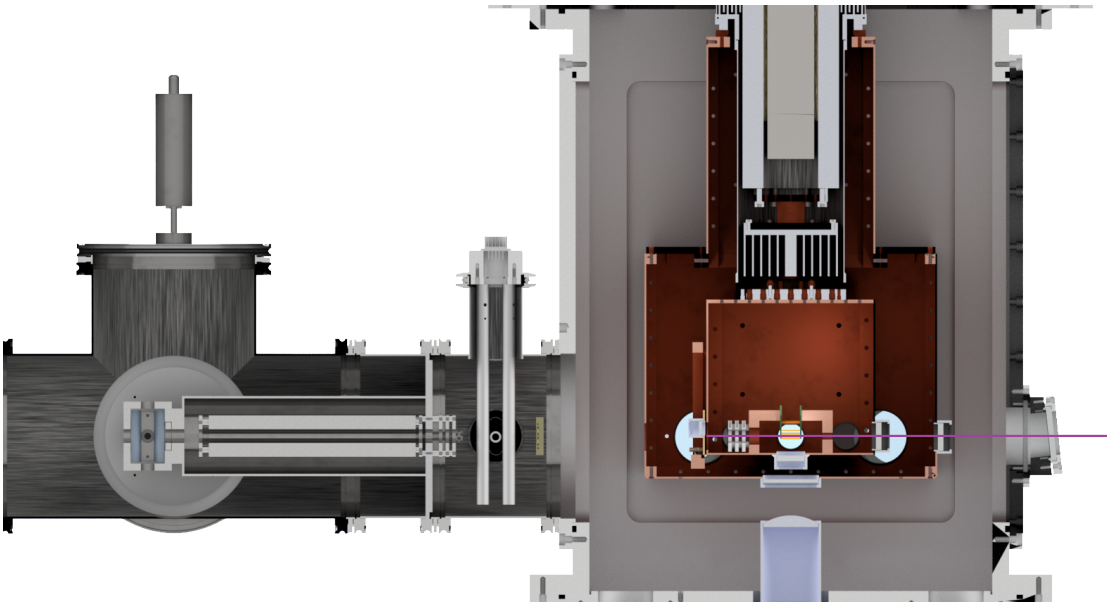

Figure 4.2: A 3D CAD model of the experimental apparatus viewed in cross section. On the left are the primary vacuum chamber, cryogenic manifold, and cryogenic ion trap. On the right is the mass filter chamber, where molecules enter through the leak valve (top right) and are ionized prior to trap loading. The interlocking heat exchangers of the cryocooler and vibration isolation stage are seen in cross section. A long working distance objective beneath the trap collects fluorescence light from laser cooled $^{88}Sr^{+}$ (axial cooling beam shown in purple).

cross-section of the modified apparatus is shown in fig. 4.2. Heat exchangers are bolted to the two stages of the refrigerator, comprising a series of concentric OFHC copper rings, with ∼2 mm between adjacent rings. The refrigerator is suspended inside of a canister, from which it is completely mechanically isolated. Two surfaces inside the canister, just below the two stages of the refrigerator, are fitted with similar heat exchangers, and the refrigerator is suspended such that the rings of the heat exchangers on the refrigerator and the canister interlock but do not make physical contact. The rings of the interlocked heat exchangers are separated by ∼1 mm. A loose rubber bellows is the only mechanical connection between the refrigerator and this canister, creating an enclosed volume in which helium gas is introduced. The gas flows into the space between the heat exchangers and acts as a thermal link between them, so that the 50 K stage of the refrigerator cools

the designated 50 K surface of the containment canister, and similarly for the 4.2 K stage. In this way, the cryostat cools the sleeve in which it is housed, while remaining mechanically isolated from it, allowing the outer cold surfaces of the containment sleeve to be free of 1 Hz vibrations.

It should be noted that this scheme for mechanical isolation of the ion trap from the pulsed valve of the helium cryostat imposes an intrinsic upper bound on the operating temperature of this system. The boiling point of helium is $\sim$4.15 K, meaning that if the cold stage of the cryostat were operated below this point, then the helium serving as the thermal link between the refrigerator and the isolation canister would liquefy. Such liquefaction substantially increases the degree of mechanical coupling between the refrigerator and sleeve, as vibrations propagate much faster and more efficiently through liquids than in gases. It is therefore necessary to operate the cryostat just above the boiling point of helium to prevent this small but detrimental mechanical link from forming. In practice, a series of small resistive heaters anchored to the inner radiation shield of the cryogenic manifold are used to maintain a shield temperature of $\sim$5.7 K. This is found to be sufficiently high to ensure that all helium in the vibration isolation stage remains gaseous throughout the experiment.

### 4.1.2 Optical Access

As will be illustrated in later sections of this chapter, the SMTS method developed here requires optical access to the ion trap center for both laser cooling and spectroscopy. This is achieved with a series of optically flat windows in the panels of the outer vacuum chamber and each of the cryogenic radiation shields, as can be seen in fig.s 4.1 and 4.2. With one exception, all windows on the outer vacuum chamber are 75 mm diameter, 5 mm thick fused silica with $\lambda/4$ flatness and anti-reflection coatings rated for 400-1000

nm. These windows are suitable for transmission of both $^{88}Sr^{+}$ laser cooling beams, as the transmission of these wavelengths through fused silica is ∼92%. The lone exception to this is the vacuum chamber window to the far right of fig.s 4.1 and 4.2. It is through this window that mid-IR light for vibrational spectroscopy enters the system (see sec. 4.5). The transmission of mid-IR light through IR-rated fused silica is only ∼40-85% across the frequency range of the mid-IR source used here (see sec. 4.5.2). A 50 mm diameter, 5 mm thick sapphire window ($\lambda/4$ flatness) is therefore used for this particular window, as the transmission of mid-IR light through sapphire is $\gtrsim$88% for all wavelengths relevant here (400-4000 nm). All vacuum chamber windows are clamped against o-rings, forming a face seal against the window surfaces themselves.

Sapphire windows are also mounted to each of the two cryogenic radiation shields. In both radiation shields, eight windows lay in the plane of the trap center for laser cooling and spectroscopy, and one window is beneath the trap for gathering and imaging fluorescence light from laser cooled $^{88}Sr^{+}$. The six windows in the outer shield which are parallel to the trap axis are 50 mm in diameter, while the two orthogonal to the trap axis are 25 mm (see fig. 4.1). The outer shield window beneath the trap is also 50 mm, while all windows in the inner shield are 25 mm in diameter. Sapphire is used here in part for its uniform transmission profile, but primarily for its high thermal conductivity at low temperature: ∼200 W/m·K at $T = 5$ K [99], compared to ∼400-800 W/m·K for OFCH copper. As a result of this high thermal conductivity, windows in the cold radiation shields cool to nearly the same temperature as the shields themselves, ensuring that there are no anomalously warm surfaces in the system which might elevate the average background gas temperature.

Sapphire windows are mounted inside of standard aluminum lens tube holders and held tightly in place with compressed spring washers to maintain a high clamping force while cold. These lens tube holders are then threaded into the copper panels of the

radiation shields. In order to verify that the sapphire windows are sufficiently cold, one of the inner shield windows (closest to the label $j$ in fig. 4.1) is replaced by an annular sapphire window with a 4 mm ∅ hole in the center of the window. A steel bolt threaded through this hole is used to hold a thermometer diode flush against the window while it is installed, thus measuring the temperature of the window center. During normal operation, with an inner radiation shield temperature of 5.7 K, the temperature of this test sapphire window is observed to be 7 K, indicating that the entire environment inside of the inner shield should be $\leq$7 K.

## 4.2 Buffer Gas System

The work detailed here is heavily reliant on the use of cryogenically cooled inert buffer gas. The novel SMTS method places several unique constraints on any potential gas delivery system, however. A custom buffer gas handling manifold was constructed to satisfy each of these constraints, and is detailed below.

### 4.2.1 Pulse Valves

The ion loading scheme used in this work relies on collisions with buffer gas to dissipate ion energy, as discussed in sec. 2.3. Additionally, cryogenic buffer gas mixtures are central to the tagging method of action spectroscopy. There is a direct competition, however, between the high buffer gas density needed for ion trapping and tagging and the need for UHV conditions to keep trapped ions Coulomb crystallized and well isolated from their environment. These conflicting demands can be satisfied with solenoid-actuated pulse valves. These valves are normally shut to prevent gas flow, but can be quickly opened and closed to allow brief pulses of gas to flow through a small exit orifice. Intense but finite pulses of buffer gas can therefore be injected into the ion trapping region to provide

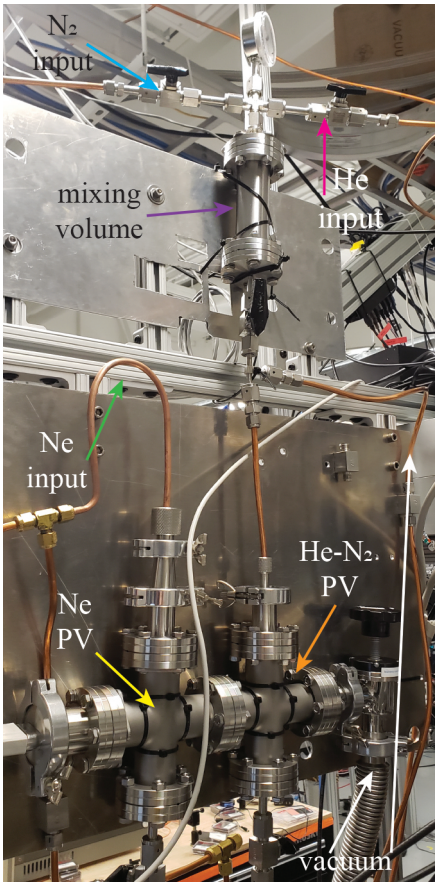


Figure 4.3: The custom UHP gas handling system used to deliver pulsed buffer gas into the ion trap. Two solenoid pulse valves (Ne PV and He-$N_2$ PV) are housed inside of the ConFlat© cross assembly at the bottom of the system, with one valve in each cross. The assembly is held under vacuum ($\sim 10^{-6}$ torr) so that the valves aren't exposed to air, which gradually diffuses into the valve bodies and contaminates the buffer gas. The Ne PV is backed by ~10 psig of UHP Ne, and the He-$N_2$ PV is backed by a mixture of UHP He and $N_2$ at ~14 psig. These two gases are loaded into the metal-seal mixing volume above the system in order to mix before experimental use.

a temporarily high buffer gas density, before this gas is rapidly pumped away through vacuum pumping and cryo-sorption.

A pair of solenoid pulse valves (Parker-Hannifin 009-1645-900) are used for this purpose. Within the valve assembly, a teflon poppet rests inside of a steel sleeve, and the poppet covers a 0.7 mm exit orifice to prevent gas behind the poppet from flowing through the orifice. This assembly is surrounded by a solenoid which can be quickly energized

with an external voltage pulse, producing a magnetic field which pulls the steel sleeve and poppet away from the orifice, allowing gas to flow. De-energizing the solenoid allows the poppet to move back into place, stopping the flow of gas again. This entire assembly is packaged in a small cylindrical body which is hermetically sealed via o-rings to isolate the gas behind the poppet from the atmosphere. As shown in fig. 4.3, this pair of solenoid valves is housed inside of a Conflat© cross assembly. This cross is external to the main vacuum chamber and is held under moderate vacuum ($10^{-6}$ torr). The outer surfaces of the pulse valves are therefore exposed to vacuum rather than the atmosphere. Experience has shown that if these valves were instead housed at atmospheric pressure, a minuscule amount of atmospheric oxygen would diffuse through the o-ring seals of the valve assembly and permeate into the backing gas. Even this trace amount of $O_2$ contamination in the buffer gas line is sufficient to cause deleterious chemical reactions with trapped analyte molecules and $^{88}Sr^+$ ions, thus necessitating the vacuum isolation of the valve assemblies.

### 4.2.2 Cryogenic Heat Exchanger

The two valves are backed by different gases: one by UHP Ne gas used for ion trap loading, and the other by a mixture of UHP He and UHP $N_2$ gas, used for molecular tagging. The choice of different buffer gases for these two applications is discussed in detail below. Gas pulses produced by each of the two pulse valves flow into a metal seal flexible steel bellows which connects to a feedthrough on the main experiment vacuum chamber. Gas flows through this feedthrough, into a second flexible steel bellows inside of the vacuum chamber, which is thermally anchored to the high cooling power stage of the cryostat. A portion of this bellows is therefore cooled to ∼60 K by the cryostat, and gas flowing through the bellows collides with the bellows walls and cools to approximately

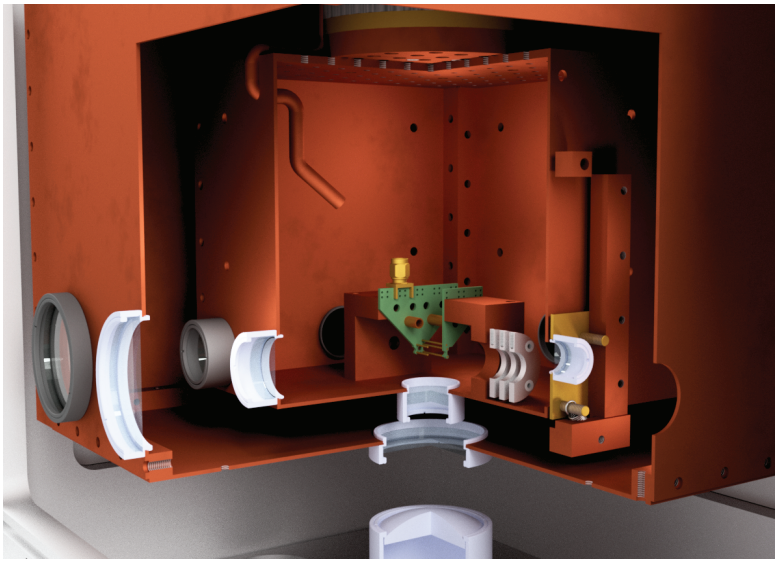

Figure 4.4: The quadrupole ion trap, cryogenic radiation shield assembly, and cryogenic heat exchanger all viewed in quarter-section. Buffer gas flowing through the heat exchanger undergoes seven different right angle turns, ensuring good thermalization to the tube temperature. The stainless steel shim which enables the exchanger temperature to be varied is not shown. The tube end is angled toward the trap center a few centimeters away.

this temperature. Buffer gas pulses then flow through a metal seal connection to a copper tube heat exchanger. The tube is thermally anchored to the low cooling power stage of the cryostat, which is held at 5.7 K. A stainless steel shim is sandwiched between the copper tube heat exchanger and the cryostat stage, providing partial thermal isolation. As a result, the temperature of the heat exchanger can be varied over a relatively wide range via resistive heaters (10-18 K) without significantly perturbing the temperature of the cryostat itself (see fig. 4.4). The heat exchanger tube contains seven different right angle bends, ensuring that gas flowing through the exchanger undergoes many collisions with the tube walls and thermalizes efficiently to the temperature of the tube.

Cooling buffer gas to this temperature range constitutes an essential purification step. $O_2$ and $H_2$ are the most detrimental contaminants present in the buffer gases used, where the former reacts readily with molecular ions and the latter reacts readily with

$^{88}Sr^{+}$. The cryogenic heat exchanger described here is typically operated between 13-14 K. Given the relatively high melting point of $O_2$ (54.8 K), this temperature range is sufficient to condense nearly all $O_2$ present in the buffer gas onto the walls of the heat exchanger tube. As a result, buffer gas which exits the heat exchanger into the ion trapping region is effectively free of $O_2$ contamination. Additionally, this operating temperature is just below the melting point of $H_2$ (14 K). $H_2$ contamination is therefore less efficiently condensed to the heat exchanger walls, but the fraction of $H_2$ which passes through the full heat exchanger circuit is much smaller than that which enters, due to the low vapor pressure of $H_2$ at 14 K ($\sim$55 mtorr [100]).

### 4.2.3 Gas Species

As mentioned, there are two primary applications of inert buffer gas in this experiment: ion trap loading, and ion tagging. Each application has different requirements, and there is no single buffer gas species which meets the requirements for both. This is the underlying motivation for this custom gas manifold with two separate pulse valves, containing two distinct buffer gas mixtures.

#### Trapping Buffer Gas

Ne gas is ideally suited for ion trap loading. The 27.1 K boiling point of Ne is low enough that it can be cooled to a very low temperature ($\sim$14 K) while still exhibiting a modest vapor pressure (0.1 torr [101]). This vapor pressure becomes effectively zero at 5.7-7 K, however, so that Ne can only exist in the trapping region for a very brief amount of time. The loading process is described in greater detail in sec. 4.3.3, but this convenient thermal behavior of Ne allows pulses of gas to be pre-cooled to $\sim$14 K before exiting the heat exchanger. A high density of cold Ne gas then passes through the ion

trap center, where it can collide with incoming ions to reduce their kinetic energies for trapping. This intense gas pulse is then immediately removed from the trapping region through cryo-sorption to the cold surfaces inside the inner radiation shield. The high gas pressures needed for trap loading can therefore be achieved and immediately followed by a return to high vacuum conditions.

### Tagging Buffer Gas

Ne was also chosen as the tagging species during the initial development stages of the SMTS method. Its 20 Da mass provides a high contrast between the tagged and un-tagged states of analyte molecules during mass spectrometry, allowing for accurate detection of tagging and de-tagging. Additionally, its relatively low polarizability results in a lower tag binding energy and is therefore less perturbative to the analyte molecule. This should result in vibrational spectra with greater absolute frequency accuracy. In practice, however, tagging with Ne proved entirely infeasible. Ne is indeed routinely used in conventional tagging experiments [102, 103, 104], but these experiments typically operate at a repetition rate of 10 Hz and tagged molecule complexes need only remain intact for 100 ms. In this experiment, however, spectroscopic interrogation of tagged molecules can last for several minutes at a time, thus it is necessary for tags to remain attached for at least many minutes at a time. The average Ne tag lifetime observed in this system, however, was less than one second, sufficient for conventional tagging but impractical for SMTS.

Molecular nitrogen, with a polarizability nearly $4 \times \alpha_{Ne}$ [105], is instead used for molecular tagging. This is not to say that pure $N_2$ gas is used for tagging, however; two principal factors make this infeasible. Firstly, pure $N_2$ gas cannot be cooled to very low ($\sim$14 K) temperatures before pulsing into the trapping region in the same way that Ne can, as a result of its 77 K boiling point; the vapor pressure of $N_2$ is simply far too low

at 14 K to be able to create intense burst of $N_2$ near this temperature. Additionally, if the density of $N_2$ in the trap center were to become too high, more than one three body collision with an analyte molecule could occur and leave the molecule with more than one tag. The higher the density of $N_2$, the greater the total number of tags which could be attached, and the greater the frequency with which multiple-tagging would occur. In extreme cases, molecular ions can be lost from the trap through this process, where the molecule gains so many tags that it becomes too heavy to stably confine.

For both of these reasons, a mixture of He and $N_2$ gas is used for tagging, rather than pure $N_2$. The exact ratio of this mixture fluctuates slightly from experiment to experiment, but is typically maintained at $\sim$80% He$-$20%$N_2$. He functions as a carrier gas to deliver the smaller quantity of $N_2$ to the trap, thus eliminating both of the issues associated with using pure tagging gas. He does not freeze at pressures below one atmosphere. When the He–$N_2$ mixture flows through the cryogenic heat exchanger, therefore, the He gas quickly and efficiently thermalizes to the heat exchanger temperature. The rarer $N_2$ gas, however, is effectively entrained in the flow of He through the heat exchanger and reaches the exchanger walls much less frequently than the He carrier gas. The net effect is that the $N_2$ tagging gas is efficiently cooled to the exchanger temperature at 14 K without colliding with the exchanger walls and freezing, thus cooling the gas to 14 K while keeping it in the gas phase. Additionally, the very low polarizability of He [45] means that it tags to molecular ions with very low efficiency. Three body collisions between molecules and He atoms therefore very rarely result in tagging, while three body collisions involving one He atom and one $N_2$ molecule will efficiently tag. The He carrier therefore acts to dilute the tagging gas density to prevent multiple-tagging events.

To form this mixture, a small metal-seal vacuum nipple is placed in the fore-line of the second solenoid pulse valve (see fig. 4.3). UHP He and UHP $N_2$ manifolds are connected to this volume through ball valves, and the pressure in this region is monitored

via a mechanical gauge. The nipple is evacuated to $10^{-6}$ torr by a turbomolecular pump (Pfeiffer HiCube Eco 80), then charged to a pressure of ∼7-8 psig (21-22 psi) of UHP He. The He manifold is then isolated from the volume, and an additional 4-5 psi of $N_2$ gas are added to the volume. All valves on the nipple are then shut, and it is left to sit for approximately two hours to allow the gases to mix evenly. The resulting mixture then backs the pulse valve, which injects bursts of the gas into the trap center for tagging.

## 4.3 Quadrupole Mass Filter

Ions in this apparatus are produced via laser ablation and electron impact (EI), and are filtered by mass via a commercial quadrupole mass filter (QMF) prior to loading into the ion trap. The use of a QMF is relatively unique among laser cooled ion trapping systems, and was chosen to address specific technical challenges which are unique to this experiment.

### 4.3.1 Laser Ablation and Stray Charges

The first generation of this experiment employed laser ablation near the ion trap for ion generation. This process quickly proved itself untenable, however, for three principal reasons related to the uncontrolled nature of the ablation process. Firstly, ablating a solid target within the cold second stage of the cryostat releases a large plume of charged particles. Recall that this region and all surfaces in it are held at ∼6-7 K, acting as a very efficient cryo-pump and therefore rapidly accruing many layers of dielectric ice (mainly in the form of frozen air). As a result, even though most of the cryo-pumping surfaces in the chamber are well grounded conductors, the charged ions released in an ablation plume cannot be efficiently dissipated when they reach these surfaces. Instead they embed in layers of dielectric ice and the electric fields produced by these charges are

not fully dissipated. Repeated ablation events are therefore capable of rapidly producing extremely large stray electric fields within the trapping region, potentially >1 V/cm. Additionally, this field environment changes with each successive ablation pulse as more ions are deposited into the system. These large, unpredictable, and constantly varying fields act to displace the ions from the RF null at the center of the ion trap, which acts to increase the micromotion and RF heating of trapped ions and thus decreases the stability of the trap.[2] Additionally, since stray electric fields distort the pseudo-potential confining the ions, the secular frequencies of oscillation of trapped ions in this environment are affected by the build up of stray charges. This manifests as macroscopic shifts over time of the observed secular frequencies.

The second issue regarding ion loading via ablation near the trap is related to the first: in addition to releasing a large plume of ions, ablation releases a large plume of neutral particles from the ablation target as well. In the specific case of $^{88}Sr^{+}$ this is particularly detrimental. Neutral Sr released in an ablation plume coats onto the surfaces of the ion trap in the same way that ions do, but these neutral atoms do not produce deleterious electric fields. This deposition of neutral Sr still leads to stray charge accumulation, however, as a result of the photoelectric effect. The work function of neutral Sr (2.59 eV [106]) is appreciably lower than the energy of the 422 nm laser light (2.94 eV) to which the trap is continually exposed for laser cooling. As a result, neutral Sr deposited onto the surfaces of the trap continually emits photoelectrons into the trapping region, which embed in dielectric ice on the trap surfaces in the same way that ions from the ablation plume do. This further contributes to the stray electric field environment around the trap and further distorts the pseudo-potential. Furthermore, since this photoelectron emission occurs continually, the trap secular frequencies continue to drift over time even in the absence of ablation pulses. As a result, even if the total number of ablation events

[2]In extreme cases ablation-induced fields can prevent trapping altogether.

is restricted, the trap secular frequencies can remain unstable for long periods of time.

The third issue related to ablation is the lack of control over the ablated species. Since ablation is a non-resonant process, any atomic or molecular species with sufficiently low ionization potential can be ablated by the same laser. As an example, the source of atomic Sr used to create $^{88}Sr^+$ throughout these experiments was a small alloy rod composed of 90% Al and 10% Sr. This means that each ablation event which was intended to create $^{88}Sr^+$ ions also created many $Al^+$ ions, as well as isotopes of Sr like $^{87}Sr^+$. Depending on the Mathieu parameters in use, this could readily lead to trapping of unwanted $Al^+$ ions, along with ions of any number of potential impurities in and on the target as well. These unwanted guest ions act to deplete the already small sympathetic cooling capacity of the intentionally loaded $^{88}Sr^+$ hosts. This means that the ultimate temperature of these ions that can be reached through laser cooling of $^{88}Sr^+$ is increased, making the entire trap warmer and less stable. Additionally, unwanted guest ions are often difficult to controllably eject from the trap, especially when present in large numbers. In practice, the entire trap must typically be emptied to remove these guests, significantly slowing down the data collection process.

These issues are avoided in traditional ion trapping experiments via the use of photoionization [107]. Here, a high temperature oven produces a beam of neutral Sr vapor, which is directed through the ion trap. 461 nm and 405 nm lasers drive a two-step photoionization transition to resonantly ionize neutral Sr atoms in the trap center, leaving them confined. This loading scheme does address the direct charge deposition issue intrinsic to laser ablation as well as the issue of species selectivity, as the resonant ionization process will only produce $^{88}Sr^+$ ions. However the deposition rate, and corresponding photoelectric charging rate, for neutral Sr is significantly worse in this scheme than for laser ablation given the high flux of neutral Sr which ovens produce. Furthermore, the issues of selectivity and charge deposition remain for the analyte molecules which must

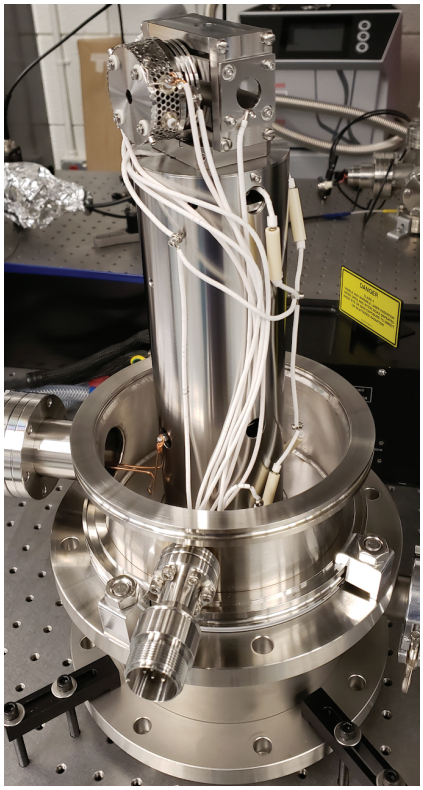

Figure 4.5: The QMF used in this work. The electron impact ionizer (perforated metal volume) is perpendicular to the axis of the quadrupole, and the exit aperture of the QMF is facing down toward the optical table in this image. An electrostatic quadrupole bender directs ions exiting the ionizer to travel down the quadrupole axis.

be produced for molecular spectroscopy experiments, as each molecular species would require different laser wavelengths for resonant photoionization.

### 4.3.2 Mass Filter Setup

For these reasons, a commercial QMF is employed to controllably load small numbers of guest ions into the trap, mitigating charging issues and controlling guest species by mass. A custom mass filter from Extrel CMS™ was used in this work (shown in fig. 4.5). The system comprises an electron impact (EI) ionizer and RF quadrupole, with DC ion optics between the two and after the quadrupole (right portion of fig. 4.2). This system is mounted to an ISO-K 160 blank welded to a short (10 cm) nipple, and housed inside

of a 5-way ISO-K 160 cross. This volume is only linked to the main vacuum chamber through two small (12.5 mm ∅) apertures, so that the chamber remains at a relatively high pressure ($\sim 10^{-5}$ torr) when pumped on by the vacuum pumps described in sec. 4.1. This volume is differentially pumped by an additional turbomolecular pump (Pfeiffer HiCube Eco 80, 67 l/s), which helps to further reduce the QMF chamber pressure to approximately $2\times 10^{-7}$ torr when the crycooler is cold. Like the panels of the vacuum chamber described in sec. 4.1, the ISO flanges of the QMF employ Viton™ o-rings, and are therefore similarly constrained to ultimate pressures on the order of $10^{-8}$ torr.

The EI ionizer is oriented at a right angle relative to the quadrupole axis. Gas phase molecules are ionized by the emission current running across a hot filament, and are then bent 90°and pass through a focusing lens before entering the quadrupole. The QMF radially confines the ions using the same principles as the linear quadrupole ion trap (recall sec. 2.1.1), and the Mathieu parameters of the QMF are tuned to allow stable radial confinement of only one mass species at at time.[3] In this way the QMF allows only specific mass species to propagate stably along the axis of the quadrupole, with all other masses being radially ejected before reaching the far end of the poles. The mass selected ions then pass through an electrostatic Einzel lens upon exiting the quadrupole, which focuses the stream to a tunable focal point.

The axis of the QMF is co-aligned with the ion trap so that ions can be injected axially into the trap. An electrostatic quadrupole bender lies between the QMF and the ion trap, with an inscribed radius equal to the diameter of the QMF exit aperture (12.5 mm, $d$ in fig. 4.1). The electrodes of this bender are oriented perpendicular to both the ion trap axis and the plane of the optical table on which the experiment sits. Between this bender and the ion trap is an additional pair of electrodes oriented parallel to the

[3]Recalling eq. 2.7, the QMF varies its Mathieu parameters by varying $V_0$ and $U_0$, while keeping $\Omega_T$ fixed.

optical table (thus orthogonal to the bender) and with the same electrode spacing as the bender. In mass filter mode, these electrodes are used to steer the ion beam from the QMF, with the bender controlling the "left-right" motion of the beam, and the horizontal electrodes controlling the "up-down" motion. In practice, little beam steering is needed for effective ion loading, thus a uniform $-15$ V is applied to all six electrodes in this configuration, helping to approximately "collimate" the ion beam as it leaves the filter.

A channel electron multiplier (CEM) is located after the QMF exit and orthogonal to the QMF axis. In mass spectrometer mode, the quadrupole bender voltages are adjusted to bend the filtered ion beam 90° toward the CEM ($e$ in fig. 4.1), which is held at a large negative potential (-2 kV). Ions colliding with the CEM produce voltage pulses which are amplified and sent to an electronic counting module which monitors the count rate as a function of the mass filter setting, thus producing a mass spectrum. An example of such a spectrum is shown in fig. 4.6. This mode is typically used to characterize the tuning of the QMF by analyzing background gas in the QMF chamber, the composition of which is largely invariant over time. In this mass spectrometer mode a static voltage is applied to opposing pairs of the quadrupole bender electrodes of approximately $\pm 1/2$ of the ionizer potential, corresponding to $\pm 1/2$ of the kinetic energy of incoming ions (discussed in more detail in the following section). Fig. 4.6 illustrates the mass selectivity of this filter, where observed mass peaks are typically $\leq$0.2 Da/z full width at half maximum (FWHM).

### 4.3.3 Loading Atomic and Molecular Samples

The QMF is used to filter both atomic and molecular species before loading into the ion trap. Molecular ions are produced directly from the gas phase, where they are introduced into the QMF ionizer through a stainless steel all-metal leak valve connected

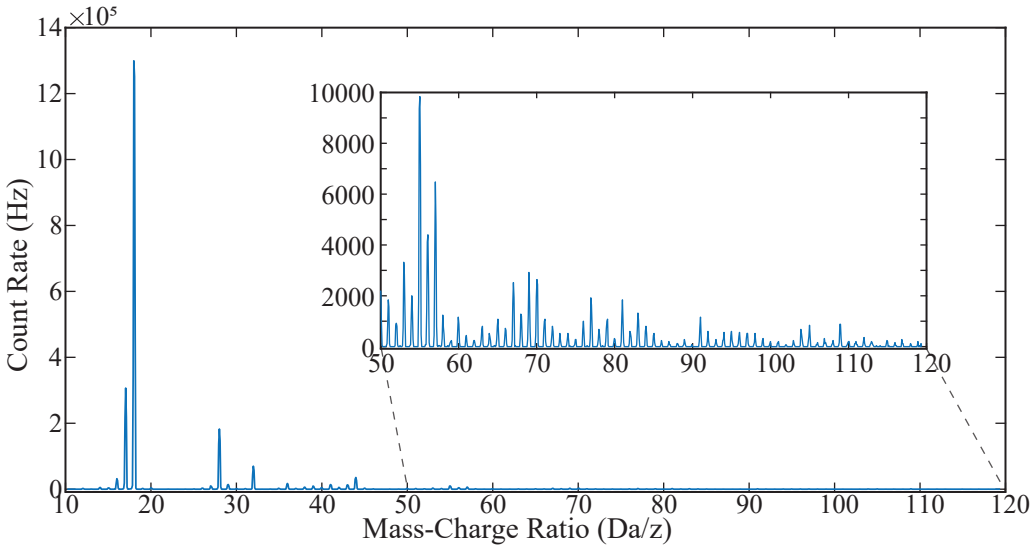


Figure 4.6: Sample mass spectrum of residual gas in the QMF vacuum chamber. This spectrum spans 10-120 Da/z, with average observed peak widths ≤0.2 Da/z. The inset expands on the lower amplitude, higher mass peaks. Amplitudes here are reported in ions/second (Hz) observed on the CEM detector.

directly to the QMF vacuum chamber (seen atop the QMF chamber in fig. 4.2). The volume behind the valve inlet flange is evacuated to ∼15 mtorr with a dry scroll pump, and this volume branches into two regions for liquid and solid samples, respectively (see fig. 4.7). Each sample region is isolated from the volume behind the leak valve by stainless steal ball valves. These volumes are all evacuated sequentially to ∼15 mtorr prior to sample injection by pumping on the desired volume while the others are isolated by their respective ball valves. Once all volumes are evacuated to base pressure, the scroll pump is isolated from the entire manifold by closing a ball valve near the pump inlet flange.

In order to load liquid molecules, the valve to the solid sample arm is closed to isolate it from the system, while the valve for the liquid arm is opened. The liquid sample portion comprises a U-shaped copper tube, sealed at the end by a pierceable rubber septum mounted to a KF40 flange. Molecules are injected through the septum via a syringe, which maintains an air tight seal around the syringe needle during and after

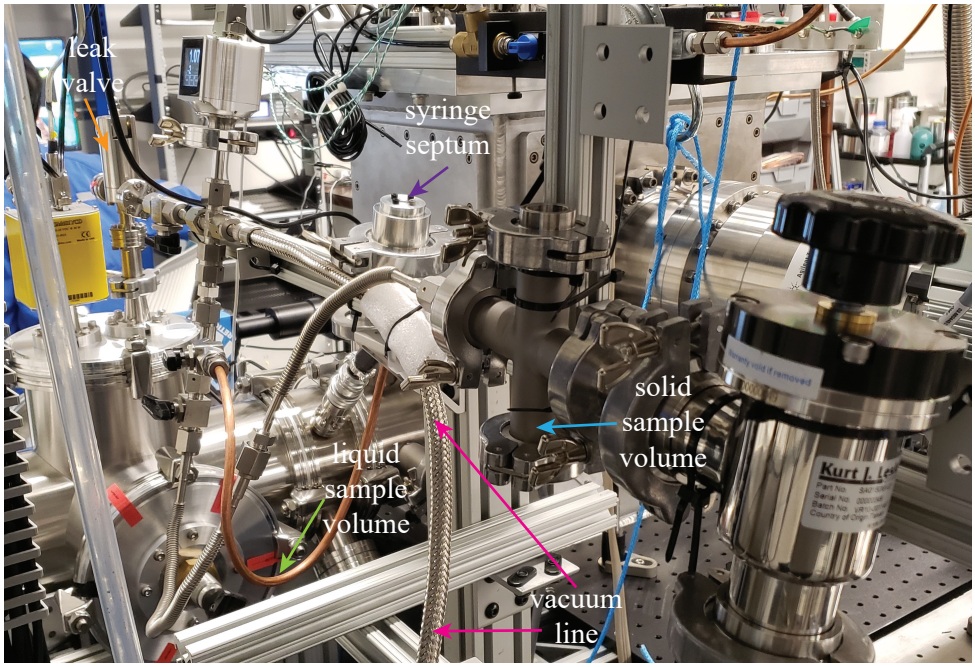


Figure 4.7: The sample input manifold which delivers molecules to the QMF ionizer. Solid samples are placed in the labelled KF25 cross, and molecular vapor diffuses through the flexible metal bellows to the fore volume of the leak valve. Liquid samples are injected through the labelled septum via a syringe and pool in the labelled liquid sample volume. Molecular vapor from either arm diffuses upward to the leak valve fore volume.

injection. The liquid sample pools at the bottom of the copper U-tube, and gaseous vapor from this liquid rises to the leak valve inlet. The sample pressure behind the leak valve is simply the vapor pressure of the given molecular species, typically a few torr for the volatile organic molecules studied here. The leak valve is then opened until a steady pressure of $\sim 10^{-6}$ torr is maintained in the QMF chamber, which corresponds to an ion flux of $\sim 10^{5}$ ions per second exiting the filter. In order to load solid samples, the liquid arm is isolated from the system by closing its ball valve, while the solid arm is exposed to the leak valve. A small amount of solid sample is placed in this volume prior to evacuating it to 15 mtorr, which removes most of the air from the system. Once the scroll pump ceases to pump on the KF25 cross, this volume is filled with vapor from the sample. Again this molecular vapor is slowly leaked into the QMF chamber through the

leak valve, until a steady pressure of $\sim 10^{-6}$ torr is observed in the chamber. The vapor pressures of solids are generally much lower than for volatile liquid molecules, of order 1 mtorr compared to 1 torr. This vapor pressure is still much higher than the desired microtorr-level sample pressure in the QMF chamber, however, and therefore yields a sufficiently high ion flux to facilitate ion loading.

Regardless of the phase of the precursor, some small fraction of these molecules pass through the EI ionizer before being pumped from the chamber or adsorbed to the chamber walls. Collisions with high energy (70 eV) electrons within this region result in ionization. The entire EI region itself is held at a DC potential of +18 V relative to the grounded vacuum chamber. The ions formed in this region thus acquire this energy difference relative to ground as kinetic energy. Within the quadrupole they are accelerated and decelerated to different energies as required for efficient mass filtering. Because of the conservative nature of the electromagnetic force, however, once an ion leaves the QMF its energy relative to the grounded vacuum chamber will revert back to its initial kinetic energy of 18 eV. Since neutral molecules are leaked into the QMF chamber continuously, this entire process produces a continuous stream of 18 eV molecular ions directed toward the ion trap with a flux of $\sim 10^5$ ions per second. It is necessary to apply a gate to this flow of ions, however, in order to avoid overwhelming the trap and loading too many molecules. The final QMF electrode through which ions pass is normally held at $-10$ V in order to focus the outgoing ion beam. When loading molecular ions, this electrode is instead held at +50 V, blocking all ions from exiting the QMF. A fast (40 ns rise time) high voltage switch (Stahl Electronics HS-200) is connected to this electrode, and switches its potential from +50 V to $-10$ V when triggered with a TTL pulse. The flow of ions out of the QMF can therefore be rapidly switched on and off, enabling molecular ions to be loaded in small bursts rather than continuously.

The primary atomic species trapped in this work is $^{88}Sr^+$, which, as mentioned in sec.

4.3, was previously loaded by direct laser ablation into the ion trap. Current experiments instead ablate a solid Sr target (80%Al–20%Sr alloy) which is positioned immediately behind the electron-impact ionizer of the QMF unit. As can be seen in fig. 4.5, there are small (6 mm ∅) through holes in the center of each EI system electrode, providing a direct line of sight through the ionizer along its axis. The output of a pulsed, frequency-doubled Nd-YAG laser (532 nm, 1 mJ per pulse) is aligned through these apertures to ablate the Al-Sr target behind the ionizer. An electrically grounded metal plate with a small (6 mm ∅) aperture lies between the Sr target and the entrance to the ionizer to block most of the ablation plume from reaching and depositing onto the QMF ionizer optics. The fraction of the ablation plume which passes this screen then eneteres the EI volume and is guided into the quadrupole just as molecular ions are. The QMF is tuned to maximize throughput and signal for ions produced at the 18 V EI potential. Ablated $Sr^+$ ions are not created with the same initial energy as gas phase ions, but they are transferred with high efficiency through the QMF, indicating that they should have a kinetic energy comparable to 18 eV. Additionally, since the ablation process itself is pulsed rather than continuous, the voltage switching process used to gate the flow of molecular ions is not needed here. The final focusing element of the QMF is simply held at its normal −10 V potential to guide the outgoing pulse of $^{88}Sr^+$ ions. Additionally, a three electrode electrostatic Einzel lens is attached to the side of the ion trap mounts (seen in fig. 4.4) in order to help focus incoming ions from the QMF into the trap center. In practice, however, this lens is observed to have little effect on loading efficiency. These electrodes are instead held at ground and are therefore not seen by ions from the QMF.

While their respective methods of ionization are different, both atomic and molecular ions are injected into the ion trap via the same mechanism. UHP Ne buffer gas is cooled through the cryogenic heat exchanger described in sec. 4.2.2, and pulsed into the trapping region during ion loading. The timing of this pulse is such that each pulse of

ions entering the trap arrives some milliseconds before the buffer gas pulse ceases. This ensures that the ions arrive in the trapping region at the point of near-peak buffer gas density, increasing the collision rate and therefore the loading efficiency. The ion trap endcaps are held at +15 V when loading, so that the pulse of 18 eV ions is energetic enough to overcome the endcap potential barrier and enter the trapping region. Elastic collisions with Ne buffer gas atoms within this region subsequently reduce the ions' kinetic energy, and after enough such collisions their mean energy is reduced below that of the endcap confining potential. The ions were therefore energetic enough to pass the potential barrier posed by the first endcap, but the buffer gas dissipates enough energy that they cannot pass over the barrier of either end cap again, leaving them confined.

It should be noted that the efficiency of transferring ions across this entire system and into the ion trap center is inherently very low. During the loading process, of order $10^5$ ions per second are created and sent towards the trap center. The voltages applied to the various electrodes used for steering and focusing of the ion beam are crudely optimized to increase the total flux of ions which pass through the aperture through the nearest trap endcap. No rigorous ion tracing simulation or electric field calculation was performed for this optimization, however. As a result, the vast majority of ions produced by this system are lost in transit to the trap. Such inefficiency is beneficial in this experiment, however, since only a single atomic and molecular ion are needed for spectroscopy. Thus while the transfer efficiency of this system is low with respect to how many generated ions are lost, the true loading efficiency for the experiment is very high. Approximately 25-50% of attempts to load a single $^{88}Sr^+$ ion are successful, as are over 50% of attempts to load a single molecular ion. If the efficiency were significantly higher than this, then more than one ion would be loaded with potentially high frequency. Each time this occurs the excess ions must be ejected from the trap and the process repeated. Thus, the relatively un-rigorous fashion in which this system was designed ultimately benefits

the SMTS duty cycle.

It should also be noted that collision-induced dissociation is often observed during ion loading. Since ions are injected into the trap with an approximate kinetic energy of 18 eV, collisions between molecules and Ne atoms in the center of mass reference frame can be highly energetic (>1 eV). Collisions with sufficient energy to dissociate the incoming molecules are therefore not rare. If dissociation does occur, and if the resulting ion fragments fall within the trap stability range, they can remain confined. As a result, whenever a molecular ion is loaded into the ion trap its mass must be verified (see sec. 4.6) to determine whether or not it is the desired analyte or a molecular fragment.

### 4.3.4 Secular Frequency Stability

This QMF loading scheme was developed in order to better control the species of ions loaded into the ion trap, as well as to address the previously mentioned issues of stray charge build up and secular frequency drift. The QMF loading scheme should significantly reduce the effects of the two primary ablation charging mechanisms. The Sr–Al alloy ablation target, which previously was positioned just centimeters from the ion trap for ablation loading, is nearly a meter away from the trap center in the QMF setup. Furthermore, there is no direct line of site between the ablation spot on this target and the trap, thus completely eliminating the deposition of neutral Sr from the ablation plume onto the surfaces of the trap.

Additionally, the flux of $^{88}Sr^{+}$ ions to which the trap is exposed is significantly reduced. Of order $10^2$ $^{88}Sr^{+}$ ions exit the mass filter after each ablation event, compared to order $10^8$ ions of all species which are produced in the ablation plume. Furthermore, the primary surface exposed to this flux of ions for QMF loading is the outer face of the trap PCB which lies between the mass filter and the trap center (see fig. 4.9). This is to say,

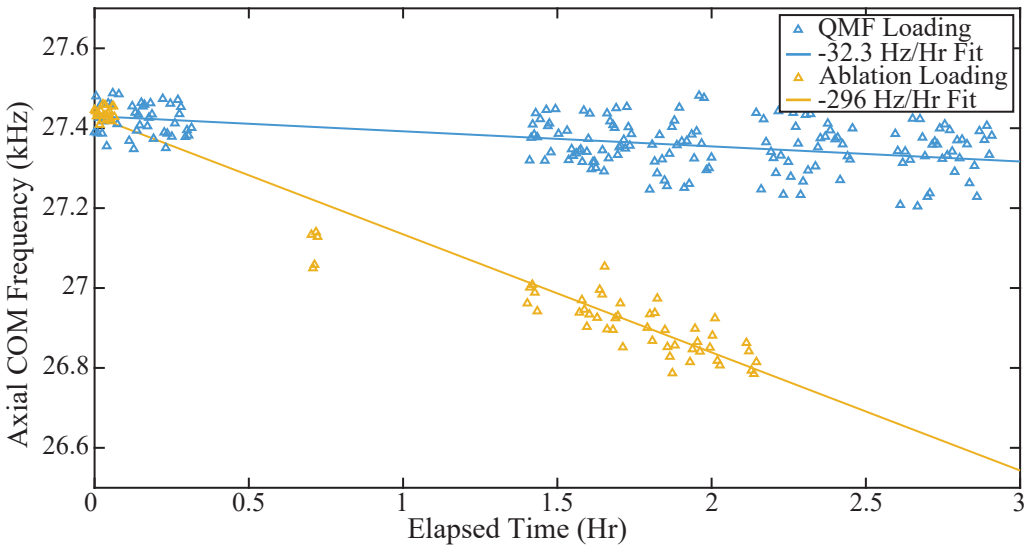


Figure 4.8: The axial secular frequency for $^{88}Sr^{+}$ ions over time. Yellow data points correspond to ions loaded via laser ablation near the ion trap, and blue data points are ions loaded via the QMF. QMF loading reduces the observed secular frequency drift over time by nearly an order of magnitude.

the primary surface onto which ions can be deposited in the QMF scheme is external to the trap center. This is in stark contrast to the ablation setup, in which ions and neutral Sr are free to deposit on the inner faces of the trap PCBs as well as on the quadrupole electrodes. The QMF scheme not only significantly reduces the ion flux which reaches the trap, but nearly all remaining ion deposition onto the trap occurs far from the trap center. The QMF setup therefore effectively eliminates photoelectric charging near the trap center, and the rate of ion deposition into ices near the trap center is dramatically reduced.

Fig. 4.8 captures the effects of these changes. Here the observed axial secular frequency of trapped $^{88}Sr^{+}$ ions is plotted over several hours for both ablation and QMF loading. As can be seen from the linear fit to both data sets, the drift rate of the axial secular frequency for QMF loading is nearly an order of magnitude lower than for direct ablation loading. The reduction in stray charge buildup near the trap center therefore significantly increases the long term stability of the axial secular frequency, which is

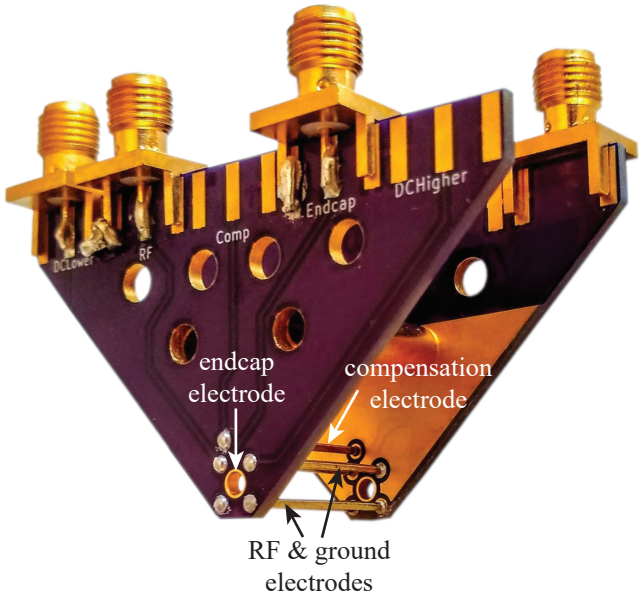


Figure 4.9: The quadrupole ion trap used in this work. The quadrupole electrodes are soldered between two PCBs, and endcaps are formed by gold coated copper traces on the circuit boards. Apertures at the center of the endcap electrodes allow for optical access and ion loading along the trap axis. A fifth electrode above the quadrupole configuration is biased to compensate for stray electric fields which displace ions from the RF null.

crucial for the mass measurement process described in sec. 4.6.

## 4.4 Quadrupole Ion Trap

A custom linear quadrupole trap was constructed for this project, and can be seen in fig. 4.9. The trap comprises a pair of printed circuit boards (PCBs) with brass electrodes of length $\ell = 16.7$ mm and diameter $d = 0.8$ mm soldered between the two in a quadrupole configuration. The diagonal separation between opposing pairs of quadrupole electrodes (inscribed diameter) is 4.4 mm. One opposing pair of these electrodes is held at electrical ground, while the other pair carries a RF sinusoidal voltage. As discussed in ch. 2, this provides a pseudo-harmonic potential which acts to confine ions in the radial direction, orthogonal to the symmetry axis of the trap.

The circuit boards of the trap are mechanically anchored to a pair of brass spacers between these boards, which are equal in length to the quadrupole electrodes, to prevent bending and torsional stress on the electrodes. Each board is mechanically anchored to a rigid, Γ-shaped copper mount (see fig. 4.2), and these mounts are directly anchored to the inner cryogenic radiation shield. Experiments were performed with a copper spacer between the electrodes, rather than brass, which was large enough to accomodate a diode thermometer. This spacer is in intimate thermal contact with the center of the trap circuit boards, but does not contact the copper mounts, thus providing a measure of the circuit board and quadrupole temperatures. During normal operation, when RF voltage is applied to the trap, this temperature is observed to be approximately 7 K. All surfaces in close proximity to the trap center are therefore held between 5.7-7 K.

The RF trapping voltage is provided by a waveform generator and a home-built toroidal resonator. The resonator consists of a 5 cm diameter ferrite torroidal core, with 1 turn of enameled magnet wire on the input and 20 turns on the output. The loaded Q-factor of the resonator is ∼12, and the observed voltage gain is ∼4, with a resonance frequency of 1.63 MHz. This resonator is driven by a sinusoidal voltage at the resonance frequency produced by a programmable waveform generator. The amplitude of the trapping voltage is adjusted by varying the waveform generator output amplitude. The typical trapping voltage for the experiments reported here was 16 $V_{pp}$ into the resonator, corresponding to ∼50 V on the resonator output. This voltage amplitude delivered to the trap was determined by measuring the axial and radial secular frequencies of trapped $^{88}Sr^{+}$ ions and solving eq.s 2.16 and 2.23 for $V_0$.

Electrical connections are made to the circuit boards through SMA connections. Coaxial cables carry both RF and DC voltages from electrical feedthroughs in the vacuum chamber to SMA bulkhead connectors anchored to the outer stage of the cryogenic radiation shield. A second set of coaxial cables transfers these voltages to SMA bulkhead

connectors anchored to the inner stage of the cryogenic radiation shield, and a third set carries these voltages to the trap itself. SMA-type coaxial cables are ideally suited for this purpose, as they shield the RF drive signal from external noise while preventing the DC signals from picking up 1.63 MHz RF noise. Additionally, the polymer insulating layer and stainless steel ground sheath of these cables makes them relatively poor thermal conductors. This allows voltages to be transferred across the radiation shields with the cables anchored directly to the shields through bulkhead connectors. Such connectors maintain a relatively hermetic seal while reducing the thermal conductance between the chambers across these connections, as compared to simple copper wires which would conduct much more heat between the shields and affect their operating temperatures.

Confinement along the axis of the trap is achieved with two endcap electrodes, shown in fig. 4.9. Two through holes 3.9 mm in diameter are drilled through the PCBs. These apertures are centered along the trap axis to provide optical acess as well as an open path along which ions can travel from outside the trap to the trap center during ion loading. A gold-plated copper solder pad slightly larger in diameter than the axial apertures surrounds the perimeter of each aperture. These metal traces constitute the endcap electrodes, and DC voltages are applied to these electrodes for axial ion confinement. The two endcaps are electrically isolated from one another, so that their voltages may be adjusted independently to shift the position of the trap center along the quadrupole axis. The endcaps typically carry +15 V each during ion loading, and +40 V during the other stages of the experiment. For the operating conditions described, with $\Omega_{RF} = 2\pi \times 1.63$ MHz, $V_0 \approx 50$ V, and $V_{DC} = 40$ V, the observed axial and radial secular frequencies for $^{88}Sr^{+}$ are $\sim$28 kHz and $\sim$196 kHz, respectively.

### 4.4.1 Stray Field Compensation

The presence of any stray, uncontrolled electric fields which originate outside of the trap but which permeate the trap center is extremely deleterious to the performance of the trap and the stability of trapped ions. If such a stray field is sufficiently large, it will influence the ions in the trap and act to displace them from the RF null point. Recall that the amplitude of ion micro-motion (given by eq. 2.12) is linearly proportional to the instantaneous displacement of the ions from the RF null point (see fig. 2.3). The micromotion amplitude of an ion which is persistently displaced from the RF null by stray electric fields is therefore non-zero and increases with displacement. An increase in micromotion amplitude is equivalent to an increase in the ion's translational temperature, leading to the undesirable effect of "RF heating."

Such external fields may be counteracted by generating controlled electric fields which displace trapped ions in the opposite direction, thus returning them to the trap center. This is accomplished in the $x-$ and $y-$directions simultaneously by applying a small DC potential to one of the two ground electrodes in the quadrupole configuration.[4] Additional compensation primarily along the $y-$axis is achieved by a fifth electrode (denoted "compensation electrode" in fig. 4.9), which is positioned 3.8 mm above the trap axis and slightly off center from the quadrupole configuration. Compensation voltages ranging from 0-3 V are typically applied to these electrodes to reduce ion micromotion.

## 4.5 Laser Optics

As discussed in sec. 2.2.2, two different wavelengths of light are required for laser cooling of $^{88}Sr^{+}$: the first drives the primary cooling transition at 422 nm, and the

[4] If instead one wished to modify the Mathieu $a$ stability parameter, a DC potential would have to be applied to both ground electrodes simultaneously.

second "repump" laser at 1092 nm prevents optical pumping into the metastable $4^2D_{3/2}$ state. An additional coherent, mid-IR light source is needed for vibrational spectroscopy, for a total of three independent sources.

### 4.5.1 Laser Cooling Sources

#### 422 nm Light Source

Cooling light at 422 nm is provided by an external cavity diode laser (ECDL, MOGLabs LDL), which produces approximately 25 mW of light near the diode. The frequency of the ECDL is coarsely tuned by adjusting the drive current and temperature of the diode, and finely tuned by adjusting the grating angle of the external cavity. The mode-hop free tuning range of this system is several GHz, while the spectral width of the output is of order 100 kHz, much narrower than the 20.05 MHz natural linewidth of the cooling transition. The output of the ECDL passes through a Faraday isolator to protect the diode from back reflections, and subsequently split into an experiment and reference beam. The experiment beam passes through an acousto-optical modulator (AOM) in the double pass configuration, which provides a net frequency shift to the beam of +520 MHz relative to the ECDL output. The beam is then coupled into an optical fiber which transfers it to an optical breadboard near the vacuum chamber. The optical path of this beam, along with the other two light sources, is shown in fig. 4.10. For simplicity, the referenced fiber optics are not shown.

As the name implies, the reference beam is separated from the ECDL output and used to measure the current lasing frequency of the system. By fortunate coincidence, the $5^2\mathrm{S}_{1/2}(F=2) \rightarrow 6^2\mathrm{P}_{1/2}(F'=2,3)$ hyperfine transition frequencies in $^{85}$Rb are very nearly equal to the primary $^{88}\mathrm{Sr}^+$ laser cooling frequency [108], laying $-440$ and $-560$ MHz, respectively, below the laser cooling transition. A simple, commercially available

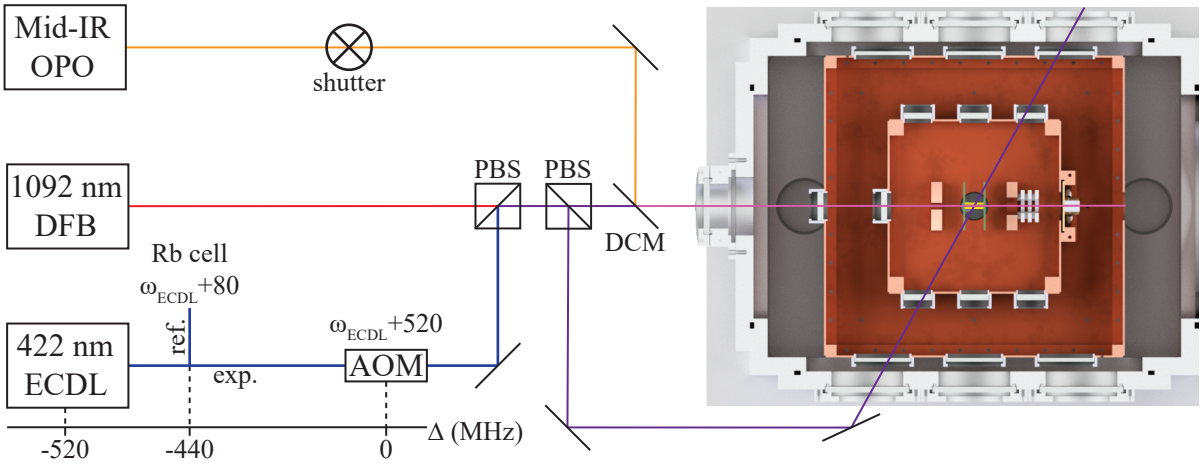


Figure 4.10: A simplified schematic showing the beam paths of the three laser light sources used in this work. The axis shown below the 422 nm ECDL indicates the detuning ($\Delta$) of the ECDL, reference beam, and experiment beam, all relative to the $^{88}Sr^{+}$ laser cooling frequency. When the ECDL is tuned to bring the refernce beam on resonance with the $^{85}$Rb $5^2S_{1/2}(F=2) \rightarrow 6^2P_{1/2}(F'=3)$ transition, the experiment beam is resonant with the $^{88}Sr^{+}$ cooling transition.

Rb vapor cell is therefore used for frequency reference. The reference beam passes through a separate AOM, which provides a net frequency shift to this beam of +80 MHz relative to the ECDL output. The beam is then directed through the Rb vapor cell, where standard saturated absorption spectroscopy provides an absorption measurement of the $5^2S_{1/2}(F=2) \rightarrow 6^2P_{1/2}(F'=2,3)$ hyperfine transitions, as well as an artificial crossover peak which lies halfway between the two. The combined effect of both AOMs shifts the experiment beam +440 MHz above the reference beam. As a result, if the ECDL is tuned such that the reference beam is resonant with the $^{85}$Rb $F=2 \rightarrow F'=3$ transition, the experiment beam will be exactly resonant with the $^{88}Sr^{+}$ cooling transition. As indicated in sec. 2.2, however, the laser cooling process requires a slight red-detuning of the cooling beam from resonance. In practice, the ECDL frequency is maintained slightly below ($\sim$20 MHz) the artificial crossover peak, the center of which is $-60$ MHz from the $^{85}$Rb $F=2 \rightarrow F'=3$ transition, and $-500$ MHz from the $^{88}Sr^{+}$ cooling

transition. This corresponds to a net ECDL red-detuning of ∼80 MHz. The experiment beam frequency is finally fine tuned to optimize the fluorescence intensity from trapped $^{88}Sr^{+}$, thus optimizing the laser cooling efficiency, either by making small adjustments to the ECDL frequency or by tuning the experiment beam AOM drive frequency. The total experiment beam power just before the second PBS in fig. 4.10 is approximately 800 $\mu$W.

### 1092 Light Source

Repump light at 1092 nm is provided by a distributed feedback (DFB) single frequency diode laser (Photodigm PH1092DBR080T8). The output of this diode is single mode, with a spectral width of order 1 MHz, comparable to the natural linewidth of the $4^2D_{3/2} \rightarrow 5^2P_{3/2}$ repump transition. The laser output passes through a Faraday isolator, with approximately 10 mW of light exiting the isolator, before passing through a cylindrical lens to compensate for the elliptical mode shape naturally produced by the diode. The total power of this repump beam just before the second PBS in fig. 4.10 is approximately 1.5 mW. The laser frequency is coarsely adjusted by varying the temperature of the diode in millikelvin increments. A portion of the DFB diode output is sampled from the beam, fiber coupled, and sent to a wavelength meter for frequency monitoring. The meter has 50 MHz resolution, and in practice the DFB diode is not locked to any frequency reference, as the observed time scale for frequency drifts is <50 MHz over the course of several hours. In practice it is observed that repump laser detunings >50 MHz are still sufficient to produce detectable ion fluorescence, implying that the intensity of the repump laser seen by trapped $^{88}Sr^{+}$ ions is well above the saturation intensity for the $4^2D_{3/2} \rightarrow 5^2P_{3/2}$ transition. From the equation for $I_{sat}$ defined with eq. 2.27, the repump transition saturation intensity is ∼0.15 mW/cm$^2$. The diameter of the combined cooling beams in the trap center is ∼1 mm with a power of ∼1 mW in the axial direction ($I \approx 127$

mW/cm$^2$). This leads to an approximate power broadening of $\Delta\nu = \frac{\Gamma}{2\pi}\sqrt{1+\frac{I}{I_{sat}}} \approx 43$ MHz [22], consistent with the above detuning observations. The frequency of the laser is tuned in increments of ∼10 MHz by tuning the diode temperature to maximize the $^{88}Sr^+$ ion fluorescence intensity, thus maximizing the laser cooling efficiency.

Each cooling beam is fiber coupled near the respective lasers and transferred to the optical breadboard nearest the inlet window of the vacuum chamber (again, these are not shown in fig. 4.10). The two beams are combined into one using a polarizing beamsplitter cube, and the combined beam is subsequently split into two. One of these beams is aligned through the ion trap directly along the trap axis, cooling ions along this axial direction. The second beam is aligned into the vacuum chamber and through the ion trap center at an approximately 60°angle to the trap axis (purple lines in fig. 4.1) to cool ions in the radial direction. The power ratio between these two beams varies from experiment to experiment, but on the average approximately 60% of the combined beam power is directed axially, with the remainder split into the radial beam.

### Beam Geometry

As is shown in fig. 4.10, the combined cooling beams propagate both along, and at a ∼60°angle to, the trap axis. It is important to note that neither of these beams is retro-reflected, as is commonly done in laser cooling experiments. Suppose the 422 nm component of the combined cooling beams is tuned slightly below the cooling transition. A $^{88}Sr^+$ ion moving anti-parallel to the incident beam would see a relative blue-shift of this beam onto resonance with the cooling cycle, leading to a high photon scattering rate. If the ion instead moved parallel to the incident beam, this beam would be red-shifted further from resonance, and the photon scattering rate would decrease. If the cooling beams are retro-reflected, however, then motion of the ion parallel to the incident beam is also anti-parallel to the retro-reflected beam. Thus, while the incident cooling beam

is red-shifted off resonance in this case, the retro-reflected cooling beam is blue-shifted onto resonance, and the photon scattering rate remains high.

A retro-reflected cooling beam geometry therefore maintains a nearly constant photon scattering rate for trapped ions, regardless of their direction of oscillation. This is desirable in conventional laser cooling experiments, since a high photon scattering rate corresponds to a high laser cooling efficiency. In a non-retro-reflect beam geometry, oscillation of the ions will lead to variations in the photon scattering rate with the same period as the oscillation. As will be seen in sec. 4.6, this is extremely advantageous for the SMTS method. Cooling laser light in fig. 4.10 is therefore intentionally non-retro-reflected through the trap.

### 4.5.2 Mid-IR Light Source

Recall from sec. 3.1.4 that vibrational bands typically fall into two major spectral regions, the fingerprint and functional group regions, corresponding to qualitatively different classes of vibrational motion. As previously noted, the primary aim of this work is molecular identification, rather than high resolution structure analysis. The fingerprint region is therefore the natural region of the vibrational spectrum to investigate here. Mid-IR light which is coherent, collimated, broadly tunable, and high power is relatively challenging to generate in this frequency range, however. Experiments which work in this range often rely on custom light sources, which increases experimental complexity, and relatively few commercial systems are available which provide all of these desired features. Multiple commercial systems are available in the functional group range, however, which are simple to use turn-key devices. Additionally, the functional group region is typically much more sparsely populated than the fingerprint region, thus reducing the complexity of resulting data. This is advantageous for the type of proof-of-concept

measurements reported here, thus the functional group region was chosen as the subject for this work. While definitive molecular identification is less straightforward for such spectra, the results of these measurements are more than sufficient to demonstrate the capabilities of the novel SMTS protocol, which can be easily adapted to the fingerprint region with a different mid-IR light source.

Broadly tunable mid-IR light is provided by a pulsed optical parametric oscillator (OPO). This is a commercial, tabletop, turn-key system (M Squared Lasers, Firefly IR) which produces >50 mW average power across a frequency range of 2700–4000 $cm^{-1}$. This pulsed source operates at a repetition rate of 150 kHz and <10 ns pulse duration, with spectral width ∼6 $cm^{-1}$ in the frequency range of interest in this work. In order to prevent saturation of molecular vibrational transitions during spectroscopy, the OPO output is attenuated by approximately 1/2 using a neutral density filter of density 0.3 near the OPO module. This mid-IR light is co-aligned with the two laser cooling beams through a dichroic mirror near the vacuum chamber, and the three combined beams all propagate along the axis of the ion trap, passing through the trap endcaps. The mid-IR beam is well collimated and has a waist of approximately 2 mm near the OPO head. In order to prevent clipping on the trap endcap aperture, the beam passes through a weakly focusing lens upstream of the dichroic mirror, resulting in an approximate beam waist at the trap center of ∼1 mm.

The frequency range of this system spans the C–H (∼3000–3100 $cm^{-1}$) and N–H (∼3300–3400 $cm^{-1}$) stretching regions. The OPO is calibrated against a separate species for each of these regions. The lower frequency C–H stretching range is calibrated against a thin polystyrene film, which exhibits five well defined, NIST-traceable bands in the region from 2850–3100 $cm^{-1}$. The higher frequency N–H stretching range is calibrated against an ammonia vapor cell, where ammonia exhibits ∼16 ro-vibrational transitions between 3150–3500 $cm^{-1}$ which are resolvable with this light source. The offset between

the internally programmed and calibrated OPO frequencies is linear, and a simple linear calibration curve is applied to the frequency axis of experimentally observed spectra.

Prior to reaching the dichroic mirror which combines the three experimental beams, the mid-IR beam passes through a fast mechanical shutter (labelled in fig. 4.10). The shutter comprises a small plastic wiper held at a right angle to the axle of a stepper motor. The motor is driven by a programmable microcontroller which is triggered by a TTL pulse. A rotation of the motor axle by some small fraction of a revolution translates the tip of the wiper up and down. The shutter is held normally closed, with the wiper up and blocking the OPO beam, so that trapped ions are not continuously irradiated by mid-IR light. This is necessary, for example, during molecular tagging. The microcontroller rotates the motor to "open" the shutter and pass the beam for a period equal to the length of the TTL trigger pulse, with a minimum open period of 65 ms and a maximum of 16 s. Although the OPO is pulsed, it is treated as quasi-continuous during these shutter opening periods. The full rationale for the use of a normally closed shutter on the OPO beam is explained in sec. 4.7.

## 4.6 Non-destructive Mass Spectrometry

The ability to non-destructively determine the mass of a trapped molecular ion is central to the SMTS technique. Non-destructive mass spectrometry is indeed the entire motivation for developing the previously described infrastructure for co-trapping laser cooled atomic ions along with molecular analyte ions. The harmonic confining potential of the quadrupole trap is exploited here to perform non-destructive mass measurements on trapped ions via two novel and complementary techniques.

### 4.6.1 Chirped Tickle Scan

The so-called "tickle" method of measuring the secular frequencies of trapped ions has been adopted as a common and powerful tool for experiments with trapped ions [109, 110, 111]. The technique has been implemented with a number of different experimental variations, but at its core the tickle method exploits the mass dependence of the secular frequency of an ensemble of trapped ions highlighted in sec. 2.1.2. A novel version of the tickle method was developed in this work which relies on the relationship between the axial secular frequency of trapped $^{88}Sr^{+}$ and the axial secular frequency of a two ion $^{88}Sr^{+}$–molecule Coulomb crystal, as articulated in eq. 2.24.

This measurement scheme is implemented as follows. A single $^{88}Sr^{+}$ ion is first trapped and laser cooled. A RF bias tee connected to a trap endcap electrode enables a low frequency sinusoidal voltage to be coupled to the endcap while maintaining the high DC voltage needed to confine ions. A small amplitude ($\sim$5 mV) chirped voltage pulse (see fig. 4.11*a*) is applied to an endcap through this tee. This is a cosine waveform whose frequency increases linearly over time for the duration of the pulse, exposing the ion to each frequency in the scanned range in equal measure.[5] For the majority of its duration, this pulse has little effect on the ion; the amplitude of the voltage is only $\sim$1% that of the DC endcap voltage, and thus minimally perturbs the ion's position. Once the chirp frequency sweeps over the axial secular frequency, however, the ion will undergo resonant, large amplitude oscillation at $\omega_{z,Sr}$.

Recall from sec. 4.5.1 that the cooling laser geometry in this experiment is not retro-reflected. The $^{88}Sr^{+}$ ion is nearly stationary near the turning points of its driven secular oscillation, and thus sees no Doppler shift of the cooling laser frequency, while its velocity is greatest as it passes through its equilibrium position at the trap center. From the ion's

[5] In frequency space the chirp constitutes a square pulse.

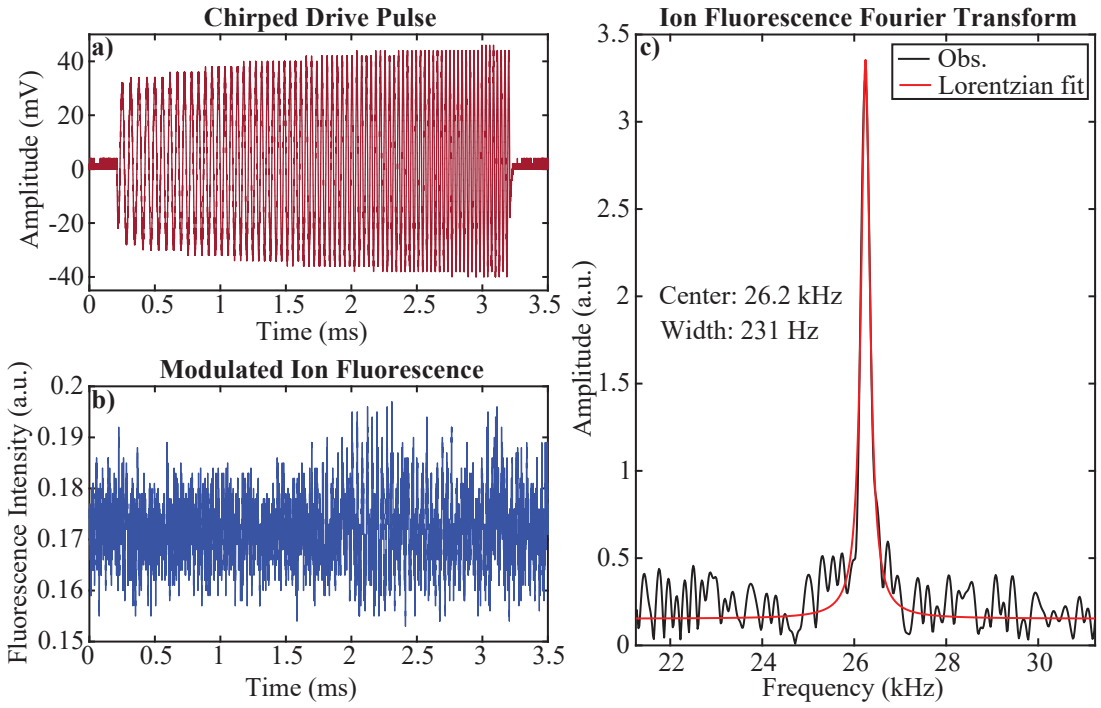


Figure 4.11: *a)* The chirped voltage pulse applied to trapped ions. The programmed pulse amplitude is typically ∼80-100 $mV_{pp}$, but this is attenuated to ∼10 $mV_{pp}$ before reaching the trap. *b)* The $^{88}Sr^{+}$ fluorescence signal observed by the PMT. Modulation of the signal begins when the chirped pulse passes over the Coulomb crystal's secular frequency near $t = 2$ ms, and is gradually damped due to laser cooling. *c)* The Fourier transform of the modulated fluorescence signal in *b* reveals the frequency of induced secular motion.

perspective, a large Doppler shift of the cooling laser frequency occurs and the two are detuned from resonance, leading to a reduction in the photon scattering rate and therefore a decrease in the fluorescence intensity. The period for this variation in the fluorescence intensity is simply the period of oscillation, thus the $^{88}Sr^{+}$ fluorescence intensity during this process is modulated at the axial secular frequency $\omega_{z,Sr}$. A custom, long working distance objective 50 mm in diameter is positioned approximately 8 cm directly below the center of the ion trap and collects 422 nm fluorescence light from the laser cooled $^{88}Sr^{+}$ ion. The trap center is then imaged onto a beam splitter cube, which passes 30% of the light to a CCD camera where the ions can be observed directly, while the remaining 70% goes to a photomultiplier tube (PMT). The amplitude of the PMT output signal

is proportional to the observed ion fluorescence intensity, so that the PMT signal is modulated at the same frequency as the ion fluorescence (fig. 4.11*b*). This signal is then directly Fourier transformed to determine the oscillation frequency (fig. 4.11*c*).

The $^{88}Sr^{+}$ ion may be viewed as a damped oscillator during this process, where the effect of laser cooling may be viewed in the equation of motion as a simple damping coefficient. The ions begin to oscillate once the chirp passes over the axial secular frequency, but the chirp quickly sweeps past this frequency and no longer interacts with the ions. The result is that the ion motion decays over time, producing the damped oscillation (or "ringdown") seen in the PMT signal in fig. 4.11*b*. The greater the laser cooling efficiency during this ringdown process, therefore, the larger the effective damping coefficient and the faster the decay. When Fourier transformed into frequency space, this corresponds to a greater peak width. In order to achieve narrow Fourier linewidths for better frequency resolution in the tickle scan, chirped tickles are typically performed with the laser cooling power slightly below the saturation intensity of the $5^2S_{1/2} \rightarrow 5^2P_{1/2}$ cooling transition ($I_{sat} \approx 35$ mW/cm$^2$, $I/I_{sat} \approx 0.6$). The tickle Fourier linewidth for $I < I_{sat}$ is typically observed to be ∼100-200 Hz, compared to ∼700-1000 Hz in the over-damped, $I > I_{sat}$ case.

In addition to this practical consideration for the laser cooling intensity, the cooling beam is red detuned (typically ∼80 MHz) to maximize the resonance condition when the ions are oscillating quickly, thus increasing the fluorescence and photon collection rate to improve the signal amplitude. The chirped pulse typically sweeps in frequency from 20-30 or 25-35 kHz, and each pulse lasts for a total of 3 ms. Pulses are spaced 2 ms apart in time, to allow the Doppler cooling process to extinguish all ion oscillation before the start of the next chirped pulse. The pulse amplitude is set to ∼80-100 $mV_{pp}$ at the output of the waveform generator which produces the signal, but the pulse amplitude is attenuated down to ∼10 $mV_{pp}$ before reaching the endcap. The PMT signal observed from each

chirp pulse is sent to a high speed digital oscilloscope card (Spectrum Instrumentation M4i, 625 MS/s), and the process is repeated over thousands of cycles for averaging. Approximately 2000 chirped pulses and their corresponding PMT signals are averaged in the digital oscilloscope for a typical tickle scan measurement, and this average signal is Fourier transformed to determine the secular frequency. The elapsed time for a chirped tickle scan of 2000 averages is approximately 30 s.

As can be seen in fig. 4.11*b*, the observed change in $^{88}Sr^{+}$ fluorescence intensity during resonant secular oscillation is ∼7%. It is observed in practice that the displacement of a $^{88}Sr^{+}$ ion during this oscillation is approximately one Coulomb crystal lattice spacing, ∼50 $\mu$m. Given the observed $^{88}Sr^{+}$ axial secular frequency $\omega_z/2\pi = 28$ kHz, this corresponds to an approximate peak ion velocity of 8 m/s. One may apply the photon scattering rate equation (eq. 2.27) with $I/I_{sat} = 0.6$ and $\Delta = 2\pi \times 80$ MHz in the case that the ion is stationary ($v = 0$, $R_0$) and in the case that it is moving along the trap axis at velocity $v \approx 8$ m/s ($R_{sec}$). This yields a relative scattering rate during secular oscillation of $R_{sec}/R_0 \approx 0.92$. This predicted relative shift agrees well with the modulation observed by the PMT, thus validating the estimated ion displacement and velocity.

Once the axial secular frequency of $^{88}Sr^{+}$ has been measured, a molecular ion of interest is loaded and co-trapped with the $^{88}Sr^{+}$ ion, and this process is repeated. When the chirp passes over the axial secular frequency for the two ion crystal COM, both ions will undergo resonant, large amplitude oscillation. Again the $^{88}Sr^{+}$ fluorescence intensity is Doppler modulated at the axial secular frequency, $\omega_{z,Sr-mol.}$, and this frequency is determined by Fourier transforming the modulated PMT fluorescence signal. Finally, these two frequencies are inserted into eq. 2.24, with $\omega_a = \omega_{z,Sr}$ and $\omega_{ab} = \omega_{z,Sr-mol}$, and the equation is solved for the molecular mass, $m_b = m_{mol}$.

### 4.6.2 Lock-In Mass Detection

As noted in sec. 4.3.3, molecular ions can undergo collision-induced fragmentation during the loading process, so that the ion mass for which the QMF is programmed is not always the same mass which appears in the trap after loading. This is among the reasons why the chirped tickle scan method is highly valuable, as it can sweep a wide frequency (and therefore mass) range, so that many possible molecular masses can be polled just after loading to identify the molecule which was trapped.

The flexibility of this method is significantly more than what is fundamentally required by the tagging process, however. It is clear from the essential steps of a tagging spectroscopy measurement that only two masses are relevant: the mass of the molecular ion, and the mass of the molecular ion plus a tag. In principle, only these two masses will exist in the ion trap at any time during the experiment, corresponding to the tagged/ground and un-tagged/excited states of the molecule. At ∼30 s, the chirped tickle scan is a relatively slow measurement and would prove cumbersome to perform after every tagging and de-tagging event. An alternative mass measurement scheme which samples a much smaller range of potential molecular masses could therefore significantly increase the SMTS data acquisition speed. In fact, this is easily implemented following a chirped tickle scan measurement.

As indicated in the preceding section, once a molecular ion is co-trapped with a $^{88}Sr^{+}$ ion, the axial secular frequency $\omega_{z,Sr-mol}$ for the ensemble is measured with a chirped tickle. Once $\omega_{z,Sr-mol}$ is known, a single frequency drive voltage, rather than a frequency swept chirp, can then be applied to the trap at precisely the measured value of $\omega_{z,Sr-mol}$. If the mass of the ensemble remains constant, i.e. $M = m_{Sr} + m_{mol}$, then the ions will continuously resonantly oscillate at $\omega_{z,Sr-mol}$, resulting in a continuous Doppler modulation of the $^{88}Sr^{+}$ fluorescence intensity. If the mass of the ensemble changes at

all, for example due to the addition of a tag on the molecule, then the ions will no longer respond to this continuous drive voltage and the $^{88}Sr^{+}$ fluorescence intensity will be unmodulated (see fig. 4.13*a*). The correlation between the Doppler modulation frequency and the single frequency drive voltage can be readily determined using a lock-in amplifier, which effectively integrates the product of these two sine waves over time. If the two are equal in frequency (i.e. the ions are responding resonantly to the drive) then this integral will be large, and if the two have very different frequencies (i.t. the ions no longer respond to the drive) then this integral will be near zero. Both the drive voltage and the fluorescence signal seen by the PMT are sent to a lock-in amplifier which integrates the two over a 500 ms period. The output of the amplifier is an analog voltage proportional to the integral over time of the product of the signals, high in the case of strong correlation and near zero in the case of low correlation (blue and orange trace is fig. 4.13*b*).

If the drive voltage is resonant with the ion ensemble, then the result of this single frequency measurement is equivalent to that of the chirped tickle scan: both measurements reveal that the mass of the ensemble is $M = m_{Sr} + m_{mol}$. If the drive is not resonant with the ensemble, then this single frequency measurement yields less information than the chirped tickle: it indicates that the mass $M \neq m_{Sr} + m_{mol}$, but it does not reveal the true mass as the chirp does. Although the measurement is less information rich in this case, it is sufficient for the spectroscopic task at hand. As previously noted, the only two masses which naturally occur throughout a de-tagging spectroscopy experiment are $M = m_{Sr} + m_{mol}$ when the molecule is not tagged and $M = m_{Sr} + m_{mol} + m_{\mathrm{N}_2}$ when the molecule is tagged. If the ions are observed to be uncorrelated with the tagged molecule frequency $\omega_{z,Sr-mol+\mathrm{N}_2}$, this is sufficient to determine that the molecule is not tagged, and vice versa. The lock-in amplifier method can therefore distinguish between the tagged and un-tagged states of the molecule on the time scale of the lock-in integration period, since is does not poll many possible frequencies/masses as does the chirped

method. In practice, measurements must be made across a few integration periods in order to distinguish variations in the lock-in correlation signal from natural noise on this signal, resulting in an effective measurement time of ∼2 s, rather than 30 s needed for a chirped measurement. The role of the lock-in measurement in the experimental cycle is described in more detail in the next section.

## 4.7 Experimental Sequence

Each primary component of the apparatus, along with its function within the SMTS process, has been described at various points within this chapter. For the sake of clarity, it is helpful to compile these operations into a single discussion to summarize the full experimental sequence needed to obtain single molecule spectra.

### Ion Loading

As described in sec. 4.3.3, the experiment begins by loading ions into the quadrupole trap. The cryogenic shutter described in sec. 4.1 is first opened to provide a line of sight between the QMF outlet and the trap center. A single $^{88}Sr^{+}$ ion is loaded by mass filtering ablated $Sr^{+}$ ions and injecting these ions into the trap center along with a simultaneous pulse of Ne buffer gas cooled to ∼13.8 K. The trap center is constantly irradiated with the two cooling lasers described in sec. 4.5. When an ion is successfully trapped, the output of the PMT which monitors the trap center discontinuously jumps to a higher value, indicating that a fluorescing ion is confined in the trap. Within a few seconds, after the buffer gas pressure in the chamber has dissipated to near zero, the ion is laser cooled to the Doppler limit and occupies a tightly bound equilibrium position at the trap center. The axial secular frequency for this single ion, $\omega_{z,Sr}$, is then measured via the chirped tickle method of sec. 4.6.

After loading $^{88}Sr^{+}$, molecular vapor (either from a solid or liquid precursor) is leaked into the QMF chamber to produce molecular ions, while the +50 V gate voltage described in sec. 4.3.3 is applied to the output of the QMF to block the flow of ions. Ne buffer gas is again pulsed into the trap center at a temperature of 13.8 K, while a TTL pulse triggers the QMF gate voltage to pass molecular ions to the trap for a brief period of time, typically 500 ms. This trigger is timed such that molecular ions arrive at the trap ∼10 ms before the end of the buffer gas pulse. After several seconds, once the residual buffer gas has been pumped from the system, a visual inspection of the imaging camera indicates whether or not a molecular ion was successfully loaded. It is not uncommon to load more than one molecular ion on a single attempt. If this occurs, the molecular guest ions are ejected by driving radial secular motion at the radial secular frequency corresponding to the molecule's mass. This drive leaves the $^{88}Sr^{+}$ ions confined, and the loading process continues until one molecule has been co-trapped. Once this two ion Coulomb crystal has been generated, the axial secular frequency for the crystal's COM motion (previously $\omega_{z,Sr-mol}$, abbreviated to $\omega_{mol}$ here) is also measured via the chirped tickle scan. These frequencies are entered into eq. 2.24 to confirm that the trapped molecule is of the desired mass. With the requisite two ion crystal loaded, the cryogenic shutter is then closed to isolate the ions from warm background gas in the outer vacuum chamber.

**Tagging**

Once a two ion Coulomb crystal containing the correct molecular ion is trapped, the temperature of the cryogenic heat exchanger is reduced from 13.8 K to 13.2 K for tagging. The ions are continuously driven by a small amplitude voltage at $\omega_{mol}$, as described in

4.6.2. This results in an unresolved image of the ions (4.12 top[6]) and a high lock-in amplifier signal (4.13 trace left). A brief (∼2.5 ms duration) pulse of He–$N_2$ is then injected into the trapping region in an effort to tag the molecular ion. The ions are temporarily heated out of the Coulomb crystal by the high collision rate resulting from this gas pulse, until the residual gas is removed from the chamber. If no tag attaches to the molecular ion then the pair will continue to be resonantly driven by the $\omega_{mol}$ drive voltage, their image will not be resolved, and the lock-in signal will recover and remain high. If the molecular ion does gain a tag, however, then the two-ion COM secular frequency will no longer be resonant with the $\omega_{mol}$ drive voltage. The ions therefore cease to oscillate, and instead are cooled back into an ordered Coulomb crystal (fig. 4.12 bottom). As a result, the lock-in signal does not recover and remains near zero (fig. 4.13 trace right), indicating that the molecular ion has been tagged. The ions are finally briefly driven at $\omega_{mol+N_2}$ to confirm that the tag is indeed $N_2$. It is observed in this apparatus that, in the absence of mid-IR OPO light, molecules tagged with $N_2$ remain tagged for an average of approximately 4-8 hours. This is the time scale on which "background" de-tagging events, likely due to collisions with hot background gas, occur.

The overall tagging efficiency varies by molecule. The described tagging process successfully attaches a tag to the tropylium molecule ($C_7H_7^+$, sec. 5.1) with an approximate average efficiency near 20%, while average tagging efficiencies for fragment ions of 1,3-benzodioxole (sec. 5.2) and indole (sec. 5.3) are 80-90% or higher. As indicated in sec. 3.3, this variability arises from the difference in geometry and charge distribution between each species. In all three species, however, it is regularly observed that an appreciable fraction of successful tagging events result in a $H_2$ tag rather than $N_2$. This is in spite of the fact that nominal $H_2$ contamination in the tagging gas mixture is at the part per

[6]The observed camera images and lock-in amplifier signals are identical for the tagging and de-tagging processes, hence the same image is used to illustrate both schematically here.

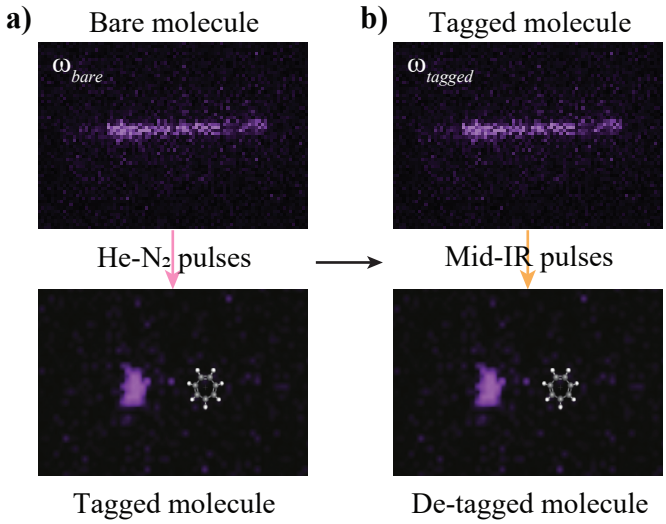


Figure 4.12: *a)* Prior to tagging the ion pair is driven at the ensemble frequency corresponding to the un-tagged molecule, $\omega_{bare}$. He–$N_2$ gas is pulsed into the trap, and the ions stop responding to the drive voltage once the molecule is tagged. *b)* The reverse of the tagging process. The ion pair is driven at the tagged ensemble frequency, $\omega_{tagged}$. The ions are exposed to mid-IR light, and resonant oscillation ceases to occur once the molecule has de-tagged and the secular frequency of the pair has changed.

million level and the partial pressure of residual $H_2$ in the trapping region is estimated $<10^{-9}$ torr. Nevertheless $H_2$ tagging is observed frequently in all three species studied thus far. This is confirmed through the lock-in method by driving the tagged Coulomb crystal at the frequency corresponding to a molecule tagged with $H_2$ and observing an elevated lock-in signal as well as resonant oscillation imaged on the CCD camera. It is further confirmed through slower chirped tickle scan measurements. For each molecular species, the typical lifetime of a $H_2$ tag is observed to be approximately 20-30 minutes, owing to the lower polarizability of $H_2$ compared to $N_2$ ($\alpha_{N_2} \approx 2.2 \times \alpha_{H_2}$ [91, 105]). Observations from traditional tagging experiments have reported typical $H_2$ binding energies of $\sim$500 cm$^{-1}$ $\approx$ 700 K [84], while DFT calculations performed in this work indicate that this energy is closer to $\sim$200 cm$^{-1}$ $\approx$ 300 K. In contrast, such calculations find typical $N_2$ binding energies closer to 1000 cm$^{-1}$ $\approx$ 1500 K.

This relatively weak $H_2$ binding energy can also be exploited to increase tagging

efficiency. Tagging with multiple $H_2$ tags or a combination of $H_2$ and $N_2$ is frequently observed if only He–$N_2$ is injected into the trap. Since the $H_2$ binding energy is relatively weak in general, however, it is found that collisions between a $H_2$-tagged molecule and cold Ne are nearly always sufficiently energetic to remove the tag. Undesirable $H_2$ tags can therefore be removed non-resonantly by injecting short pulses of Ne gas into the trap. In general, when attempting to tag an analyte, all three gases are used; that is, a pulse of mixed He–$N_2$ as well as a pulse of pure Ne. These are each fired from their respective pulse valve in the buffer gas system of sec. 4.2, with typical pulse durations of 7.5 ms and 2.5 ms for the Ne and He–$N_2$ pulses, respectively. It is known from experience that the optimal order of these two pulses varies by analyte species: tagging is most efficient for tropylium in sec. 5.1 if the Ne pulse precedes the tagging pulse, while the reverse is true for 1,3-benzodioxole (sec. 5.2) and indole (sec. 5.3). In each case, however, the Ne pulse has the effect of inhibiting undesirable $H_2$ tagging, thus increasing the overall $N_2$ tagging efficiency.

Somewhat curiously, a complementary phenomenon is regularly observed with $H_2$ tagging, which is referred to here as "substitution." As indicated, the average lifetime of $H_2$ tags is much shorter than for $N_2$ tags, since the $H_2$ binding energy is typically lower. Given the rough binding energies cited above, if a molecule tagged with $H_2$ were to collide with a $N_2$ molecule with a collision energy 300 K $< E_c <$ 1500 K, such a collision could remove the loosely attached $H_2$ tag while still leaving the $N_2$ bound to the molecule. This is observed regularly when attempting to tag analyte molecules, and occurs on a time scale ranging from several seconds, when the density of $N_2$ in the trap is still relatively high, to several minutes, when the $N_2$ density has nominally dropped to near zero.

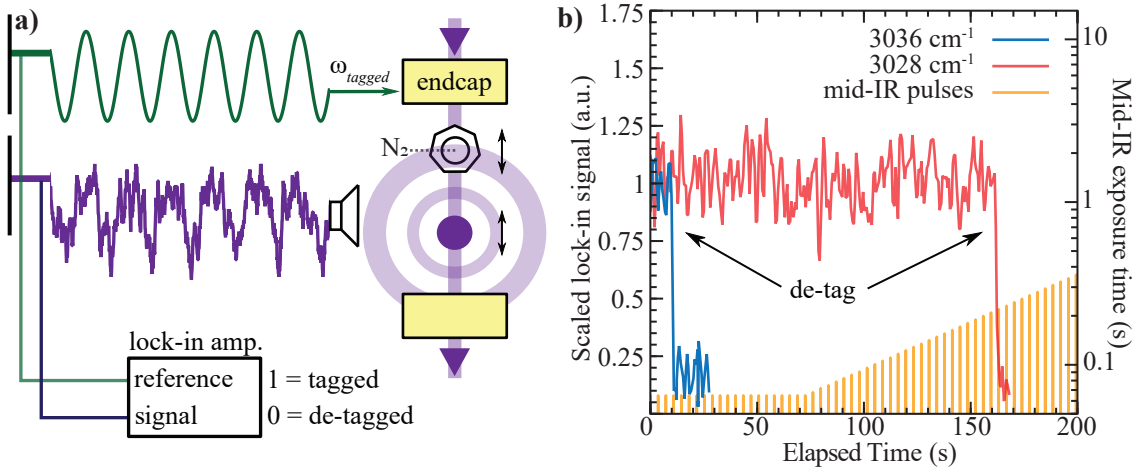


Figure 4.13: *a)* A cartoon indicating the single frequency lock-in measurement. A $^{88}Sr^{+}$ and tagged molecular ion are driven continuously at the tagged ensemble frequency, $\omega_{tagged}$. This continuously modulates the $^{88}Sr^{+}$ fluorescence intensity at $\omega_{tagged}$, as observed by the PMT. Both drive and PMT signals are compared by a lock-in amplifier, which indicates their degree of correlation. *b)* An example of two lock-in amplifier signals over time during a spectroscopic measurement. The ions are exposed to bursts of mid-IR light every ∼2.5 s, with burst durations increasing over time as shown on the right vertical axis. The molecule remains tagged, and the lock-in amplifier signal remains high, until a photon is absorbed and the tag ejected. Strong transitions de-tag the molecule after only a brief mid-IR exposure time (blue trace), while weaker transitions require greater exposure times to de-tag (red trace).

### Spectroscopy

Once the analyte molecule has been tagged spectroscopy can begin. The Coulomb crystal is continuously resonantly driven at $\omega_{tagged}$, producing a high lock-in signal. The OPO light source is then tuned to the desired frequency. Custom MATLAB® control software opens the normally closed mechanical shutter for brief periods to expose the tagged molecule to mid-IR light, and simultaneously monitors the lock-in amplifier signal for changes. A discontinuous drop in the lock-in signal to near zero, as in fig. 4.13, indicates that the molecule has de-tagged, and the control software ceases the experiment. The ions are first exposed to 20 bursts of mid-IR light, 65 ms in duration, with a 2.5 s delay between each burst. If de-tagging is not observed over the course of these 20 bursts, then subsequent bursts begin to increase in duration as $1 + \frac{1}{N}$, where $N$ is the

pulse number (see fig. 4.13, orange trace). Each successive shutter burst grows in length until reaching a preset maximum of 1.5 s, and subsequent bursts are fixed at this length. Ions are exposed to an additional 40 such bursts, corresponding to a total exposure time (the sum of all bursts) of ∼90 s. If the molecule does not de-tag after this cycle of bursts, the time required to de-tag for the OPO set frequency is recorded as >90 s. If the molecule does de-tag at any point throughout this process, the control software immediately identifies the elapsed time at which this occurred through the drop in the lock-in signal. The program then sums the total exposure time prior to de-tagging, and reports the de-tagging time as an interval: the prior exposure time plus the current burst duration (e.g. 60 – 61.5 s). Once de-tagging has occurred, the ions can be tagged again and the process repeated. In practice, ∼3-6 de-tagging measurements are typically made at each OPO frequency in a given spectrum for effective averaging. A best estimate of the true de-tagging time for that frequency is then calculated from the set of observed de-tagging intervals in a process described in ch. 5 and appendix A. Spectra are then reported by the equivalent de-tagging rate (inverse of the estimating de-tagging time) as a function of OPO frequency.

# Chapter 5

# Single Molecule Vibrational Spectra

This chapter presents the vibrational spectra of single molecules which have been recorded to date with this apparatus. Three molecular species have been studied in the C–H stretching region thus far, and each experiment highlights different capabilities of SMTS. The relevance of each species and the details of its observed spectrum are discussed in detail.

## 5.1 The Tropylium Cation

Tropylium ($C_7H_7^+$) is an aromatic carbocation with a seven-membered ring structure and $D_{7h}$ symmetry (see fig. 5.2). The unusual aromatic stability of this unique cation enables tropylium ($Tr^+$) to occur in numerous chemically important systems, making it a subject of frequent investigation since its first synthesis over a century ago [112]. $Tr^+$ has long been believed to be the primary $m = 91$ Da component of the fragmentation mass spectra of alkylbenzenes [113], and its role in mass spectrometry has been regularly investigated since this proposal [114, 115]. Conventional tagging spectroscopy experiments have recently helped to confirm this belief by identifying $Tr^+$ as a primary fragmentation product of the simple aromatic hydrocarbon toluene ($C_6H_5CH_3$), along with the isomeric benzylium structure ($Bz^+$, see fig. 5.2) [6, 116].

This ubiquity in the fragmentation of common hydrocarbons implies that $Tr^+$ likely plays an important role in astrochemistry as well. Mass spectra from the Cassini spacecraft directly observed $C_7H_7^+$ ions in the upper atmosphere of Saturn's moon Titan, suggesting that $Tr^+$ may be appreciably present there [117]. Additionally, these mass spectra have suggested that toluene is a common component of Titan's upper atmosphere as well, an argument further supported through atmospheric modeling [118]. Toluene is also believed to have been observed in the atmosphere/ionosphere [119] as well as on the surface [120] of the comet 67P/Churyumov-Gerasimenko by the ESA Rosetta mission. Ionizing radiation and collisions are common in atmospheric and interplanetary environments, so that this apparent abundance of toluene in the solar system strongly suggests that $Tr^+$ should be quite common in such systems as well.

In addition to this potentially significant presence in the solar system, $Tr^+$ and $Tr^+$–bearing molecules may also play important roles in the interstellar medium (ISM). Polycyclic aromatic hydrocarbons (PAHs) are believed to be major contributors to observed

interstellar IR emissions, as well as a significant source of interstellar carbon [121]. Methylated PAHs, in particular, have been observed in star forming regions previously [122], where they are regularly exposed to energetic UV photons. Conventional tagging spectroscopy experiments have found that dehydrogenation and ionization of certain methylated PAHs can lead to isomerization from the parent PAH structure, which bears only benzene-like six-membered rings, to a structure containing $Tr^+$-like seven-membered rings [123]. Furthermore, theoretical calculations have indicated that the barrier to this $Tr^+$-like isomerization is approximately 3.5-4 eV [124]. This energy is likely sufficient to ionize many methylated PAHs, and those species which have been observed in star forming regions previously are regularly exposed to photons of this energy, or higher. All of this evidence strong indicates that cationic PAH isomers which contain $Tr^+$ ring sub-units are likely present in such regions, where they may potentially contribute to the rich chemistry of these systems.

Given these many motivating factors, $Tr^+$ was chosen as the first species with which to demonstrate the SMTS method. Toluene vapor was ionized by electron impact through the process described in sec. 4.3.2, and individual mass 91 Da ions were loaded into the trap via the QMF. $Tr^+$ was then tagged with $N_2$, and the resulting C–H stretching region spectrum is shown in fig. 5.1. The spectrum in panel *a* of this figure was recorded from a single $Tr^+$ molecule. Each plotted point corresponds to a single de-tagging measurement. These measurements were made in 2 $cm^{-1}$ intervals from approximately 2950-2970 $cm^{-1}$ and 3028–3150 $cm^{-1}$. Between these two spectral regions the observed de-tagging rate was near the sensitivity limit of the measurements (de-tagging times near 90 s), and so measurements were made with coarser frequency sampling here. The expected geometry for the $Tr^+$–$N_2$ complex is shown in panel *a*. Structure optimization calculations were performed at the B3LYP-D3-aug-cc-pVTZ level of theory in the Gaussian 16 software package [125], indicating that the most energetically favorable tag geometry is with the

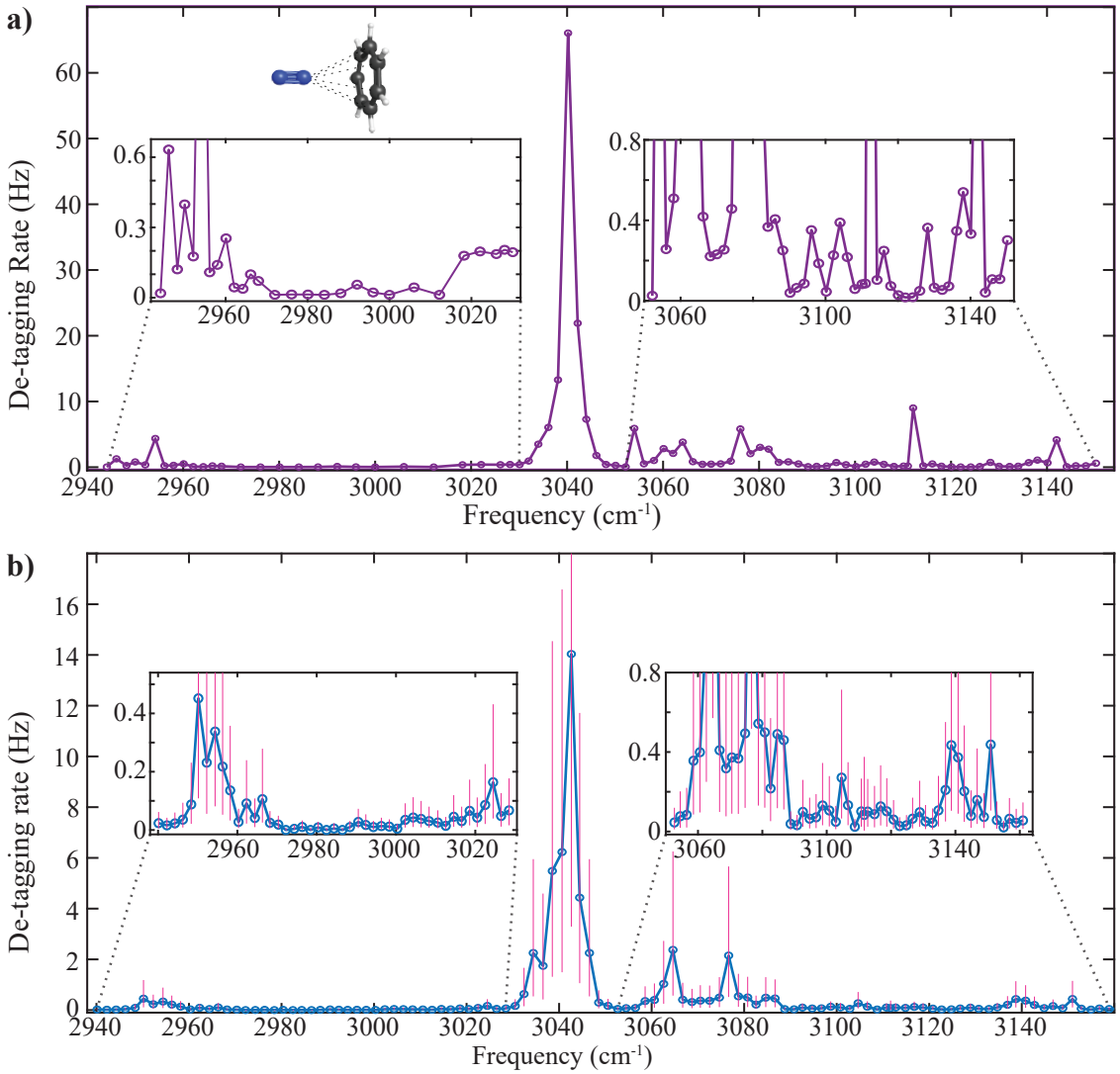


Figure 5.1: *a)* The C–H stretching region vibrational spectrum of a single $Tr^+$ molecule. De-tagging times were calculated according to the probability distribution described in app. A and converted to an equivalent de-tagging rate. *b)* The same spectral region was recorded across a total of eight individual molecules, for a total of three de-tagging observations at every frequency interval. Vertical bars are 95% confidence intervals (see app. A).

$N_2$ molecular axis oriented along the $Tr^+$ symmetry axis, orthogonal to the plane of the molecule, with a binding energy $E_b \approx 1000$ K and an ion tag separation of $\sim$3 Å.

The spectrum in panel *b* was recorded from eight individual $Tr^+$ molecules. Each set of measurements was performed on a single molecule, but reactive collisions between

the $Tr^+$ under investigation and residual $O_2$ gas in the chamber led to the periodic loss of the molecule from the trap. Whenever such losses occurred, a new $Tr^+$ was loaded into the trap and de-tagging measurements were made at the strong C–H stretching frequency at 3042 $cm^{-1}$ to confirm that the molecule was indeed $Tr^+$. Spectroscopy was then resumed where the previous data set left off. A total of eight sets of individual molecule measurements were required to produce the spectrum in fig. 5.1*b*, in which three de-tagging observations were made every 2 $cm^{-1}$ from 2944–3150 $cm^{-1}$. Three primary peaks were observed in this composite spectrum, with the strongest transition centered at 3042 $cm^{-1}$ and two smaller peaks at 3065 and 3077 $cm^{-1}$. Additionally, weak bands with amplitudes <1 Hz were observed near 2952 and 3140 $cm^{-1}$. These observations are compared with previously reported values and given tentative assignments in table 5.1.

The resonant de-tagging process is expected to follow an exponential probability distribution. Given the single de-tagging time observed at every frequency step in fig. 5.1*a*, and the set of three de-tagging times per point in fig. 5.1*b*, a maximum likelihood estimate for the most probable de-tagging time is calculated for each frequency point. The details of this calculation are discussed in app. A. This most probable de-tagging time is inverted to yield an equivalent de-tagging rate, and this rate is plotted versus OPO frequency to produce the molecular vibrational spectrum. The probability distribution used to compute this time may also be used to calculate a corresponding confidence interval for this result. Again the details of this calculation are highlighted in app. A. A 95% confidence interval is computed at every frequency point in the composite spectrum of fig. 5.1*b* and plotted as a vertical bar at each point. These intervals are asymmetric about the de-tagging data point as a result of the asymmetry of the de-tagging probability distribution (see app. A).

Ref. [6], by Wagner *et al.*, is the only known previous report of the gas phase $Tr^+$ spectrum which includes the C–H stretching region. The spectrum reported there was

| Frequency ($cm^{-1}$) | Prev. obs. ($cm^{-1}$) | Assignment |
|---|---|---|
| 2952 | – | 2× C–C stretch |
| 3042 | 3020[126],3036[6] | C–H stretch |
| 3065 | 3074[6],3080[126] | IR/Raman combination* |
| 3077 | 3074[6],3080[126] | IR/Raman combination* |
| 3140 | – | C–H($\perp$)/C–H($\parallel$)/C–C stretch |

Table 5.1: Observed $Tr^+$ vibrational frequencies, along with previously reported values (where applicable) and potential assignments. Starred entries could not be clearly assigned.

measured by the conventional, destructive tagging method using $N_2$ tags. The spectrum was recorded from an ensemble of many thousands of mass filtered ions produced from toluene ($C_6H_5CH_3$) and cycloheptatriene ($C_7H_7$) precursors, resulting in the observation of four strong vibrational bands. The isomeric benzylium cation ($Bz^+$) is believed to be produced along with $Tr^+$ during the fragmentation of both precursors, with toluene producing more of the analogous $Bz^+$ structure and cycloheptatriene producing more $Tr^+$. Two bands were ultimatately assigned to each of the two structures by varying the precursor and observing the subsequent depletion/enhancement of these peaks. This spectrum is plotted against the observations of this experiment in fig. 5.2, with the assignments color coded by isomer. As can be seen from the figure, the two bands assigned to $Tr^+$ align well with the spectrum observed in this work. Given the agreement between these results and those of ref. [6], the strong transition near 3042 $cm^{-1}$ is assigned to the lone dipole allowed, asymmetric C–H stretching mode of $Tr^+$ with $E_1'$ symmetry.

It is noteworthy that the two strong bands assigned to $Bz^+$ are entirely absent here, indicating that only $Tr^+$ was observed. In principle, the single molecule approach employed here is ideally suited to distinguish between two competitive isomers. If successive experiments are conducted loading a single molecule into the ion trap and measuring its spectrum, then some experiments should observe $Tr^+$ and others should observe $Bz^+$,

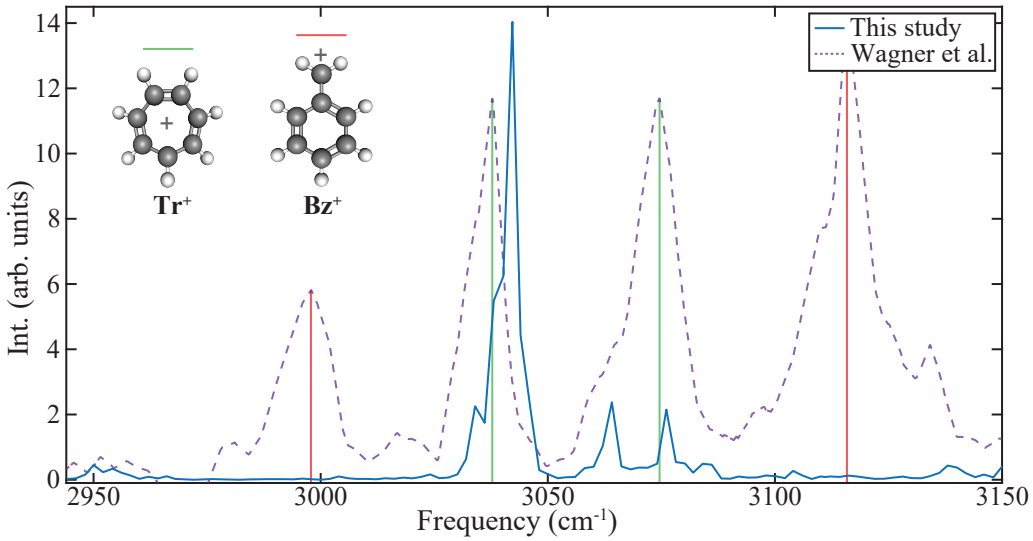


Figure 5.2: The averaged $Tr^+$ spectrum shown in fig. 5.1*b*, plotted against the spectrum observed by Wagner *et al.* in ref. [6] which has been scaled vertically to the current data set. The spectrum reported in this reference was recorded with a large ensemble of ions derived from a toluene precursor and tagged with $N_2$, the same precursor and tag species used in this experiment. Four strong transitions were observed there and assigned variously to $Tr^+$ and isomeric $Bz^+$. These assignments are indicated here with color-coded lines, showing that only $Tr^+$ is present.

with the number of occurrences of each dictated by the branching ratio for the decomposition of the precursor (toluene, in the case of fig. 5.2). Additionally, since toluene fragmentation has been shown to favor the $Bz^+$ structure, this isomer should have been frequently observed in this experiment.

By complete coincidence, however, the 422 nm laser cooling light to which the entire trap center is continuously exposed coincides with a strongly dissociative electronic transition in the $Bz^+$ isomer [127]. As a result, any $Bz^+$ ion which is injected during trap loading should readily dissociate. This argument is supported anecdotally by the observation that only ∼25% of the mass filtered 91 Da ions injected into the trap center during typical experiments are observed to be $Tr^+$. The remainder of loaded ions are molecular fragments of mass 65 Da, likely the cyclopentadienyl cation ($C_5H_5^+$). If the beam of mass 91 Da ions directed toward the trap consisted of isomerically pure $Tr^+$

then the appearance of such fragments would be very unlikely, given that the $Tr^+$ is a resonance stabilized aromatic structure. The ∼3:1 ratio for the occurrence of $C_5H_5^+$ ions versus $Tr^+$ ions in the trap is consistent with photofragmentation of $Bz^+$ ions, however, given that the toluene precursor should produce this isomer at ∼3× the rate of $Tr^+$ [6]. Thus, while SMTS is ideal for identifying and distinguishing between competing isomers, it was not necessary here due to this coincidental photoionization.

The two peaks observed at 3065 and 3077 $cm^{-1}$ align well with the strong band at 3074 $cm^{-1}$ in ref. [6], even mimicking its somewhat asymmetric shape. Wagner *et al.* argue that both $Tr^+$ and $Bz^+$ contribute to this band, which can explain the discrepancy between the relative amplitudes observed in both experiments, but were ultimately unable to make an assignment to a specific vibrational mode. The C–H stretching region has been measured previously for $Tr^+$ in solution, where this band was also observed (∼3080 $cm^{-1}$) and also could not be assigned [126]. This work shows that there is underlying structure to this peak which was not previously resolved. Neither underlying peak observed here aligns well with an overtone or simple combination of known IR active $Tr^+$ vibrational modes. Multiple combinations of IR and Raman active modes can be constructed, however, which yield approximately the correct frequency and which are allowed by symmetry. Additionally, IR inactive vibrational modes are known to become weakly IR active in many systems in the liquid phase [128], where symmetry breaking distortions induced by neighboring molecules is thought to be responsible for such effects. The presence of the $N_2$ tag along the molecular symmetry axis may possibly provide such symmetry breaking distortion, making IR forbidden transitions weakly accessible. Two relatively strong Raman transitions have been observed in $Tr^+$ in solution previously [126] at 3060 and 3075 $cm^{-1}$. These modes are very nearly equal in frequency to those observed here, suggesting that symmetry breaking from the presence of the tag may enable these modes to be driven (see app. B). Neither hypothesis can be definitively adopted based on the

observations here, however. These peaks are therefore suggested to arise from Raman modes or Raman/IR mode combinations.[1]

The weak features near 2952 and 3140 $cm^{-1}$ have not previously been identified due to their low relative amplitudes. The data of Wagner *et al.* shows a possible subtle feature near 2952 $cm^{-1}$, but this is very close to the noise floor of the measurement and cannot be definitively distinguished from noise. $Tr^+$ is known to have a strong, asymmetric C–C stretching mode ($E_1'$ symmetry), which has been previously observed between 1477 $cm^{-1}$ [6, 126] and 1486 $cm^{-1}$ [116]. Recall from sec. 3.1.2 that mechanical anharmonicity leads to the uneven spacing of vibrational energy levels, thus causing overtone vibrations to have energies slightly less than an integer multiple of the fundamental transition energy. In this context, the weak band at 2952 $cm^{-1}$ may be assigned as the first overtone of the $\sim$1480 $cm^{-1}$ C–C stretching fundamental. Initially, this overtone would appear to be symmetry disallowed, as the symmetry of the overtone is $E_1' \otimes E_1' = A_1' \oplus A_2' \oplus E_2'$, and none of these terms coincides with the symmetries of the dipole moment components in the $D_{7h}$ symmetry group. As is shown in app. B, however, the presence of the $N_2$ tag reduces the symmetry of the system to a point group for which this overtone is allowed. Combinations of the other low energy modes of $Tr^+$ may be formed to reach approximately the same frequency (e.g. $2v_4 + v_8$ for $v_4$ and $v_8$ reported in ref. [116]), but such combinations do not satisfy the symmetry selection rule and are therefore not IR active. Similarly, higher overtones of other low energy modes may yield approximately the correct frequency, but the transition moment for a higher overtone is much lower than that of a first overtone, making such a transition unlikely. Thus, the first C–C stretching fundamental is the most likely assignment for this mode. A more detailed discussion of this symmetry-based argument is presented in app. B.

[1]Ref. [126] contains a detailed analysis of all modes allowed by symmetry, along with their IR and Raman activities.

The assignment of the weak band near 3140 $cm^{-1}$ is more challenging. The relative amplitude of this band is lower than the sensitivity limit of previous studies, and thus the transition is sufficiently forbidden to be difficult to reproduce computationally. The observed frequency of this feature does not align well with overtones or simple combinations of known $Tr^+$ vibrational modes, but the feature is repeatable enough to be statistically significant and unlikely to be the result purely of noise. A handful of possible combinations of IR active modes can be made to produce approximately the correct frequency, but most are not symmetry allowed. On the basis of the symmetry analysis presented in app. B, this peak is tentatively identified as a combination of three low energy modes: an out-of-plane C–H wag, an in-plane C–H rock, and an in-plane C–C stretch. This assignment is tentative and may not be the correct interpretation of the observed band, thus a more detailed theoretical analysis is needed here.

## 5.2 1,3-Benzodioxole Fragmentation

1,3-Benzodioxole ($C_6H_4O_2CH_2$) is a heterocyclic organic molecule with $C_{2v}$ symmetry, comprising an acetal group bound to a benzene ring (see fig. 5.3, right). While the number of systems in which the 1,3-benzodioxole (BDO) molecule itself plays a significant role is limited, it is a structural component in many larger molecules with important chemical and biological applications [129]. This system has been the subject of previous theoretical interest owing to its unusual non-planarity arising from the anomeric effect [130]. Far-IR, Raman, UV absorption, and laser induced fluorescence methods have all been employed to characterize this unusual ring puckering behavior, helping to improve potential energy surface calculation methods used to understand this anomeric effect [131, 132, 133]. While ring puckering vibrations are generally too low in energy ($\sim$100 $cm^{-1}$) to observe via tagging, the demonstrated sensitivity of SMTS to weak combina-

tion transitions raises the possibility of observing puckering modes in combination with higher energy vibrations. Anomeric non-planarity may therefore potentially be observable in the BDO cation via SMTS. Both mid-IR [60] and far-IR [132, 134] spectra of the neutral molecule have been reported previously, but no known data for the vibrational spectrum of the corresponding cation has been published to date. The BDO cation was therefore chosen as a model system to characterize the sensitivity limits and identification capability of SMTS for molecules without known spectra.

In practice, when such experiments were attempted, it was found that the ion loading scheme described in sec. 4.3.3 was incapable of loading the BDO cation ($m = 122$ Da). All such attempts instead resulted in the trapping of the dehydrogenated BDO fragment cation ("BDO-H", $C_6H_4O_2CH^+$). This molecule has mass $m = 121$ Da, in spite of the fact that the QMF was set to filter out all ions of mass $m \neq 122$ Da. The QMF filters ions at the 1 Da resolution level with unit efficiency, thus implying that the transition from BDO to BDO-H occurred after the ions left the QMF. As previously noted, ions are created in the EI source with a kinetic energy of 18 eV, and thus enter the ion trap center with this average kinetic energy before colliding with cold Ne atoms. From the center of mass perspective of a colliding BDO–Ne pair, this results in a collision energy of many eV, thus resulting in collision-induced fragmentation from BDO to BDO-H. Efforts were made to form BDO ions at lower initial kinetic energies, but even the lowest such energies which could be practically realized proved too high to avoid this fragmentation process in the ion trap. This practical complication therefore precluded the study of the parent BDO cation, and the BDO-H fragment ion was studied instead.

The vibrational spectrum of BDO-H in the C–H stretching region was recorded from 3020–3212 $cm^{-1}$, with data collected in 4 $cm^{-1}$ increments. A total of five individual BDO-H molecules were needed for this measurement, as molecules were again periodically lost from the trap due to reactive background gas collisions. The resulting composite

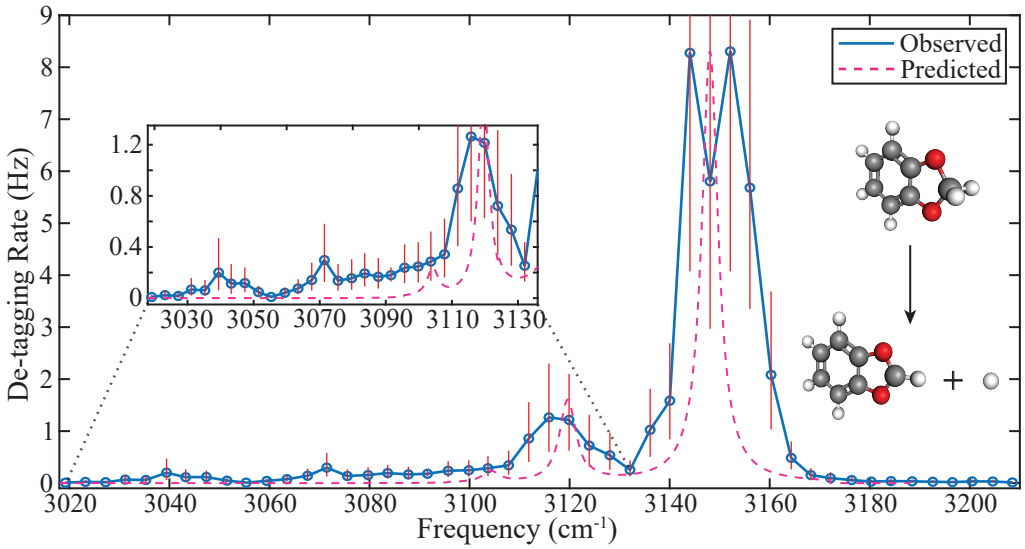


Figure 5.3: The C–H stretching region vibrational spectrum of the BDO-H fragment. This spectrum is a composite of measurements made on five individual molecules. The dashed line is a computed spectrum assuming that hydrogen loss occurs on the methylene bridge of the acetal group. The dominant observed feature at 3148 $cm^{-1}$ agrees well with the methylene bridge C–H stretching mode, and the minor band at 3118 $cm^{-1}$ arises from an asymmetric benzene ring C–H stretch.

spectrum is shown in fig. 5.3, with five de-tagging measurements made at each frequency point. This data was averaged, and 95% confidence intervals calculated, according to the equations derived in app. A in the same fashion as for $Tr^+$. Two primary transitions were observed: one strong band centered at 3148 $cm^{-1}$, and one weaker band centered at 3118 $cm^{-1}$. Whenever molecule losses occurred, a new ion was loaded into the ion trap and de-tagging measurements were made at the strong 3148 $cm^{-1}$ transition to verify the identity of the new molecule. Two additional weak bands are possibly observed near 3040 and 3072 $cm^{-1}$, but the signal-to-noise here is relatively low and further measurements are required to determine if these features are truly real. Even if so, their low de-tagging amplitudes suggest that they would likely arise from combinations or overtones of unknown lower energy fundamental vibrations.

Vibrational structure calculations for BDO-H were performed at the B3LYP-D3BJ/aug-cc-pVTZ level of theory in to order compare these predictions with the observed spectrum.

This calculated spectrum is plotted as a dashed line in fig. 5.3. It is plotted with an artificial transition linewidth of 6 $cm^{-1}$ FWHM, which is equal to the spectral width of the mid-IR OPO light. This plot therefore represents the expected spectrum that one would observe if the transitions were limited by the OPO linewidth rather than the radiative lifetime. The amplitude of this calculation is scaled to that of the observed spectrum, and is shifted down in frequency by 108 $cm^{-1}$ to achieve the greatest agreement between the two.

As can be seen from the figure, the two strongest predicted modes align very well with the observed bands, excepting this frequency offset. The observed vibrations are therefore assigned to the theoretically predicted vibrational modes. The strongest of these vibrations, predicted at 3148 $cm^{-1}$ (after applying the frequency offset) arises from the stretching motion of the lone hydrogen atom left on the methylene bridge of the acetal group ($A_1$ symmetry). This is followed by an in-plane, asymmetric C–H stretching mode of the benzene ring hydrogen atoms at 3120 $cm^{-1}$ ($B_2$ symmetry). An additional benzene ring stretching mode is predicted at 3104 $cm^{-1}$ ($A_1$), but the calculated amplitude of this mode is below the background of the observed spectrum and was therefore not distinguishable experimentally.

As previously discussed, technical complications necessitated that this experiment be performed with the BDO-H ion rather than the parent BDO ion. In spite of this difficulty, the resulting spectrum helps to validate the assertion that the method and apparatus described here are generalizable to a broader class of molecular ions. While the analysis of the $Tr^+$ spectrum was made primarily on the basis of previously observed vibrational transitions, the analysis here of BDO-H was made entirely through *ab initio* calculations. This result therefore demonstrates that this single molecule method can record molecular spectra which can be accurately interpreted to provide structural information about unidentified analyte molecules. The utility of the BDO-H ion extends beyond this simple

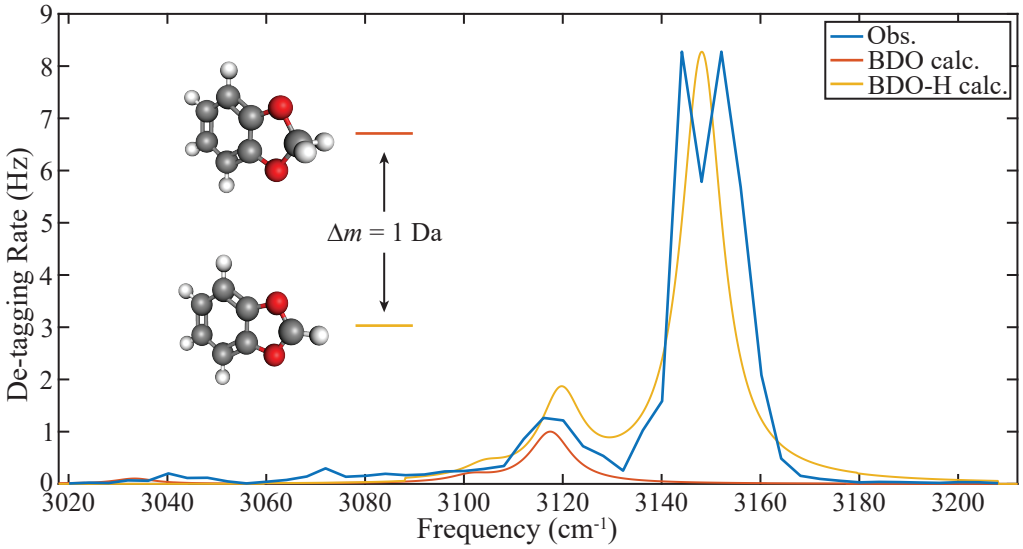


Figure 5.4: The observed C–H stretching lines of BDO-H plotted against calculated spectra for both the parent BDO cation ($m = 122$ Da) and the BDO-H fragment ion ($m = 121$ Da). Both calculations were done at the B3LYP-D3BJ/aug-cc-pVTZ level of theory and down-shifted in frequency by 108 cm$^{-1}$.

proof-of-principle for the generality of this method, however. Indeed BDO-H is a natural platform for benchmarking the performance of the ion trap.

As discussed in sec. 4.6.1, the masses of trapped molecular ions in this experiment are read out non-destructively through the tickle method. Experience has shown this technique to have a mass resolution limit of $\sim$1 Da, on the basis that molecular masses measured by the tickle technique typically differ from the programmed QMF mass by $\lesssim$0.5 Da. In spite of the relatively simple difference in the structure of the BDO and BDO-H cations, such a structural change should have an appreciable impact on their respective vibrational spectra. While the spectrum of the BDO parent ion could not be measured here, it can be calculated just as with BDO-H in order to compare this to the observed spectrum. This is shown in fig. 5.4, comparing the experimental result with the calculated spectra for both the BDO and BDO-H cations, where the BDO calculation was also performed at the B3LYP-D3BJ/aug-cc-pVTZ level of theory and down-shifted in frequency by 108 cm$^{-1}$. The vibrational calculation for BDO indicates that the benzene

ring C–H stretching frequency is relatively unchanged between the two species, but the methylene bridge C–H stretching frequency is red-shifted by ∼200 $cm^{-1}$ (out of view of fig. 5.4). This is likely due to the increased mass involved in the vibration, since two hydrogen atoms are present on the methylene bridge rather than one for BDO-H. The predicted benzene ring stretching mode aligns well with the observed weak peak, as is the case for the BDO-H calculation. Additionally, the strongest observed vibration aligns very well with the BDO-H methylene C–H stretch but lays at a frequency which should be entirely devoid of features according to the BDO calculation. The experimental spectrum therefore clearly demonstrates that only the 121 Da BDO-H ion was studied, and not the 122 Da BDO parent ion. This validates the assertion that the mass resolution of the tickle measurement is <1 Da. If lower ion injection energies during trap loading can be achieved in future experiments, it may be possible to reliably load the BDO cation rather than BDO-H and measure this spectrum to further validate this claim.

It should also be noted that both calculated spectra in fig. 5.4 are plotted with artificial linewidths of 10 $cm^{-1}$ FWHM, approximately replicating the widths of the experimentally observed bands. This indicates that the observed linewidths are not limited by the OPO spectral width. The dominant broadening mechanism here is due to predissociation of the tagged molecule, as discussed in sec. 3.3.2. This observed transition linewidth of ∼10 $cm^{-1}$ (≈ 300 GHz) therefore suggests that the time scale for the IVR process which leads to predissociation is $\tau_{IVR} \approx \frac{1}{300\times10^9} \approx 3 \times 10^{-12}$ seconds in this system.

## 5.3 Indole Photofragmentation

Indole ($C_8H_7N$) is an aromatic, heterocyclic molecule with $C_s$ symmetry, comprising a pyrrole ring bound to a benzene ring (see fig. 5.5 right). It is an important metabolite

which occurs naturally in many biological systems and is known to serve as a signalling molecule in many cellular systems, including common bacteria [135] and the microbiota of the human intestinal system [136]. Numerous indole derivatives and molecules which contain indole as a structural component are naturally abundant, including the amino acid tryptophan, and play important roles in key biological processes [137], making indole among the most biologically important small polyatomic molecules.

Additionally, given its aromatic stability, indole is believed to be a potential constituent of the interstellar medium (ISM). Although it has not yet been identified definitively in interstellar emissions, numerous similar heterocyclic nitrogen-bearing molecules have been detected via mass spectrometry (and related methods) in both terrestrial meteorites [138] as well as samples collected from near-earth asteroids [139]. This potential extraterrestrial presence has motivated previous work to measure the rotational spectrum of indole to aid in microwave astronomy searches [140]. Given the ubiquitous presence of ionizing radiation and collisions within the ISM, any appreciable presence of indole in the ISM would necessarily mean the presence of indole cations as well, which may be potential drivers of interstellar chemistry. This hypothesis has motivated previous vibrational spectroscopy studies of the indole cation, which measured the N–H stretching region with conventional tagging methods [141], but both the resolution and spectral range of these measurements were limited. A more complete vibrational spectrum of this cation would therefore be extremely valuable in the search for evidence of indole in interstellar emission bands.

Although indole is a solid at room temperature, its relatively high vapor pressure ($\sim$10 mtorr) is sufficient for loading via the solid sample input manifold described in sec. 4.3.3. Cations were generated from the vapor of solid indole, producing a sufficient ion flux to efficiently load single cations into the quadrupole trap. It was found, however, that the indole cation suffered a limited lifetime once trapped. On a number of attempts,

trapped cations survived in the trap just long enough (∼1 minute) for a chirped tickle scan measurement to be made to verify that their mass was indeed that of indole ($m = 117$ Da). Shortly after this verification, however, each trapped molecule fragmented and left behind a mass $m = 90$ Da ion instead. This dissociation was observed on five different occasions, indicating that the trapped lifetime for indole in this apparatus is limited to the few minute time scale.

The Ne buffer gas used for trap loading is very quickly pumped away from the trap center due primarily to cryo-sorption, with a $1/e$ pump out time much less than one second. The observed one minute fragmentation lifetime therefore indicates that this could not have been the result of energetic collisions with Ne buffer gas. As was indicated in sec. 5.1 and sec. 5.2, molecules can be periodically lost from the trap due to reactive background gas collisions. This loss would primarily occur because the masses of charged products that result from such a reaction cannot be stably confined. Thus, in principle, it is possible that the indole cation could react with background gas such as $O_2$ and yield a charged product of mass $m = 90$ Da which would remain trapped. This explanation is also unlikely, however, given that five successive fragmentation events were observed. During normal operation, such events occur randomly with a typical rate of once every one to two days. The likelihood of seeing five such reactions in relatively short order is therefore low. A final possibility is that the molecules which were trapped were not the indole cation, but rather some other molecule of mass $m = 117$ Da present in the chamber background. The QMF cannot distinguish between analyte molecules and background molecules of the same mass, therefore any background species with the same mass as the desired analyte would be passed through the QMF along with that analyte. Mass spectra of the background gas in the QMF chamber observe a mass 117 Da ion flux of ∼200 Hz (see fig. 4.6), some three orders of magnitude lower than the flux of indole cations exiting the QMF during loading. The likelihood of loading unwanted background molecules on

five separate occasions is therefore very low.

In light of these considerations, the most likely explanation for the cause of the observed fragmentation events is off-resonance photodissociation. 422 nm laser cooling light is continuously present in the ion trap center, as required by the single molecule tagging technique. The energy per photon of this light (2.94 eV) is comparable to the lower bond energies of many polyatomic molecules, so that a molecule which scatters a 422 nm photon may have an appreciable probability of fragmenting. Previous tagging measurements have shown that the indole radical cation has a broad electronic absorption feature centered near 335 nm [142]. This resonance is sufficiently far detuned from the cooling laser frequency that off-resonance photon scattering events should occur very infrequently, but any such scattering event may pose a threat to the molecule. The observed fragmentation events are consistent with this process, as the long fragmentation time corresponds to a 422 nm photon scattering rate $<$0.1 Hz, as would be expected for such a large wavelength detuning.

This uncontrolled photo-fragmentation process precluded the measurement of the indole cation vibrational spectrum here. This system is still of scientific interest, however, in spite of this technical setback. As previously mentioned, ions are common in the interstellar medium due to the frequent presence of high energy radiation and collisions, which would therefore lead to the occurrence of the indole cation if indole itself is present in the ISM. Such ionizing sources would also fragment indole molecules in the ISM in addition to simply ionizing them. It may therefore be reasonably supposed that if indole exists in interstellar space, the products of indole photo-fragmentation would likely exist there as well. Theoretical studies of the fragmentation of the neutral indole molecule have indicated that a likely fragmentation pathway is through the loss of either hydrogen cyanide (HCN) or hydrogen isocyanide (HNC), leaving behind a charged $C_7H_6^+$ fragment with mass $m = 90$ Da [143], exactly as is observed in this work. Additionally, both

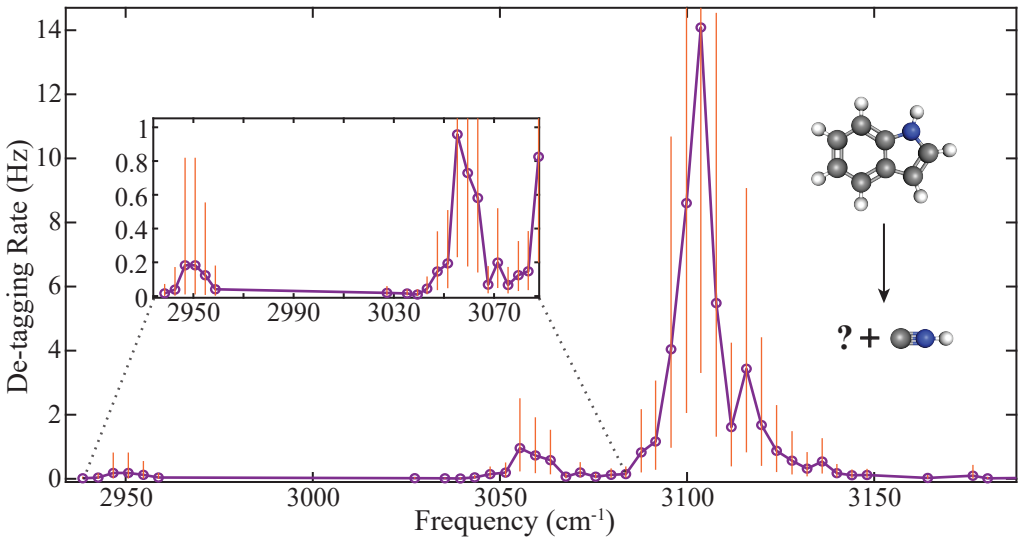


Figure 5.5: The C–H stretching region vibrational spectrum of a single indole photo-fragment. A trapped indole cation quickly dissociated under the influence of the 422 nm cooling laser light, resulting in this 90 Da fragment ion whose structure is currently unknown.

potential neutral products of this fragmentation, HCN and HNC, have been observed in abundance in a variety of astronomical environments [144]. This therefore raises a natural question as to whether or not the predicted $C_7H_6^+$ indole fragment can be detected in interstellar emissions. Not only would such an observation strongly imply indole's presence in interstellar space, but a clearer understanding of the fragment ion's structure would enable additional studies regarding any potential role it might play in interstellar chemistry. Additionally, tagging spectroscopy has already been demonstrated as valuable tool for identifying molecules in the ISM [102, 104], making it ideal for this task.

Given these numerous motivating factors, SMTS was therefore used to record the vibrational spectrum of the observed indole photo-fragment ion in the C–H stretching region. The result of this measurement is plotted in fig. 5.5. A single indole photo-fragment was used for this data set, where the spectrum was recorded from 2938-3180 $cm^{-1}$. This spectrum is a preliminary data set, and was therefore not measured in

completely uniform steps across the spectral range as in the preceding sections. De-tagging measurements were made in 4 $cm^{-1}$ steps in the range from 3036–3148 $cm^{-1}$, across the strongest observed bands, as well as a smaller range from 2938–2958 $cm^{-1}$. Several other data points have been measured at different frequencies scattered about the spectrum, but measurements have yet to be taken between these two primary regions of interest. A set of three total de-tagging measurements were made at each frequency point plotted in this spectrum. These measurements were averaged together, and 95% confidence intervals calculated, in the same fashion as described in the preceding sections.

Although this data set is preliminary and additional measurements are needed, this spectrum reveals three to four clear vibrational transitions. The strongest of these is centered approximately at 3104 $cm^{-1}$, de-tagging at a rate of $\sim$14 Hz. A possible smaller satellite peak appears nearby at 3116 $cm^{-1}$, but additional measurements are need to reduce statistical amplitude noise, along with measurements in finer frequency steps in order to confirm that this is indeed a real peak. After this strong primary band, the second strongest observed transition lies lower in frequency at 3059 $cm^{-1}$ with a de-tagging amplitude of $\sim$1 Hz. An additional transition, which is weaker still, is observed at approximately 2950 $cm^{-1}$. The observed de-tagging rate for this transition is comparable to that of the proposed overtone and combination bands observed in sec. 5.1, suggesting that this peak may possibly have a similar origin.

These three (possibly four) vibrational modes have yet to be assigned, as the structure of the observed fragment ion is still unknown. More spectroscopic measurements are needed to fill in the empty spaces in this data set and search for any additional C–H modes in this range. The expansion of this data set to a larger frequency range would be even more valuable, as any additional vibrational modes which can be observed would significantly aid the structure assignment process. Such experiments are currently underway. Additionally, theoretical work is needed to predict the fragmentation pathways and

resulting products for the indole cation, so that spectra of proposed fragment geometries may be simulated and compared to the experimental observations. This computational effort is also currently underway with collaborators from ref. [143].

While the effort to interpret these results is currently ongoing, even these preliminary measurements provide a powerful illustration of the promising applications for SMTS. Single molecule photo-fragmentation reactions, as well as single ion-neutral chemical reactions, could be readily induced within the quadrupole ion trap, and the products of these reactions could be rigorously characterized through SMTS. A full description of these proposed experiments is discussed in sec. 6.2, but the primary point of interest here is that the products of such reactions could be determined through SMTS, with sensitivity even to very subtly different product isomers. Additionally, the ultra-high vacuum and cryogenic temperature of the experimental platform means that such reactions would take place in an environment which resembles the ISM in important ways. This apparatus and technique therefore constitute a promising new tool for the investigation of astrochemically relevant molecules.

# Chapter 6

# Applications and Future Work

This chapter highlights promising future avenues of research utilizing the apparatus and SMTS technique described in this work. Potential applications for this novel spectroscopic tool include rare sample characterization, ultra-sensitive analysis of complex mixtures, and characterization of chemical reactions.

## 6.1 Mixture Analysis

Among the most fundamental potential applications of SMTS is the study of complex chemical mixtures. In this discussion, the term "mixture" will be taken to mean any ensemble of molecules which is heterogeneous in either the chemical species or the isomeric species present in the ensemble. An ensemble of large, floppy molecules which are chemically identical would therefore constitute a mixture, as such molecules can typically adopt many different possible conformations. This definition, though unorthodox, is useful in this context, because even the most subtly different isomers will have unique and distinguishable vibrational spectra. A "mixture" here may therefore be regarded as any ensemble containing more than one species with a unique vibrational spectrum.

This is the scientific arena in which the single molecule tagging method shows perhaps the greatest promise, as mixtures of this type are all but impossible to avoid in an ensemble of molecules. Numerous powerful techniques have been developed to separate molecules based on their chemical and isomeric structure. Modern mass spectrometry is extraordinarily sensitive and efficient at separating chemicals by mass. Techniques such as chromatography and ion mobility spectrometry can provide structural sensitivity which can't be achieved with mass spectrometry, through diffusion or collisional separation processes which are sensitive to a molecule's structure. None of these separation techniques, however, can achieve unit efficiency in separating all unique isomers of a given molecular species, especially for those isomers which are only slightly different [145, 146]. This is especially true for large floppy molecules which, as noted, can isomerize in many different ways. Indeed as the size of a molecule increases, the number of accessible isomers increases significantly, reaching $10^{12}$ for kilo-Dalton scale molecules [86].

Structural isomers of a chemical, even those isomers which are only subtly different, possess unique vibrational spectra which provide a more powerful means to distinguish

between them. A number of techniques have been developed in recent years to combine the structural sensitivity of IR spectroscopy with existing separation methods in an effort to better distinguish between the components of chemical mixtures [147, 148]. Among the greatest barriers to using spectroscopy as an effective analytical tool for mixtures, however, is the issue of spectral congestion. The vibrational spectrum of a single chemical isomer may be inherently complex, depending on the size and composition of the molecule, exhibiting many features in its spectrum. Each component in a mixture contributes further unique features to the spectrum of that mixture, resulting in a sum of the spectra of all components. Such a spectrum is often intractably complex and difficult to interpret for even a simple mixture, thus limiting the ability to extract meaningful information. Methods which employ spectroscopy as a means of mixture analysis therefore require many separation steps that precede spectroscopy, in order to reduce the complexity of each mixture being analyzed as much as possible, though never with unit efficiency. These experiments must therefore rely on libraries of spectra of potential mixture components, along with analysis algorithms to interpret observed features and relative amplitudes to attempt to assign spectral features to specific chemical species [149]. Thus, while such experiments have advanced the capabilities of spectroscopic mixture analysis, they are still imperfect and typically require significant technical overhead.

Additional techniques have been developed to increase the sensitivity of vibrational spectroscopy to the isomeric composition of a sample. These methods apply the technique of spectral hole burning, typically in concert with conventional tagging spectroscopy [150, 151]. Two independently tunable mid-IR light sources, pump and probe, are needed for such experiments. Tagged molecules are exposed to pump light which is swept over a broad frequency range, and interrogated at a later stage by probe light at a fixed frequency. Resonant de-tagging of a given isomer by the pump beam then reduces the tagged population seen by the probe beam, thus reducing the de-tagging signal induced

by the probe. Two primary issues arise with such methods, however. The necessity for a second light source increases both experimental costs and operational complexity, continuing the trend illustrated here that current methods for mixture analysis with isomeric sensitivity require significant technical overhead. Additionally, this hole burning scheme only works if the transitions of different isomers are at least approximately known, so that they may be driven selectively to add or remove isomer population from a mixture being probed. These methods are therefore costlier as well as less general.

All issues cited to this point can be immediately circumvented, however, by operating at the single molecule level. In some sense, a single analyte ion constitutes a sample of perfect purity: only one chemical species and isomeric structure is present. The vibrational spectrum of this sample is necessarily not congested, and can contain no ambiguity about which species contributes to the observed features. Conventional spectroscopic methods rely on measuring the spectra of many molecules in parallel, resulting in a congested and difficult to interpret sum of all spectra. This same sample can instead be analyzed sequentially, one molecule at a time. Each single molecule spectrum can determine the exact chemical species and isomeric structure of the analyte molecule. Many sequential spectra of individual molecules drawn from a chemical sample would therefore reveal the full chemical and isomeric composition of that mixture. Additionally, this is all achieved with only one step of separation (mass filtration) and one IR light source. The data acquisition time of this method is inherently much longer than previously discussed methods, but this is compensated for by the clarity of the resulting data and the comparatively much simpler experimental infrastructure. Thus the detailed isomeric landscape of a mixture can be readily analyzed via sequential single molecule measurements, making the method developed in this work a powerful new tool for the analysis of complex mixtures which would be intractable by conventional analytical means.

## 6.2 Cold Chemical Reactions

The most promising applications of this method all stem from the potential for highly accurate mixture analysis, since chemical and isomeric mixtures arise in numerous important contexts. Reaction products are a prime example of this. The products of ion-neutral reactions involving polyatomic molecules of intermediate size can often follow several different reaction pathways to produce multiple ionized products [152, 153]. Reactions induced in an ensemble of reactant molecules will therefore produce a mixture of chemically distinct products, in general. Depending on the size and structural complexity of these products, they may each in turn adopt one of multiple possible isomeric structures, leading to a potentially complex mixture of chemical and isomeric species. The same is true for the products of unimolecular dissociation processes, such as photo-dissociation and collision-induced dissociation (CID). Tens to hundreds of reaction pathways may be accessible in such processes, depending on the initial excitation energy [143, 154], further increasing the number of potential product species. The ability to analyze such a product mixture at the single molecule level would simplify the characterization process while eliminating ambiguity about product identities. Previous experimental work has attempted to harness this enormous potential for single molecule reaction analysis [155, 156]. Such methods demonstrated to date are far from generalizable, however, as they are restricted to very small molecules and rely on optical manipulation of the quantum states of participating particles. The generality of SMTS, however, makes it an ideally suited tool for the analysis of single molecule reactions.

A process entirely analogous to the one described in sec. 6.1 could be implemented to identify all chemical and isomeric products from such reactions. Upon trapping a single reactant molecule, a reaction can be induced via the desired mechanism: introducing neutral reagent molecules to induce an ion-neutral reaction; introducing UV or

visible light to induce a photo-dissociation reaction; or introducing inert gas to serve as energetic collision partners for CID. The ionic products created in the ensuing reaction, provided that their mass-charge ratio falls within the stability range of the ion trap, will remain confined. If more than one charged product is trapped, products can be selectively ejected from the trap by mass, so that one molecule can be spectroscopically interrogated at a time. This measurement reveals the identity of that product down to the structural isomer level due to its unique vibrational spectrum. The trap is then emptied, a new reactant molecule loaded, and the process repeated. Measurements of the same product molecule can be repeated many times to determine any and all structural isomers produced for that particular mass. The process can then be repeated for any reaction products of different masses as well. The total number of occurrences of each observed chemical species and isomeric structure, as a fraction of the total number of reaction experiments performed, provides a precise measurement of the branching ratio between each possible product. The experiments reported in sec. 5.1 demonstrate these capabilities, as two isomers of identical mass were produced in unimolecular dissociation processes, and effectively distinguished from one another on the basis of their vibrational spectra. While it is true that the competing $Bz^+$ isomer was not truly present in the spectroscopic mesurements made their, its spectrum is known to differ significantly from that of $Tr^+$. Had it occurred, therefore, it would have been readily distinguished from the competing $Tr^+$ isomer, exactly as would be necessary in the analysis of single molecule reactions. Furthermore, work is currently underway to expand upon the indole data set reported in sec. 5.3, in which multiple isomeric species are observed and distinguished.

As alluded to at the end of sec. 5.3, the environment experienced by ions in the cryogenic ion trap used here resembles the ISM in several key respects. Additionally, as indicated in sec. 3.2, ionizing radiation and energetic collisions are primary sources of ions in the ISM [74], and these ions are believed to play an important role in interstel-

lar chemistry [73]. In general, the reactivity of a chemical is strongly influenced by its conformational structure, especially in the case of reactive radical cations like the indole cation of sec. 5.3 [157]. Detailed characterization of the chemical and isomeric product structures resulting from photo-dissociation of astrochemically relevant molecules would thus help to significantly advance the understanding of astrochemical processes. Of more terrestrial interest, the method of tandem mass spectrometry (MS/MS) employs CID to identify molecular ions by their unique fragmentation mass spectra [158]. This method has gained widespread adoption for its enhanced sensitivity to molecular structure compared to traditional mass spectrometry [159]. The characterization of fragmentation pathways via SMTS would provide more complete information about these dissociative processes, enabling dissociation products and isomeric structures to be mapped across a range of CID conditions relevant to tandem mass spectrometry. SMTS therefore presents a natural complement to the powerful MS/MS method, with the potential to increase the amount of valuable information which can be abstracted through this method.

## 6.3 Rare Sample Analysis

As illustrated in sec. 6.1, single molecule samples are necessarily pure, allowing for unambiguous interpretation of observed spectra. Operating in the single molecule regime introduces an additional intrinsic benefit. While the data acquisition speed of SMTS is far below most competing methods, this technique consumes the minimum amount of sample necessary for analyte identification: one molecule. On this basis of sample consumption, therefore, SMTS constitutes the single most efficient method for identifying molecular analytes. A natural application for such a technique lies in the analysis of rare samples.

Numerous situations arise throughout analytical science in which a sample of interest is in scarce supply and must be handled efficiently. Perhaps the most striking example of

this is samples of extraterrestrial origin. The Hayabusa2 spacecraft recently accomplished the major feat of collecting dust samples from the surface of a near-earth asteroid and returning them to earth for analysis [139]. Given the small amount of material available to work with, and the enormous cost and effort required to collect it, only a scant 38 mg of dust was made available for composition analysis. This represents inordinately more sample than necessary when operating at the single molecule level, however, so that SMTS would be an invaluable tool in the analysis of such specimens. As noted in sec. 5.1, other spaceborn missions have achieved chemical analysis of other extraterrestrial bodies as well, such as the comet 67P/Churyumov-Gerasimenk [120] and Saturn's moon Titan [117]. Such analyses were performed *in situ*, but future missions may very well return such chemical samples to earth for analysis just as with Hayabusa2. If such a feat of space exploration is realized, the numerous years and billions of dollars required to do this would make these chemicals certainly the most precious ever studied. SMTS is therefore an ideal candidate for analyzing such scarce samples with maximum efficiency.

The consumption efficiency of SMTS has more immediate benefits than hypothetical space exploration missions, however. Rare elements, such as the lanthanides and actinides, exhibit exotic behavior in chemical reactions and molecular systems, which has generated significant interest in these systems in order to better understand their fundamental chemistry [160, 161]. IR vibrational spectroscopy has already been demonstrated as a valuable tool for understanding the structure of such rare element-bearing molecules, and for elucidating the unusual chemistry of these unique species [162]. Molecules containing particularly rare elements, especially those which are radioactive, are often only available in very minuscule quantities, making efficient sample consumption during analysis a necessity. SMTS is therefore ideally suited to study such systems. While rare samples occur in many different scientific contexts, these examples serve to illustrate the valuable potential for the SMTS method.

# Appendix A

# Error Analysis

## A.1 Probability Distribution

In order to compute confidence intervals for the de-tagging times which correspond to the $y$-axes of the spectra shown in ch. 5, a probability distribution must be ascribed to the de-tagging process. This is assumed to be a random process with no correlations between de-tagging events, and should therefore be well described by an exponential probability density function

$$\mathcal{P}(T,\tau) = \frac{1}{\tau(\omega_L)} e^{-T/\tau(\omega_L)} \tag{A.1}$$

where $\tau(\omega_L)$ is a distribution parameter which has units of time and which is dependent on the de-tagging laser frequency $\omega_L$. This distribution represents the probability that a tagged molecule exposed to mid-IR light starting at time $t = 0$ will scatter a photon for the first time at a time $T$. As discussed in sec. 3.1.3, a tagged molecule which scatters a mid-IR photon will de-tag on the time scale of the IVR process, usually some picoseconds. This is significantly faster than the millisecond-scale radiative lifetime for

typical vibrationally excited states. Photon scattering therefore leads to immediate de-tagging, and the probability distribution which describes the de-tagging process should be the same as that which describes the photon scattering process.

In the experiments of ch. 5, tagged molecules are exposed to a sequence of discrete pulses of IR light. The pulse which de-tags the molecule is known to start at time $t = T_i$ and end at $t = T_f$. In order to accurately evaluate the probability for such an event to occur, the probability density distribution A.1 must be integrated from $T_i$ to $T_f$. The probability that a tagged molecule will de-tag between a total IR exposure time of $T_i$ and $T_f$ is therefore

$$\begin{aligned} P(T_i, T_f) &= \int_{T_i}^{T_f} dt\mathcal{P}(t) \\ &= e^{-\frac{T_i}{\tau}} - e^{-\frac{T_f}{\tau}} \end{aligned} \tag{A.2}$$

The frequency dependence of $\tau$ will be implicit from here on. In practice, multiple measurements of the de-tagging interval $[T_i, T_f]$ are typically made to help reduce statistical noise in the measured time. Since the de-tagging process is assumed to be random and de-tagging events are uncorrelated, the probability of de-tagging a molecule in one interval $[T_{i,1}, T_{f,1}]$ followed by de-tagging in a different interval $[T_{i,2}, T_{f,2}]$ is the product of the probabilities for the two events. If $N$ total de-tagging measurements are made at a given laser frequency $\omega_L$, the probability for observing $N$ such events is therefore

$$P_N(\{T_N\} \mid \tau) = \prod_{j=1}^{N} \left[ e^{-\frac{T_{i,j}}{\tau}} - e^{-\frac{T_{f,j}}{\tau}} \right] \tag{A.3}$$

The period $\tau$ parameterizes this probability distribution, and can be viewed as the expected value for a measurement of the de-tagging time of a molecule at a given laser frequency.

## A.2 Confidence Interval Formulation

Given a set of $N$ de-tagging interval measurements, a straightforward estimate can be made of the parameter $\tau$ which makes this set of observations maximally probable. The likelihood function for the set of $N$ observations can be expressed as

$$L_N(\tau \mid \{T_N\}) = P_N(\{T_N\} \mid \tau) \tag{A.4}$$

Eq. A.4 is a function of $\tau$, and the value $\tau = \tau_0$ which maximizes this likelihood function is computed numerically. This is the value of $\tau$ which maximizes the probability of having made the set of $N$ observations, and is thus the most likely time which would be measured in a de-tagging experiment. $\tau_0$ therefore serves as the best estimate of the true value of $\tau(\omega_L)$ which characterizes the de-tagging probability distribution (eq. A.1) for a given molecule–tag combination.

All spectra reported in this work are derived using eq. A.3. $N$ de-tagging events are observed at laser frequency $\omega_L$, and the most likely value of $\tau(\omega_L) = \tau_0$ is estimated by numerically maximizing eq. A.3 with respect to $\tau$. The inverse of this $\tau_0$ estimate is then plotted versus laser frequency to present the molecule's spectrum as an equivalent de-tagging rate versus laser frequency. An example of the calculation of $\tau_0$ is illustrated in fig. A.1.

Once a maximum likelihood estimate of $\tau_0$ has been made, a confidence interval can be computed to indicate the range of values about $\tau_0$ which might parameterize the true de-tagging distribution for a given laser frequency. If $L_0$ is the maximum value of $L(\tau \mid \{T_N\})$, which occurs at $\tau = \tau_0$, then a confidence interval can be defined as the boundary values of $\tau$, $[\tau = u, \tau = v]$, inside of which $L_N > \alpha L_0$. An example of the calculation of this interval is shown in fig. A.1 with $\alpha = e^{-2}$. It should be noted that the asymmetry of the confidence intervals for the spectra reported in ch. 5 is a direct

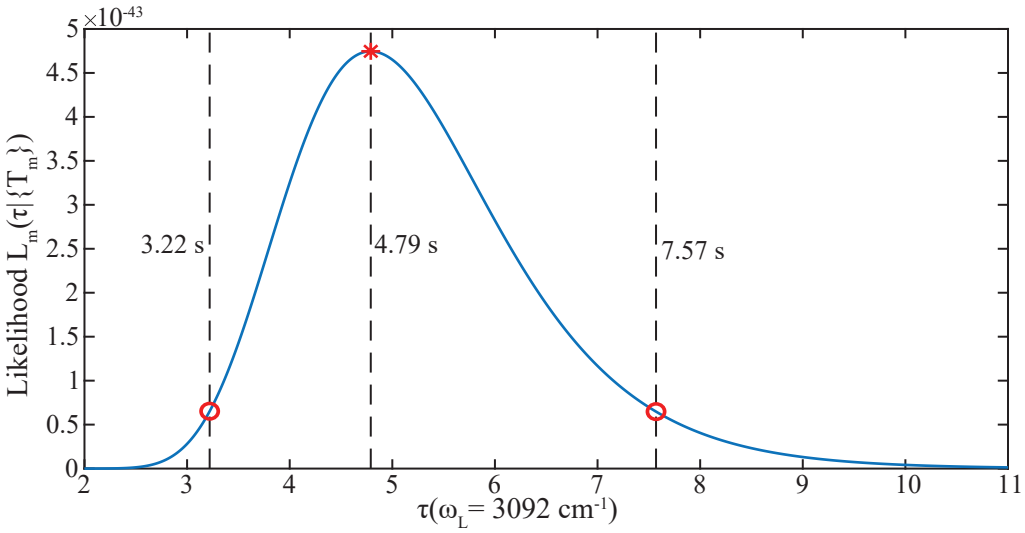


Figure A.1: An example of a maximum likelihood estimation of $\tau$ (starred point and dashed line), as well as the corresponding 95% confidence interval (circled points and dashed lines). The solid line is the probability distribution determined by eq. A.3 for $N = 22$ de-tagging observations at a laser frequency of $\omega_L = 3092$ cm$^{-1}$ for the dehydrogenated 1,3-benzodioxole fragment.

result of the asymmetry of the likelihood function with respect to $\tau$, which can be clearly observed in fig. A.1.

Prior to making any de-tagging measurements, it is assumed that $\ln(\tau)$ is a uniformly distributed random variable, that is to say, $P(\ln(\tau)) = 1$. After making a set of $N$ de-tagging measurements, the posterior probability density function given this prior assumption can be expressed as

$$\begin{aligned} P_{\ln(\tau)|\{T_m\}}(\ln(\tau)) &= \frac{P(\ln(\tau))L_m(\tau \mid \{T_m\})}{\int_{\ln(\tau)=-\infty}^{\ln(\tau)=+\infty} P(\ln(\tau))L_m(\tau \mid \{T_m\})d(\ln(\tau))} \\ &= \frac{L_m(\tau \mid \{T_m\})}{\int_{\ln(\tau)=-\infty}^{\ln(\tau)=+\infty} L_m(\tau \mid \{T_m\})d(\ln(\tau))} \end{aligned} \tag{A.5}$$

The probability that an observed value of the $\tau$ will fall in the interval $[\tau = u, \tau = v]$ is therefore the integral of this posterior probability density over this interval

$$\int_{\ln(u)}^{\ln(v)} P_{\ln(\tau)|\{T_m\}}(\ln(\tau))d(\ln(\tau)) = \frac{\int_{\ln(u)}^{\ln(v)} L_m(\tau \mid \{T_m\})d(\ln(\tau))}{\int_{-\infty}^{+\infty} L_m(\tau \mid \{T_m\})d(\ln(\tau))} = \frac{\int_u^v \frac{1}{\tau} L_m(\tau \mid \{T_m\})d\tau}{\int_0^{+\infty} \frac{1}{\tau} L_m(\tau \mid \{T_m\})d\tau} \tag{A.6}$$

In practice, it is found that choosing $\alpha = e^{-2}$ results in $P_{\ln(\tau)|\{T_m\}}(\ln(\tau)) \approx 95\%$ as calculated by eq. A.6. The vertical bars plotted with the spectra in ch. 5 were calculated according to these equations, corresponding to 95% confidence intervals for the observed spectral amplitudes.

In order to test the validity of this derived probability distribution, one may consider the probability of observing a de-tagging event in some small time interval, $[T, T + dT]$. From eq. A.1, this is simply $\mathcal{P}(T)dT$. Converting this expression from a function of $T$ to a function of $\ln(T)$

$$\mathcal{P}(\ln(T))d(\ln(T)) = P(T)dT \tag{A.7}$$

Which can be re-arranged to find the probability distribution as a function of $\ln(T)$

$$\begin{aligned} \mathcal{P}(\ln(T)) &= \frac{\mathcal{P}(T)}{\frac{d(\ln(T))}{dT}} \\ &= T\mathcal{P}(T) \\ &= \frac{T}{\tau} e^{-\frac{T}{\tau}} \\ &= e^{\ln(T/\tau)} e^{-e^{\ln(T/\tau)}} \end{aligned} \tag{A.8}$$

With the BDO-H fragment ion of sec. 5.2, a series of 22 total de-tagging measurements were made at a single, relatively off-resonance OPO frequency of 3092 $cm^{-1}$. The re-

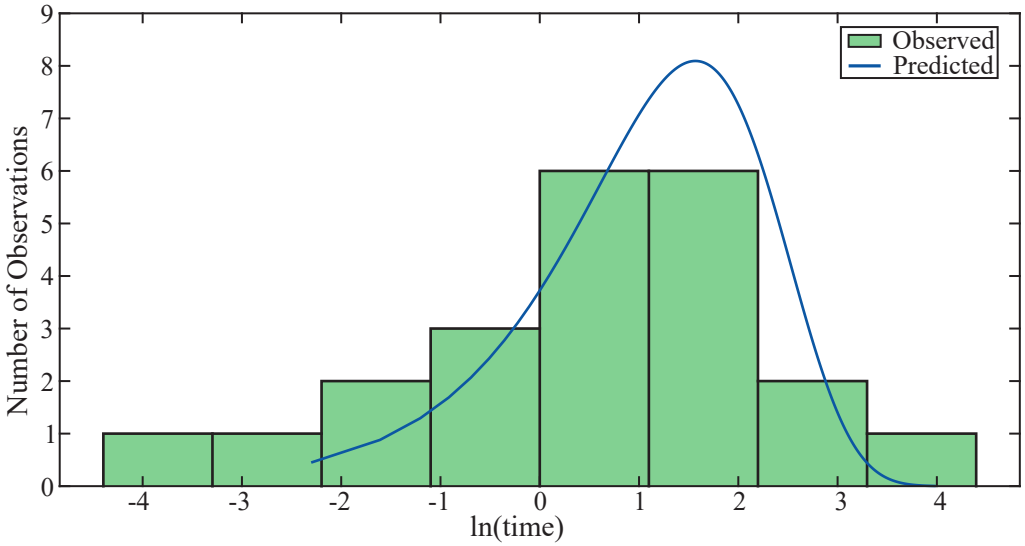


Figure A.2: Histogram of 22 observed de-tagging times for BDO-H at 3092 $cm^{-1}$, compared to the predicted distribution of times assuming the de-tagging process follows an exponential distribution.

sulting set of 22 de-tagging time intervals were inserted into eq. A.4, which was then maximized with respect to $\tau$ to determine $\tau_0$. This value of $\tau_0$ was then inserted into eq. A.8 and multiplied by $N = 22$ observations to yield the predicted distribution of logarithmic de-tagging times, given the estimated value of $\tau_0$. This predicted distribution is plotted against a histogram of observed times in fig. A.2. The two are seen to be in reasonably good agreement, supporting the underlying expectation that the de-tagging process follows an exponential probability density distribution. Additionally, the distribution observed here is not multi-modal. Such a split distribution would be expected if the tag position was not always the same in each measurement, as this variation in tag position would lead to different positions and amplitudes of observed vibrational bands. The uniformity of the observed distribution therefore demonstrates that only one tagging site occurs in this set of measurements, thus indicating that the observed features in the BDO-H spectrum arise from a single tag position.

# Appendix B

# $Tr^+$ Mode Analysis

Table B.1 summarizes all vibrational modes which have been previously observed in $Tr^+$. Modes are labelled in order of increasing frequency for simplicity.

### 2952 $cm^{-1}$ Band

Using the notation of table B.1, the $2\nu_6$ overtone has symmetry $\Gamma(E_1') \otimes \Gamma(E_1') = A_1' \oplus A_2' \oplus E_2'$. As noted in sec. 5.1, this reducible representation is not symmetry allowed (recalling that $\Gamma(\mu_{x,y}) = E_1'$ and $\Gamma(\mu_x) = A_2''$ for the $D_{7h}$ symmetry point group to which $Tr^+$ belongs). For the tagging geometry described in sec. 5.1 with the $N_2$ tag along the symmetry axis of $Tr^+$ and orthogonal to the plane of the molecule, however, the symmetry of this system is reduced from $D_{7h}$ for the bare molecule to $C_{7v}$ when tagged. The $D_{7h}$ symmetry species $E_1'$ therefore becomes $E_1$ in the $C_{7v}$ group, so that the true symmetry of the $2\nu_6$ overtone for the tagged system is $E_1 \otimes E_1 = A_1 \oplus A_2 \oplus E_2$. In the $C_{7v}$ point group, however, $\Gamma(\mu_{x,y}) = E_1$ and $\Gamma(\mu_z) = A_1$. Thus, while the first overtone of the $\nu_6$ mode is not allowed by symmetry in the bare $Tr^+$ molecule, the slight alteration to the symmetry of the system due to the presence of a tag makes this overtone IR active.

| Frequency ($cm^{-1}$) | Label | Activity | Description | Symmetry | Source |
|---|---|---|---|---|---|
| 433 | $v_1$ | Raman | Ring bending | $E_2'$ | [126] |
| 633,652 | $v_2$ | IR | C–H bending | $A_2''$ | [126, 116] |
| 868 | $v_3$ | Raman | Ring breathing | $A_1'$ | [126] |
| 992,994 | $v_4$ | IR | C–H bending | $E_1'$ | [126, 116] |
| 1210 | $v_5$ | Raman | C–H bending | $E_2'$ | [126] |
| 1477,1477,1486 | $v_6$ | IR | C–C stretch | $E_1'$ | [126, 6, 116] |
| 1594 | $v_7$ | Raman | C–C stretch | $E_2'$ | [126] |
| 3020,3036 | $v_8$ | IR | C–H stretch | $E_1'$ | [126, 6] |
| 3060 | $v_9$ | Raman | C–H stretch | $A_1'$ | [126] |
| 3075 | $v_{10}$ | Raman | C–H stretch | $E_2'$ | [126] |
| 3074,3080 | $v_{11}$ | IR | Unassigned | | [6, 126] |

Table B.1: Selected $Tr^+$ vibrational frequencies which have been reported previously. Rows with multiple frequencies listed correspond to the respective source, i.e. the first frequency in the row is reported in the first source for that row, etc.

### 3140 $cm^{-1}$ Band

Using the gas phase frequencies of ref. [116], the three component combination transition $v_2+v_4+v_6 \approx 3132\ cm^{-1}$, with symmetry $\Gamma(v_2)\otimes\Gamma(v_4)\otimes\Gamma(v_6) = A_1''\oplus A_2''\oplus E_2''$. Since $\Gamma(\mu_z) = A_2''$, this combination is IR allowed, and therefore a plausible origin for the observed weak 3140 $cm^{-1}$ band. Definitively assigning this band is challenging, however. A number of different combinations can be made of known IR and/or Raman active modes which sum to approximately the correct frequency and which are allowed by symmetry. For example, $Tr^+$ is predicted to have a vibrational mode with $E_3'$ symmetry which is neither IR nor Raman active [126]. This mode can become IR active in combination with observed Raman modes $v_1$ and $v_5$, however $(E_3'\otimes\Gamma(v_1)\otimes\Gamma(v_5) = A_1'\oplus A_2'\oplus E_1'\oplus 2E_3')$. The frequency of this silent mode has been predicted to be 1511 $cm^{-1}$ (see supplementary information for ref. [163]). If this is correct, the frequency of this three component combination ($\approx$3154 $cm^{-1}$) is very similar to that of the observed weak band. One may argue that this three component combination band is less probable than the one cited above, since transition matrix elements for Raman transitions are general much smaller

than for IR allowed transitions. The level of uncertainty involved here is large enough that only suggested assignments can be made.

### 3065 and 3077 $cm^{-1}$ Bands

It must also be noted that two relatively strong Raman bands ($v_9$ and $v_{10}$ in table B.1) have been reported in the vicinity of the 3065 and 3077 $cm^{-1}$ peaks observed in this work [126]. The assignment of the symmetry and frequency of these modes has been supported by theoretical treatments of the vibrational structure of $Tr^+$ as well (ref. [163] supplementary information). The reduction in symmetry from the $D_{7h}$ point group to the $C_{7v}$ point group transforms the irreducible representation $A_1' \rightarrow A_1$. This result is significant, however, as $\Gamma(\mu_z) = A_1$ in the $C_{7v}$ group. The Raman mode $v_9$ may potentially become IR allowed due to this reduction in the overall symmetry of the tagged system. This is consistent with the results reported in ref. [126], in which $Tr^+$ spectra were recorded in solution. A weak band was observed here centered near $\sim$3080 $cm^{-1}$ which was not assigned. Symmetry disallowed vibrations are known to appear in solution phase vibrational spectra, however, due to instantaneous anisotropy in the analyte molecule's liquid environment [128], suggesting that this observed IR band may indeed be a Raman vibration made IR active due to symmetry breaking. A similar result does not hold true for mode $v_{10}$, however, as $E_2'$ in the $D_{7h}$ group transforms to $E_2 \neq \Gamma(\mu_{x,y,z})$. Further analysis is therefore needed to definitively assign the 3074 $cm^{-1}$ and 3140 $cm^{-1}$ bands observed in this work.

# Bibliography


[1] R. March and J. Todd, *Quadrupole Ion Trap Mass Spectrometry*. John Wiley and Sons, 2005.

[2] B. E. King, *Quantum State Engineering and Information Processing with Trapped Ions*. PhD thesis, University of Colorado, Boulder, Boulder, Colorado, 1999.

[3] P. Richerme, *Depletion, Quantum Jumps, and Temperature Measurements of $^{88}Sr^{+}$ Ions in a Linear Paul Trap*. PhD thesis, Massachusetts Institute of Technology, Cambridge, Massachusetts, 2006.

[4] L. Woodward, *Introduction to the Theory of Molecular Vibrations and Vibrational Spectroscopy*. Oxford University Press, 1972.

[5] E. B. W. Jr., J. C. Decius, and P. C. Cross, *Molecular Vibrations*. McGraw-Hill, 1955.

[6] J. Wagner, D. McDonald II, and M. Duncan, *Mid-infrared spectroscopy of $C_7H_7^+$ isomers in the gas phase: Benzylium and tropylium*, *J. Phys. Chem. Lett.* **9** (2018) 4591–4595.

[7] S. Brewer, J. Chen, A. Hankin, E. Clements, C. Chou, D. Wineland, D. Hume, and D. Leibrandt, *$^{27}Al^{+}$ quantum-logic clock with a systematic uncertainty below $10^{-18}$*, *Phys. Rev. Lett.* **123** (2019) 033201.

[8] M. Drewsen, *Ion coulomb crystals*, *Physica B* **460** (2015) 105–113.

[9] A. T. Calvin and K. R. Brown, *Spectroscopy of molecular ions in Coulomb crystals*, *The Journal of Physical Chemistry Letters* **9** (Oct, 2018) 5797–5804.

[10] S. Willitsch, *Coulomb-crystallised molecular ions in traps: Methods, applications, prospects*, *Int. Rev. Phys. Chem.* **31** (2012) 175–199.

[11] D. Douglas, A. Frank, and D. Mao, *Linear ion traps in mass spectrometry*, *Mass Spectrom. Rev.* **24** (2004) 1–29.

[12] J. Campbell, B. Collings, and D. Douglas, *A new linear ion trap time-of-flight system with tandem mass spectrometry capabilities*, *Rapid Commun. Mass. Spectrom.* **12** (1998) 1463–1474.

[13] S. Earnshaw, *On the nature of the molecular forces which regulate the constitution of the luminiferous ether*, *Trans. Camb. Phil. Soc.* **7** (1842) 97–112.

[14] W. Paul and H. Steinwedel, *Notizen: Ein neues massenspektrometer ohne magnetfeld*, *Z. Naturforsch. A* **8** (1953) 448–450.

[15] N. McLachlan, *Theory and Application of Mathieu Functions*. Oxford Press, 1947.

[16] J. Heinrich, *A $Be^+$ Ion Trap for $H_2^+$ Spectroscopy*. PhD thesis, Sorbonne Université, Paris, France, 2018.

[17] P. L. Kapitza, *Dynamic stability of the pendulum with vibrating suspension point*, *Sov. Phys. JETP* **21** (1951) 588–597.

[18] D. Berkeland, J. Miller, J. Bergquist, W. Itano, and D. Wineland, *Minimization of ion micromotion in a paul trap*, *J. Appl. Phys.* **83** (1998) 5025–5033.

[19] G. Morigi and H. Walther, *Two-species coulomb chains for quantum information*, *Eur. Phys. J. D* **13** (2001) 261–269.

[20] M. Fan, C. Holliman, X. Shi, H. Zhang, M. Straus, X. Li, S. Buechele, and A. Jayich, *Optical mass spectrometry of cold $RaOH^+$ and $RaOCH_3^+$*, *Phys. Rev. Lett.* **126** (2021) 023002.

[21] D. Wineland, R. Drullinger, and F. Walls, *Radiation-pressure cooling of bound resonant absorbers*, *Phys. Rev. Lett.* **40** (1978) 1639–1642.

[22] C. Foot, *Atomic Physics*. Oxford University Press, 2005.

[23] R. Drullinger, D. Wineland, and J. Bergquist, *High-resolution optical spectra of laser cooled ions*, *Appl. Phys.* **22** (1980) 365–368.

[24] D. Larson, J. Bergquist, W. Itano, and D. Wineland, *Sympathetic cooling of trapped ions: A laser-cooled two-species nonneutral ion plasma*, *Phys. Rev. Lett.* **57** (1986) 70–73.

[25] Z. Mao, Q. Mei, W. Zhao, Y. Jiang, Y. Wang, X. Chang, L. He, L. Yao, Z. Zhou, Y. Wu, and L. Duan, *Experimental realization of multi-ion sympathetic cooling on a trapped ion crystal*, *Phys. Rev. Lett.* **127** (2021) 143201.

[26] P. Bowe, C. B. L. Hornekær, M. Drewsen, J. Hangst, and J. Schiffer, *Sympathetic crystallization of trapped ions*, *Phys. Rev. Lett.* **82** (1999) 2071–2074.

[27] T. Baba and I. Waki, *Cooling and mass-analysis of molecules using laser-cooled atoms*, *Jpn. J. Appl. Phys.* **35** (1996) L1134–L1137.

[28] A. Ostendorf, C. Zhang, M. Wilson, D. Offenberg, B. Roth, and S. Schiller, *Sympathetic cooling of complex molecular ions to millikelvin temperatures*, *Phys. Rev. Lett.* **97** (2006) 243005.

[29] M. Bohman, V. Grunhofer, C. Smorra, M. Wiesinger, C. Will, M. Borchert, J. Devlin, S. Erlewein, M. Fleck, and S. Gavronovic, *et al.*, *Sympathetic cooling of a trapped proton mediated by an LC circuit*, *Nature* **596** (2021) 514–518.

[30] C. Baker, W. Bertsche, C. Cesar, M. Charlton, A. C. Mathad, S. Eriksson, A. Evans, N. Evetts, S. Fabbri, and J. Fajans, *et al.*, *Sympathetic cooling of positrons to cryogenic temperatures for antihydrogen production*, *Nature Comm.* **12** (2021) 6139.

[31] P. Bowe, L. Hornekær, C. Brodersen, M. Drewsen, and J. Hangst, *Sympathetic crystallization of trapped ions*, *Phys. Rev. Lett.* **82** (1999) 2071–2074.

[32] D. Offenberg, C. Zhang, C. Wellers, B. Roth, and S. Schiller, *Translation cooling and storage of protonated proteins in an ion trap at subkelvin temperatures*, *Phys. Rev. A* **78** (2008) 061401(R).

[33] A. Bertelsen, S. J. rgensen, and M. Drewsen, *The rotational temperature of polar molecular ions in coulomb crystals*, *J. Phys. B: At. Mol. Opt. Phys.* **39** (2006) L83–L89.

[34] J. Sansonetti, *Wavelengths, transition probabilities, and energy levels for the spectra of strontium ions (Sr II through Sr XXXVIII)*, *J. Phys. Chem. Ref. Data* **41** (2012) 013102.

[35] A. Gallagher, *Oscillator strengths of Ca II, Sr II, and Ba II*, *Phys. Rev.* **157** (1967) 24–30.

[36] S. Mannervik, J. Lidberg, L.-O. Norlin, P. Royen, A. Schmitt, W. Shi, and X. Tordoir, *Lifetime measurment of the metastable $4d^2D_{3/2}$ level in $Sr^+$ by optical pumping of a stored ion beam*, *Phys. Rev. Lett.* **83** (1999) 698–701.

[37] A. Leandhardt, T. Pasquini, M. Saba, A. Schirotzek, Y. Shin, D. Kielpinski, D. Pritchard, and W. Ketterle, *Cooling Bose-Einstein condensates below 500 picokelvin*, *Science* **301** (2003) 1513–1515.

[38] J. Doyle, B. Friedrich, J. Kim, and D. Patterson, *Buffer-gas loading of atoms and molecules into a magnetic trap*, *Phys. Rev. A* **52** (1995) R2515–R2518.

[39] B. Hemmerling, G. Drayna, E. Chae, A. Ravi, and J. Doyle, *Buffer gas loaded magneto-optical traps for Yb, Tm, Er and Ho*, *New J. Phys.* **16** (2014) 063070.

[40] J. Kim, B. Friedrich, D. Katz, D. Patterson, J. Weinstein, R. DeCarvalho, and J. Doyle, *Buffer-gas loading and magnetic trapping of atomic europium*, *Phys. Rev. Lett.* **78** (1997) 3665–3668.

[41] A. Grier, M. Cetina, F. Oručević, and V. Vuletić, *Observation of cold collisions between trapped ions and trapped atoms*, *Phys. Rev. Lett.* **102** (2009) 223201.

[42] G. Gioumousis and D. Stevenson, *Reactions of gaseous molecule ions with gaseous molecules. V. theory*, *J. Chem. Phys.* **29** (1958) 294–299.

[43] M. Langevin, *A fundamental formula of kinetic theory*, *Ann. Chim. Phys.* **5** (1905) 245–288.

[44] R. Wester, *Radiofrequency multipole traps: Tools for spectroscopy and dynamics of cold molecular ions*, *J. Phys. B: At. Mol. Opt. Phys.* **42** (2009) 154001.

[45] M. Masili and A. Starace, *Static and dynamic dipole polarizability of the helium atom using wave functions involving logarithmic terms*, *Phys. Rev. A* **68** (2003) 012508.

[46] P. Taylor, T. Lee, J. Rice, and J. Almlöf, *The polarizabilities of neon*, *Chem. Phys. Lett.* **163** (1989) 359–365.

[47] S. Rice, *Selectivity of elementary molecular processes associated with energy transfer and chemical reaction*, *J. Phys. Chem* **90** (1986) 3063–3072.

[48] C. Markus, O. Asvany, T. Salomon, P. Schmid, S. Bünken, F. Lipparini, J. Gauss, and S. Schlemmer, *Vibrational excitation hindering an ion-molecule reaction: The c-$C_3H_2^+$–$H_2$ collision complex*, *Phys. Rev. Lett.* **124** (2020) 233401.

[49] A. Hansen, O. Versolato, Ł. Kłosowski, S. Kristensen, A. Gingell, M. Schwartz, A. Windberger, J. Ulrich, J. Crespo-López-Urrutia, and M. Drewsen, *Efficient rotational cooling of Coulomb-crystallized molecular ions by a helium buffer gas*, *Nature* **508** (2014) 76–79.

[50] D. Yang, J. Huang, X. Hu, H. Guo, and D. Xie, *Breakdown of energy transfer gap laws revealed by full-dimensional quantum scattering between HF molecules*, *Nature Comm.* **10** (2019) 4658.

[51] R. deCarvalho, J. Doyle, B. Friedrich, T. Guillet, J. Kim, D. Patterson, and J. Weinstein, *Buffer-gas loaded magnetic traps for atoms and molecules: A primer*, *Eur. Phys. J. D* **7** (1999) 289–309.

[52] Y. Zhang, D. Zhang, J. Wu, Z. He, and X. Deng, *A thermal model for nanosecond pulsed laser ablation of aluminum*, *AIP Adv.* **7** (2017) 075010.

[53] M. Weissbluth, *Atoms and Molecules*. Academic Press, 1978.

[54] T. Uzer and W. Miller, *Theories of intramolecular vibrational energy transfer*, *Phys. Rep.* **199** (1991) 73–146.

[55] K. von Puttkamer, H. Dübal, and M. Quack, *Time-dependent processes in polyatomic molecules during and after intense infrared irradiation*, *Faraday Discuss.* **75** (1983) 197–210.

[56] J. Butler and G. Kistiakoswky, *Reactions of methylene. IV. Propylene and cyclopropane*, *J. Am. Chem. Soc.* **82** (1960) 759–765.

[57] D. Nesbitt and R. Field, *Vibrational energy flow in highly excited molecules: Role of intramolecular vibrational redistribution*, *J. Phys. Chem.* **100** (1996) 12735–12756.

[58] G. Bethardy, X. Wang, and D. Perry, *The role of molecular flexibility in accelerating intramolecular vibrational relaxation*, *Can. J. Chem.* **72** (1994) 652–659.

[59] L. Giancarlo and M. Lester, *Vibrational predissociation and electronic quenching dynamics of OH-$N_2$ ($A^2\Sigma^+$)*, *Chem. Phys. Lett.* **240** (1995) 1–9.

[60] S. Stein, *NIST 35. NIST/EPA gas-phase infrared database - JCAMP format*, *World Wide Web-Internet and Web Information Systems* (2008).

[61] B. Stuart, *Infrared Spectroscopy: Fundamentals and Applications*. John Wiley Sons, Ltd, 2004.

[62] J. Steinfeld, *Molecules and Radiation*. MIT Press, 1974.

[63] M. Waegele, R. Culik, and F. Gai, *Site-specific spectroscopic reporters of the local electric field, hydration, structure, and dynamics of biomolecules*, *J. Phys. Chem. Lett.* **2** (2011) 2598–2609.

[64] K. Rector and M. Fayer, *Vibrational echoes: A new approach to condensed-matter vibrational spectroscopy*, *Int. Rev. Phys. Chem.* **17** (1998) 261–306.

[65] A. El-Aneed, A. Cohen, and J. Banoub, *Mass spectrometry, review of the basics: Electrospray, MALDI, and commonly used mass analyzers*, *Appl. Spectrosc. Rev.* **44** (2009) 210–230.

[66] C. Stedwell, J. Galindo, A. Roitberg, and N. Polfer, *Structures of biomolecular ions in the gas phase probed by infrared light sources*, *Annu. Rev. Anal. Chem.* **6** (2013) 267–285.

[67] F. Arnold, *Atmospheric ions and aerosol formation*, *Space Sci. Rev.* **137** (2008) 225–239.

[68] A. Hirsikko, T. Nieminen, S. Gagné, K. Lehtipalo, H. Manninen, M. Ehn, U. Hõrrak, V.-M. Kerminen, L. Laakso, and P. McMurry, *et al.*, *Atmospheric ions and nucleation: A review of observations*, *Atmos. Chem. Phys.* **11** (2011) 767–798.

[69] C. Anderson and M. Record Jr., *Ion distributions around DNA and other cylindrical polyions: Theoretical descriptions and physical implications*, *Annu. Rev. Biophys. Biophys. Chem.* **19** (1990) 423–465.

[70] C. Miller, *An overview of the potassium channel family*, *Genome Biol.* **1** (2000) reviews0004.1.

[71] Z. Tian and S. Kass, *Does electrospray ionization produce gas-phase or liquid-phase structures?*, *J. Am. Chem. Soc.* **130** (2008) 10842–10843.

[72] M. Gerin, H. Liszt, D. Neufield, B. Godard, P. Sonnentrucker, J. Pety, and E. Roueff, *Molecular ion abundances in the diffuse ISM: $CF^+$, $HCO^+$, $HOC^+$, and $C_3H^+$*, *Astron. Astrophys.* **622** (2018) A26.

[73] E. Herbst, *Molecular ions in interstellar reaction networks*, *J. Phys.: Conf. Ser.* **4** (2005) 17–25.

[74] N. Indriolo and B. McCall, *Cosmic-ray astrochemistry*, *Chem. Soc. Rev.* **42** (2013) 7763–7773.

[75] N. Polfer, *Infrared multiple photon dissociation spectroscopy of trapped ions*, *Chem. Soc. Rev.* **40** (2011) 2211–2221.

[76] A. P. Cismesia, M. R. Bell, L. F. Tesler, M. Alves, and N. C. Polfer, *Infrared ion spectroscopy: An analytical tool for the study of metabolites*, *Analyst* **143** (2018) 1615–1623.

[77] A. Cismesia, L. Tesler, M. Bell, L. Bailey, and N. Polfer, *Infrared ion spectroscopy inside a mass-selective 2D linear ion trap*, *J. Mass Spectrom.* **52** (2017) 720–727.

[78] X. Li, J. Oomens, J. Eyler, D. Moore, and S. Iyengar, *Isotope dependent, temperature regulated, energy repartitioning in a low-barrier, short-strong hydrogen bonded cluster*, *J. Chem. Phys.* **132** (2010) 244301.

[79] N. Polfer and P. Dugourd, eds., *Laser Photodissociation and Spectroscopy of Mass-Separated Biomolecular Ions*, vol. 83 of *Lecture Notes in Chemistry*. Springer Cham., 2013.

[80] M. Okumura, L. I. Yeh, and Y. T. Lee, *The vibrational predissociation spectroscopy of hydrogen cluster ions*, *J. Chem. Phys.* **83** (1985) 3705–3706.

[81] A. Wolk, C. Leavitt, E. Garand, and M. Johnson, *Cryogenic ion chemistry and spectroscopy*, *Acc. Chem. Res.* **47** (2013) 202–210.

[82] M. Kamrath, R. Relph, T. Guasco, C. Leavitt, and M. Johnson, *Vibrational predissociation spectroscopy of the $H_2$-tagged mono- and dicarboxylate anions of dodecanedioic acid*, *Int. J. Mass Spec.* **300** (2011) 91–98.

[83] K. Geistlinger, F. Dahlmann, T. Michaelsen, M. Ončák, and E. Endres, *Multiple helium tagging and OH vibrational spectroscopy of cold protonated glycine ions*, *J. Mol. Spec.* **379** (2021) 111479.

[84] M. Kamrath, E. Garand, P. Jordan, C. Leavitt, A. Wolk, M. V. Stipdonk, S. Miller, and M. Johnson, *Vibrational characterization of simple peptides using cryogenic infrared photodissociation of $H_2$-tagged, mass-selected ions*, *J. Am. Chem. Soc.* **133** (2011) 6440–6448.

[85] W. Robertson, J. Kelley, and M. Johnson, *A pulsed supersonic entrainment reactor for the rational preparation of cold ionic complexes*, *Rev. Sci. Instrum.* **71** (2000) 4431–4434.

[86] R. Laine, *Invited Commentary: A calculation of all possible oligosaccharide isomers both branched and linear yields* $1.05 \times 10^{12}$ *structures for a reducing hexasaccharide: The Isomer Barrier to development of single-method saccharide sequencing or synthesis systems*, *Glycobiology* **4** (1994) 759–767.

[87] O. Boyarkin, S. Mercier, A. Kamariotis, and T. Rizzo, *Electronic spectroscopy of cold, protonated tryptophan and tyrosine*, *J. Am. Chem. Soc.* **128** (2006) 2816–2817.

[88] N. Polfer and J. Oomens, *Vibrational spectroscopy of bare and solvated ionic complexes of biological relevance*, *Mass Spectrom. Rev.* **28** (2009) 468–494.

[89] T. Rizzo, J. Stearns, and O. Boyarkin, *Spectroscopic studies of cold, gas-phase biomolecular ions*, *Int. Rev. Phys. Chem.* **28** (2009) 481–515.

[90] C. Johnson, A. Wolk, J. Fournier, G. Sullivan, G. Weddle, and M. Johnson, *Communication: He-tagged vibrational spectra of the SarGlyH$^+$ and $H^+(H_2O_3)_{2,3}$ ions: Quantifying tag effects in cryogenic ion vibrational predissociation (CIVP) spectroscopy*, *J. Chem. Phys.* **140** (2014) 221101.

[91] W. Kolos and L. Wolniewicz, *Polarizability of the hydrogen molecule*, *J. Chem. Phys.* **46** (1967) 1426–1432.

[92] J. Wagner, S. Giles, and M. Duncan, *Gas phase infrared spectroscopy of the $H_2C{=}NH_2^+$ methaniminium cation*, *Chem. Phys. Lett.* **726** (2019) 53–56.

[93] M. Duncan, *Infrared spectroscopy to probe structure and dynamics in metal ion-molecule complexes*, *Int. Rev. in Phys. Chem.* **22** (2003) 407–435.

[94] J. Mosley, J. Young, and M. Duncan, *Infrared spectroscopy of the acetyl cation and its protonated ketene isomer*, *J. Chem. Phys.* **141** (2014) 024306.

[95] S. Hoekstra, J. Gilijamse, B. Sartakov, N. Vanhaecke, L. Scharfenberg, S. van de Meerakker, and G. Meijer, *Optical pumping of trapped neutral molecules by blackbody radiation*, *Phys. Rev. Lett* **98** (2007) 133001.

[96] J. Koelemeij, B. Roth, and S. Schiller, *Blackbody thermometry with cold molecular ions and application to ion-based frequency standards*, *Phys. Rev. A* **76** (2007) 023413.

[97] K. Okada, M. Wada, T. Takayanagi, S. Ohtani, and H. Schuessler, *Characterization of ion coulomb crystals in a linear paul trap*, *Phys. Rev. A* **81** (2010) 013420.

[98] Y. Aikyo, G. Vrijsen, T. Noel, A. Kato, M. K. Ivory, and J. Kim, *Vacuum characterization of a compact room-temperature trapped ion system*, *Appl. Phys. Lett.* **117** (2020) 234002.

[99] R. Berman and E. Foster, *Thermal conduction in artificial sapphire crystals at low temperatures*, *Proc. R. Soc. A* **231** (1955) 130–144.

[100] E. Grilly, *The vapor pressures of hydrogen, deuterium and tritium up to three atmospheres*, *J. Am. Chem. Soc.* **73** (1951) 843–846.

[101] D. Stull, *Vapor pressure of pure substances. Organic and inorganic compounds*, *Ind. Eng. Chem.* **39** (1947) 517–540.

[102] E. K. Campbell, M. Holz, D. Gerlich, and J. P. Maier, *Laboratory confirmation of $C_{60}^+$ as the carrier of two diffuse interstellar bands*, *Nature* **523** (2015) 322–323.

[103] D. Zeh, M. Bast, D. Rap, P. Scmid, S. Thorwith, S. Brünken, S. Schlemmer, and M. Schäfer, *Cryogenic messenger-IR ion spectroscopy study of phenol & aniline molecular ions and of the common fragment ion $[C_5H_6]^{\bullet +}$ formed by EI-MS*, *J. Mol. Spec.* **378** (2021) 111453.

[104] D. Rap, T. van Boxtel, B. Redlich, and S. Brünken, *Spectroscopic detection of cyano-cyclopentadiene ions as dissociation products upon ionization of aniline*, *J. Phys. Chem. A* **126** (2022) 2989–2997.

[105] T. Olney, N. Cann, G. Cooper, and C. Brion, *Absolute scale determination for photoabsorption spectra and the calculation of molecular properties using dipole sum-rules*, *Chem. Phys.* **223** (1997) 59–98.

[106] H. Michaelson, *The work function of the elements and its periodicity*, *J. Appl. Phys. B* **48** (1977) 4729–4733.

[107] M. Brownnutt, V. Letchumanan, G. Wilpers, R. Thompson, P. Gill, and A. Sinclair, *Controlled photoionization loading of $^{88}Sr^{+}$ for precision ion-trap experiments*, *Appl. Phys. B* **87** (2007) 411–415.

[108] A. Sinclair, M. Wilson, and P. Gill, *Improved three-dimensional control of a single strontium ion in an endcap trap*, *Opt. Commun.* **190** (2001) 193–203.

[109] T. Baba and I. Waki, *Cooling and mass-analysis of molecules using laser-cooled atoms*, *Jpn. J. Appl. Phys.* **35** (1996) L1134–L1137.

[110] M. Drewsen, A. Mortensen, R. Martinussen, P. Staanum, and J. Sørensen, *Nondestructive identification of cold and extremely localized single molecular ions*, *Phys. Rev. Lett.* **93** (2004) 243201.

[111] S. Willitsch, M. Bell, A. Gingell, S. Procter, and T. Softley, *Cold reactive collisions between laser-cooled ions and velocity-selected neutral molecules*, *Phys. Rev. Lett.* **100** (2008) 043203.

[112] G. Merling, *Ueber tropin*, *Berichte der deutschen chemischen Gesellschaft* **24** (1891) 3108–3126.

[113] P. Rylander, S. Meyereson, and H. Grubb, *Organic ions in the gas phase. II. The tropylium ion*, *J. Am. Chem. Soc.* **79** (1957) 842–846.

[114] P. Ausloos, *Structure and isomerization of $C_7H_7^+$ ions formed in the charge-transfer-induced fragmentation of ethylbenzene, toluene, and norbornadiene*, *J. Am. Chem. Soc.* **104** (1982) 5259–5265.

[115] C. Lifshitz, *Tropylium ion formation from toluene: Solution of an old problem in organic mass spectrometry*, *Acc. Chem. Res.* **27** (1994) 138–144.

[116] P. Jusko, A. Simon, S. Banhatti, S. Brünken, and C. Joblin, *Direct evidence of the benzylium and tropylium cations as the two long-lived isomers of $C_7H_7^+$*, *ChemPhysChem* **19** (2018) 3182–3185.

[117] J. Waite, D. Young, T. Cravens, A. Coates, F. Crary, B. Magee, and J. Westlake, *The process of tholin formation in titan's upper atmosphere*, *Science* **316** (2007) 870–875.

[118] J. Loison, M. Dobrijevic, and K. Hickson, *The photochemical production of aromatics in the atmospher of titan*, *Icarus* **329** (2019) 55–71.

[119] M. Schumann, K. Altwegg, H. Balsiger, J. Berthelier, J. D. Keyser, B. Fiethe, S. Fuselier, S. Gasc, T. Gombosi, and N. Hänni, *et al.*, *Aliphatic and aromatic hydrocarbons in comet 67P/Churyumov-Gerasimenko seen by ROSINA*, *Astron. Astrophys.* **630** (2019) A31.

[120] K. Altwegg, H. Balsiger, J. Berthelier, A. Bieler, U. Calmonte, S. Fuselier, F. Goesmann, S. Gasc, T. Gombosi, and L. Le Roy, *et al.*, *Organics in comet 67P - A first comparative analysis of mass spectra from ROSINA-DFMS, COSAC and Ptolemy*, *Mon. Notices Royal Astron. Soc.* **469** (2017) S130–S141.

[121] A. Tielens, *Interstellar polycyclic aromatic hydrocarbon molecules*, *Annu. Rev. Astron. Astrophys.* **46** (2008) 289–337.

[122] C. Joblin, A. Tielens, L. Allamandola, and T. Geballe, *Spatial variation of the 3.29 and 3.40 micron emission bands within reflection nebulae and the photochemical evolution of methylated polycyclic aromatic hydrocarbons*, *Astrophys. J.* **458** (1996) 610–620.

[123] G. Wenzel, A. Simon, S. Banhatti, P. Jusko, S. Schlemmer, S. Brünken, and C. Joblin, *Infrared spectroscopy of the benzylium-like (and tropylium-like) isomers formed in the -H dissociative ionization of methylated PAHs*, *J. Mol. Spec.* **385** (2022) 111620.

[124] M. Rapacioli, A. Simon, C. Marshall, J. Cuny, D. Kokkin, F. Spiegelman, and C. Joblin, *Cationic methylene-pyrene isomers and isomerization pathways: Finite temperature theoretical studies*, *J. Phys. Chem. A* **119** (2015) 12845–12854.

[125] M. Frisch, G. Trucks, H. Schlegel, G. Scuseria, M. Robb, J. Cheeseman, G. Scalmani, V. Barone, G. Petersson, and H. Nakatsuji, *et al.*, *Gaussian16 Revision C.01*, 2016. Gaussian Inc. Wallingford CT.

[126] W. Fateley and E. Lippincott, *Vibrational spectrum and structure of the tropylium ion*, *J. Chem. Phys.* **26** (1957) 1471–1481.

[127] G. Fèraud, C. Dedonder-Lardeux, S. Soorkia, and C. Jouvet, *Photo-fragmentation spectroscopy of benzylium and 1-phenylethyl cations*, *The Journal of Chemical Physics* **140** (2014) 024302.

[128] E. B. Wilson Jr., J. C. Decius, and P. C. Cross, *Molecular Vibrations*, p. 146. McGraw-Hill, 1955.

[129] N. Micale, M. Zappalá, and S. Grasso, *Synthesis and antitumor activity of 1,3-benzodioxole derivatives*, *Farmaco* **57** (2002) 853–859.

[130] S. Moon, Y. Kwon, J. Lee, and J. Choo, *Conformational stabilization of 1,3-Benzodioxole: Anomeric effect by natural bond orbital analysis*, *J. Phys. Chem. A* **105** (2001) 3221–3225.

[131] K. Hassan and J. Hollas, *Supersonic jet fluorescence spectroscopy of 1,3-benzodioxole: a non-planar ($C_2$) structure in $S_0$*, *Chem. Phys. Lett.* **157** (1989) 183–188.

[132] S. Sakurai, N. Meinander, K. Morris, and J. Laane, *Far-infrared, Raman, and dispersed fluorescence spectra, vibrational potential energy surface, and the anomeric effect of 1,3-benzodioxole*, *J. Am. Chem. Soc.* **121** (1999) 5056–5062.

[133] J. Laane, E. Bondoc, S. Sakurai, K. Morris, N. Meinander, and J. Choo, *Spectroscopic determination of the vibrational potential energy surface and conformation of 1,3-benzodioxole in its $S_1(\pi,\pi^*)$ excited state. the effect of the electronic excitation on the anomeric effect*, *J. Am. Chem. Soc.* **122** (2000) 2628–2634.

[134] J. Duckett, T. Smithson, and H. Wieser, *1,3-benzodioxole: Far-infrared spectrum 50-500 $cm^{-1}$*, *Chem. Phys. Lett.* **64** (1979) 261–265.

[135] J.-H. Lee and J. Lee, *Indole as an intercellular signal in microbial communities*, *FEMS Microbiol. Rev.* **34** (2010) 426–444.

[136] C. Chimerel, E. Emery, D. Summers, U. Keyser, F. Gribble, and F. Reimann, *Bacterial metabolite indole modulates incretin secretion from intestinal enteroendocrine L cells*, *Cell Rep.* **9** (2014) 1202–1208.

[137] N. Kaushik, N. Kaushik, P. Attri, N. Kumar, C. Kim, A. Verma, and E. Choi, *Biomedical importance of indoles*, *Molecules* **18** (2013) 6620–6662.

[138] H. Naraoka and M. Hashiguchi, *Distinct distribution of soluble N-heterocyclic compounds between CM and CR chondrites*, *Geochem. J.* **53** (2018) 33–40.

[139] H. Naraoka, Y. Takano, J. Dworkin, Y. Oba, K. Hamase, N. Ogawa, M. Hashiguchi, K. Fukushima, D. Aoki, and P. Schmitt-Koplin, *et al.*, *Soluble organic molecules in samples of the carbonaceous asteroid (162173) ryugu*, *Science* **379** (2023) eabn9033.

[140] K. Vávra, K. Luková, P. Kania, J. Koucký, and Š. Urban, *Rotational spectra of indole in the lowest vibrational states*, *J. Mol. Spec.* **363** (2019) 111175.

[141] N. Solcà and O. Dopfer, *Microsolvation of the indole cation ($In^+$) in a nonpolar environment: IR spectra of $In^+$-$L_n$ complexes (L = Ar and $N_2$, n8)*, *Phys. Chem. Chem. Phys.* **6** (2004) 2732–2741.

[142] N. Chalyavi, K. Catani, J. Sanelli, V. Dryza, and E. Bieske, *Gas-phase electronic spectrum of the indole radical cation*, *Mol. Phys.* **113** (2014) 2086–2094.

[143] D. Garay-Ruiz, M. Álvarez Moreno, C. Bo, and E. Martinez-Núñez, *New tools for taming complex reaction networks: The unimolecular decomposition of indole revisited*, *ACS Phys. Chem. Au* **2** (2022) 225–236.

[144] J.-C. Loison, V. Wakelam, and K. Hickson, *The insterstellar gas-phase chemistry of HCN and HNC*, *Mon. Notices Royal Astron. Soc.* **443** (2014) 398–410.

[145] D. Fouque, A. Maroto, and A. Memboeuf, *Purification and quantification of an isomeric compound in a mixture by collisional excitation in multistage mass spectrometry experiments*, *Anal. Chem.* **88** (2016) 10821–10825.

[146] S. McPherson, J. Shusterman, H. L. Peña, D. Boateng, and K. Tibbetts, *Quantitative analysis of nitrotoluene isomer mixtures using femtosecond time-resolve mass spectrometry*, *Anal. Chem.* **93** (2021) 11268–11274.

[147] A. Abikhodr, V. Yatsyna, A. B. Faleh, S. Warnke, and T. Rizzo, *Identifying mixtures of isomeric human milk oligosaccharides by the decomposition of IR spectral fingerprints*, *Anal. Chem.* **93** (2021) 14730–14736.

[148] J. Martens, G. Berden, R. van Outersterp, L. Kluijtmans, U. Engelke, C. van Karnebeek, R. Wevers, and J. Oomens, *Molecular identification in metablomics using infrared ion spectroscopy*, *Sci. Rep.* **7** (2017) 3363.

[149] V. Yatsyna, A. Abikhodr, A. Faleh, S. Warnke, and T. Rizzo, *High-throughput multiplexed infrared spectroscopy of ion mobility-separated species using hadamard transform*, *Analytical Chemistry* **94** (2022) 2912–2917.

[150] B. Elliott, R. Relph, J. Roscioli, J. Bopp, G. Gardenier, T. Guasco, and M. Johnson, *Isolating the spectra of cluster ion isomers using Ar-"tag"-mediated IR-IR double resonance within the vibrational manifolds: Application to $N_2O^-{\cdot}H_2O$*, *J. Chem. Phys.* **129** (2008) 094303.

[151] C. Leavitt, A. Wolk, J. Fournier, M. Kamrath, E. Garand, M. V. Stipdonk, and M. Johnson, *Isomer-specific IR-IR double resonance spectroscopy of $D_2$-tagged protonated dipeptides prepared in a cryogenic ion trap*, *J. Phys. Chem. Lett.* **3** (2012) 1099–1105.

[152] O. Krohn, K. Catani, J. Greenberg, S. Sundar, G. da Silva, and H. Lewandowski, *Isotope-specific reactions of acetonitrile ($Ch_3CN$) with trapped, translationally cold $CCl^+$*, *J. Chem. Phys.* **154** (2021) 074305.

[153] O. Krohn, K. Catani, and H. Lewandowski, *Formation of astrochemically relevant molecular ions: Reaction of translationally cold $CCl^+$ with benzene in a linear ion trap*, *Phys. Rev. A* **105** (2022) L020801.

[154] F. McLafferty, P. Bente, S.-C. T. R. Kornfeld, and I. Howe, *Metastable ion characteristics. XXII. collisional activation spectra of organic ions*, *J. Am. Chem. Soc.* **95** (1973) 2120–2129.

[155] L. Ratschbacher, C. Zipkes, C. Sias, and M. Köhl, *Controlling chemical reactions of a single particle*, *Nature Phys.* **8** (2012) 649–652.

[156] A. Hansen, M. Sørensen, P. Staanum, and M. Drewsen, *Single-ion recycling reactions*, *Angew. Chem. Int. Ed.* **51** (2012) 7960–7962.

[157] A. Perrott and D. Arnold, *The importance of conformation in the reactivity of radical cations. Changing configuration at saturated carbon centres*, *Can. J. Chem.* **70** (1992) 272–279.

[158] F. McLafferty, *Tandem mass spectrometry (MS/MS): A promising new analytical technique for specific component determination in complex mixtures*, *Acc. Chem. Res.* **13** (1980) 33–39.

[159] A. Johnson and E. Carlson, *Collision-induced dissociation mass spectrometry: A powerful tool for natural product structure elucidation*, *Anal. Chem.* **87** (2015) 10668–10678.

[160] L. Gagliardi and P. Pyykkö, *Theoreticl search for very short metal-actinide bonds: NUIr and isoelectronic systems*, *Angew. Chem. Int. Ed.* **43** (2004) 1573–1576.

[161] M. Straka and P. Pyykkö, *Linear HThThH: A candidate for a Th− Th triple bond*, *J. Am. Chem. Soc.* **127** (2005) 13090–13091.

[162] J. Lyon, H.-S. Hu, L. Andrews, and J. Li, *Formation of unprecedented actinide≡carbon triple bonds in uranium methylidyne molecules*, *PNAS* **104** (2007) 18919–18924.

[163] U. Jacovella, M. Scholz, and E. Bieske, *Electronic spectrum of the tropylium cation in the gas phase*, *J. Phys. Chem. Lett.* (2020) 8867–8872.